STUDY OF THE HELICITY DISTRIBUTIONS OF $Z\gamma$ PRODUCTION AT THE CMS EXPERIMENT

by

IRAKLI CHAKABERIA

B.S., Tbilisi State University, Georgia, 2002
M.S., Tbilisi State University, Georgia, 2004

AN ABSTRACT OF A DISSERTATION

submitted in partial fulfillment of the
requirements for the degree

DOCTOR OF PHILOSOPHY

Department of Physics
College of Arts and Sciences

KANSAS STATE UNIVERSITY
Manhattan, Kansas

2014

Abstract

This thesis represents the first study of the helicity distributions of $Z\gamma$ di-boson production at hadron colliders. I use 5 fb^{-1} of $\sqrt{s} = 7$ TeV center of mass energy proton-proton collision data, collected by the Compact Muon Solenoid (CMS) experiment at the Large Hadron Collider (LHC), to look at the angular distribution of the $Z\gamma \rightarrow e^+e^-\gamma/\mu^+\mu^-\gamma$ process and measure the helicity amplitudes that govern it. This study provides sensitivity to the interference terms between different quantum states and through the interference terms to the possible new physics. The final state is comprised of leptons (muon-antimuon or electron-positron pairs) with transverse momentum over 20 GeV and a photon with transverse energy over 30 GeV. Helicty amplitudes are measured for the total angular momentum of the quark-antiquark system up to $J_{q\bar{q}} = 2$. Four-dimensional multivariate analysis of the 2011 CMS data shows no significant deviations from the standard model prediction for the measured amplitudes.

STUDY OF THE HELICITY DISTRIBUTIONS OF $Z\gamma$ PRODUCTION AT THE CMS EXPERIMENT

by

IRAKLI CHAKABERIA

B.S., Tbilisi State University, Georgia, 2002
M.S., Tbilisi State University, Georgia, 2004

A DISSERTATION

submitted in partial fulfillment of the
requirements for the degree

DOCTOR OF PHILOSOPHY

Department of Physics
College of Arts and Sciences

KANSAS STATE UNIVERSITY
Manhattan, Kansas
2014

Approved by:

Major Professor
Tim Bolton

Abstract

This thesis represents the first study of the helicity distributions of $Z\gamma$ di-boson production at hadron colliders. I use 5 fb^{-1} of $\sqrt{s} = 7$ TeV center of mass energy proton-proton collision data, collected by the Compact Muon Solenoid (CMS) experiment at the Large Hadron Collider (LHC), to look at the angular distribution of the $Z\gamma \to e^+e^-\gamma/\mu^+\mu^-\gamma$ process and measure the helicity amplitudes that govern it. This study provides sensitivity to the interference terms between different quantum states and through the interference terms to the possible new physics. The final state is comprised of leptons (muon-antimuon or electron-positron pairs) with transverse momentum over 20 GeV and a photon with transverse energy over 30 GeV. Helicty amplitudes are measured for the total angular momentum of the quark-antiquark system up to $J_{q\bar{q}} = 2$. Four-dimensional multivariate analysis of the 2011 CMS data shows no significant deviations from the standard model prediction for the measured amplitudes.

Table of Contents

List of Figures

List of Tables

Acknowledgments

Pursuit of the PhD degree would not have been so smooth and rewarding without the support of many people, and I am deeply indebted to those who supported me during these years.

Foremost, I want to express my gratitude to my adviser, Professor Tim Bolton, whose guidance was vital in every aspect of my reserch. I am grateful for all the opportunities he gave me. Thanks to them, I was fully submerged in the experimental particle physics environment. I am especially grateful to him for giving me complete freedom in my work, which implied a great deal of confidence.

I am grateful to many professors here at KSU. I would like to thank Professor Yurii Maravin for inviting me to join the HEP group, the decision that is a cornerstone of this analysis and my career. I would like to thank Professor Larry Weaver for going through my calculations, and always listening to and commenting at my detailed reports regarding this analysis. I am thankful to Professors Glenn Horton-Smith and Bharat Ratra, who were always there to answer wide range of physics question I had.

I owe my deepest gratitude to the entire pixel detector team at Paul Scherrer Institute and, in particular to Dr. Danek Kotlinski, for letting me experience the CMS pixel detector firsthand, and for continuous support afterwards. My special thanks goes to Dr. Kaori Maeshima and the CMS WebBased Monitoring team at Fermilab and CERN, working with whom was a great experience.

I am forever grateful to my family back home, in Georgia, and especially to my mother for her patience during these years and caring support and encouragement. And of course I want to thank my wife Sofia and daughter Natalie, for their love no matter how fast or slow my work progressed, and how uncertain the future was.

Dedication

To my parents, who taught me the value of education.

Chapter 1

Introduction

The fundamental structure of the universe has always captured the human curiosity. The notion of atomism can be tracked back to Democritus, in the ancient Greece. Atoms were considered the indivisible constituents of the matter until early 20$^{\text{th}}$ century. Modern particle physics has emerged from the discovery of the electron by J. J. Thomson, and the sub-structure of the atom as a result of the famous Rutherford scattering experiments, which put positively charged nucleus in the center of the atom and electrons in its orbits. The metamorphosis of the particle physics into the high energy physics, through the invention of the particle accelerators, which accelerate protons or electrons to very high energies and smash them into nuclei or each other, revealed the whole zoo of the new particles. With accelerators reaching higher energies more and more particles were being discovered. By the early 1960s, physicists once again faced the problem of classification of over one hundred new particles, and the question whether they are the elementary constituents of matter. Continued efforts of theorists and experimentalists were rewarded by the very elegant solution. The fundamental particles were reduced to the quarks and leptons, and the carriers of their interactions. All other particles (e.g. protons or neutrons) are comprised of these elementary particles. The most robust and widely accepted description of these fundamental particles and there interactions is given by the theory called the standard model (SM). High energy physics experiments are designed to test this model and to seek for new phenomena that may lay beyond the standard model.

A short overview of the standard model is given in this chapter followed by the description of the $Z\gamma$ production process, which is the focus of this thesis.

1.1 The Standard Model

The standard model is a quantum field theory, combining quantum mechanics and special relativity into the $\mathrm{SU}(3)_c \times \mathrm{SU}(2)_L \times \mathrm{U}(1)_Y$ local gauge symmetry group to describe the matter and its interactions, which is the union of the quantum chromodynamics [2] (QCD) and the electroweak theory [3] (EWK). It describes electromagnetic, weak, and strong interactions, falling short of including the gravity and, thus, unifying all the known forces. Within this framework all visible matter observed in the universe is composed of 12 spin-half elementary particles – fermions. The interactions are mediated by the gauge bosons of the appropriate symmetry groups. All elementary particles have their corresponding antiparticles, which possess similar properties but have charge (both electric and color charge) opposite to those of their companions.

Fermions are classified into three generations of quarks and leptons. The classification is based on the mass scales of the particles, which are the only distinguishing property between the generations. Charged leptons (e, μ, τ) have their companion neutral leptons called neutrinos $(\nu_e, \nu_\mu, \nu_\tau)$, which only underlie the weak interaction. Quarks participate in all three interactions. They make up quark-antiquark bound states called mesons, or of three quarks called baryons. The observation of the four-quark state has been recently claimed by the BELLE experiment [4], in Japan and has recently been confirmed by the LHCb experiment [5], at CERN. The indications of the theoretically possible five-quark bound state, pentaquark, have been seen in some experiments, although have not been confirmed by other experiments with similar conditions.

Different gauge boson exchange between fermions corresponds to a different interaction. Electromagnetic interaction is represented by the photon exchange between charged particles; $\mathrm{W}^{\pm}$ and Z bosons are the mediators of the weak force, and gluons are the carriers of the strong interaction between quarks.

Finally, one of the most important bosons, introduction of which lets other particles acquire masses, is the Higgs boson. The CMS and the ATLAS experiments have recently discovered the new boson, which very well fits the standard model and further strengthens the theory. The summary of the standard model particles together with their properties is given in Fig. 1.1

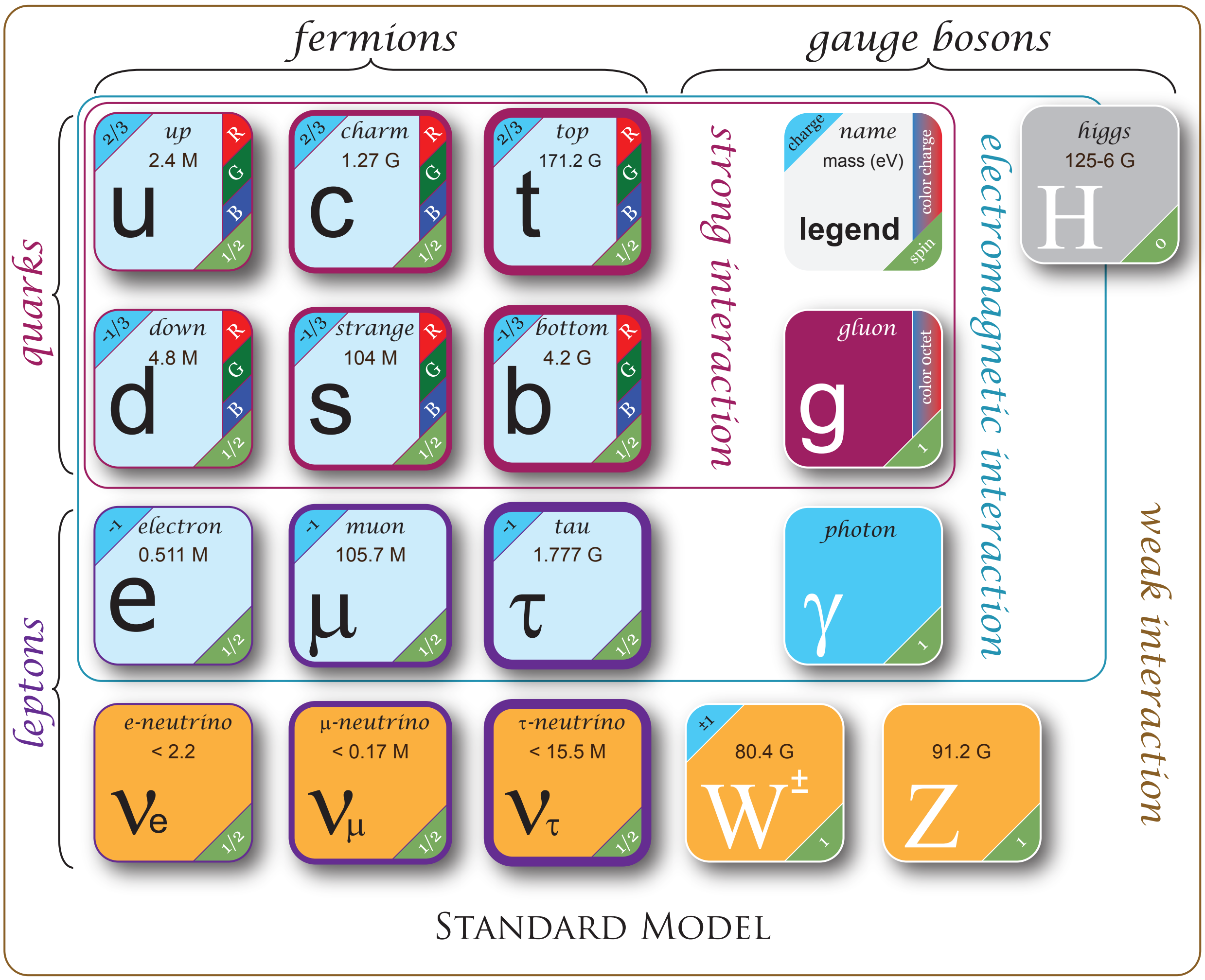

Figure 1.1: Table of the elementary particles within the standard model with their properties, showing the domains of the interactions as well as electroweak domain broken through the Higgs mechanism.

Despite all the elegance of the standard model and the recent discovery of the long anticipated final missing peace of the puzzle, the Higgs boson, the theory is still short of being accepted as the final theory of the matter and its interactions. Besides the already mentioned problem of not including gravity, which operates with many orders of magnitude smaller strength, there are many open questions that cannot be answered within the SM framework. Some of the big problems include: the matter-antimatter asymmetry in the universe, which cannot be accounted for by the CP asymmetry in the quark sector; the recently established fact that neutrinos have non-zero masses still lacks the robust and experimentally tested mechanism through which the masses could be acquired; cosmological observations of the last decades suggest existence of the "dark matter", the origin of which remains a mystery; finally, there are many free parameters in the SM, which need to be established empirically. All this suggests that there might be an underlying fundamental theory, which may extend beyond the SM. Therefore, the search for the new phenomena is highly motivated. The LHC provides a window into the physics at the order of magnitude higher energies than accessed by the previous experiments. This is a fundamentally new energy regime, and the discovery of the Higgs boson is the first fruit successfully harvested. One of the motivations of the analysis of this thesis is the sensitivity to new physics that may manifest itself as the deviations from the known distributions of the $Z\gamma$ process, when tested in the energy and luminosity regimes of the LHC.

1.1.1 Quantum Chromodynamics

Quantum chromodynamics is the part of the standard model that describes the strong interaction between quarks and gluons. It emerged from the quark model proposed by Gell-Mann [6] in 1964. The additional quantum number – *color* – was proposed for the quarks, which solved the problem that quarks being fermions seemed to violate the Pauli exclusion principal according to the experimental data from hadron spectroscopy. The final theory of the QCD was proposed by Weinberg [7], Fritzsch, Gell-Mann, and Leutwyler [8] in 1973 as a gauge theory of a $SU(3)_c$ symmetry group, where c stands for color. The concept of asymptotic freedom (described later) was added to the theory by Gross and Wilczek [9], which beautifully filled the demands of the experimental observations.

$$\begin{pmatrix} u \\ d \end{pmatrix} \quad \begin{pmatrix} c \\ s \end{pmatrix} \quad \begin{pmatrix} t \\ b \end{pmatrix}.$$

The $SU(3)$ symmetry group yields three color charges for each quark, which are denoted by *red(r)*, *green(g)* and *blue(b)* and existence of color octet of eight gluons which carry the linear combination of color-anticolor pairs and can be expressed as:

$$\begin{aligned}
\frac{1}{\sqrt{2}}(r\bar{b}+b\bar{r}), &\quad -\frac{i}{\sqrt{2}}(r\bar{b}-b\bar{r}),\\
\frac{1}{\sqrt{2}}(r\bar{g}+g\bar{r}), &\quad -\frac{i}{\sqrt{2}}(r\bar{g}-g\bar{r}),\\
\frac{1}{\sqrt{2}}(b\bar{g}+g\bar{b}), &\quad -\frac{i}{\sqrt{2}}(b\bar{g}-g\bar{b}),\\
\frac{1}{\sqrt{2}}(r\bar{r}-b\bar{b}), &\quad \frac{1}{\sqrt{6}}(r\bar{r}+b\bar{b}-2g\bar{g}).
\end{aligned}$$

The fact that QCD is a $SU(3)$ group and not a $U(3)$ is supported by the fact that singlet gluon is not experimentally observed. This non-Abelian nature of the theory enables gluons to directly interact with each other through the color charge.

The strong coupling constant, which defines the strength of the interaction, at the leading-order, can be expressed as:

$$\alpha_s(Q^2) = \frac{12\pi}{(11c-2n_f)\log\left(Q^2/\Lambda^2_{QCD}\right)}, \tag{1.1}$$

where Q is the momentum transfer, $n_f = 6$ is the number of the quark flavors, $c = 3$ is the number of quark colors, and Λ_{QCD} is the characteristic scale of the QCD. Two very important properties of the QCD follow from the Eq. 1.1, particularly, from the fact that the strength of the interaction depends on the momentum transfer, thus, on the distance between the interacting quarks.

First phenomena is called the *confinement*. It is the result of the coupling parameter α_s asymptotically growing when Q^2 becomes very low, or the distance between quarks becomes large – on the order of 10^{-15} m. This is the reason for quarks being confined into the colorless bound states like mesons (e.g. π meson $= u\bar{d}$) or baryons (e.g. proton $= uud$) and cannot be observed as free particles. The quarks that are confined into hadrons are called *valence quarks*, which are in constant exchange of gluons that are binding them. These gluons can produce quark-antiquark pairs, called *sea quarks*, which in combination with the confinement leads to the phenomena known as *hadronization*. Hadronization is the cascade pair-production of hadrons. It occurs due to the drastic increase of the gluon field energy when two quarks become largely separated. At a certain distance, creation of the quark-antiquark pair becomes energetically favored, which can lead to hadronization. The size of nuclei is related to the characteristic distance, to which strong interaction range is effectively limited. On these and larger scales the QCD is replaced by the bound state, or hadron, dynamics.

On the other hand, the small distance, thus, high momentum transfer interactions, between quarks, results in a small α_s and leads to the effect called asymptotic freedom. This effect justifies the use of the perturbative QCD. The characteristic scale of the QCD is given by the Λ_{QCD} scale factor, at which the perturbative approach fails.

1.1.2 Electroweak Theory

Radioactive beta decay is one of the first nuclear processes studied in the particle physics. This process is mediated by the weak force and was initially described by the Fermi's theory of beta decay. In this model four fermions directly couple with a Fermi coupling constant G_F, coming to a single four-fermion vertex. The theory is still a good approximation for lepton scattering in low momentum transfer regime, but it fails at high energies because G_F coupling constant grows as the square of the energy. Beta decay is weak interaction with charged currents and Fermi's model had two conserved vector currents. But formulating weak interaction as a $SU(2)$ gauge theory, as Yang and Mils showed [10], also allows to have a third conserved current, which is parity violating axial current. The experiments by

Chien-Shiung Wu [11] confirmed the parity violation in weak interactions. Although, this current cannot be assumed to be the neutral current of the $SU(2)$ group, because it would involve coupling with both left and right handed fermions, similarly to the electromagnetic current. Left and right-handed particles can be distinguished by the new quantum number – *isospin*, I. Isospin was first introduced by Heisenberg to describe proton and neutron as two different isospin states of the same particle. Left-handed particles are arranged into isospit doublets $I{=}\frac{1}{2}$, with charged leptons and down type quarks (d, s, b) having isospin projection $I_3{=}-\frac{1}{2}$ and neutrinos and up-type quarks (u, c, t) projection $I_3{=}\frac{1}{2}$. Right-handed particles are isospin singlets $I_3{=}0$;

In other words, $SU(2)_L$ symmetry group, where L stands for the isospin, indicating that gauge fields couple only with the left-handed fermions, introduces three massless gauge bosons W^1, W^2 and W^3 and a coupling constant g_W to couple to fermions. To account for the parity violation and neutral currents, addition of the $U(1)_Y$ symmetry is necessary. This model was proposed by the Glashow [12], Weinberg [13], and Salam [14] and it unifies electromagnetism with weak interaction.

The new symmetry required for the electroweak theory is *hypercharge* symmetry. Hypercharge is related to the electric charge and the weak isospin via Gell-Mann-Nishijima relation:

$$Y = 2(Q - I_3). \tag{1.2}$$

The $U(1)_Y$ symmetry group gives rise to additional gauge field B_μ and a coupling constant g. Together with the W^1_μ, W^2_μ, and W^3_μ, it takes care of third conserved (neutral) current and parity violation in weak interactions. The weak interaction vector bosons, $W^\pm$ and Z, were first observed in UA1 [15] and UA2 [16] experiments at CERN. Since $W^\pm$ only couple to left-handed fermions, they can be constructed as the linear combination of the W^1_μ and W^2_μ gauge fields of the $SU(2)_L$:

$$
\begin{aligned}
W_\mu^+ &= \frac{1}{\sqrt{2}}(W_\mu^1 - iW_\mu^2), \\
W_\mu^- &= \frac{1}{\sqrt{2}}(W_\mu^1 + iW_\mu^2).
\end{aligned}
\tag{1.3}
$$

Both the W_μ^3 and the B_μ fields couple to the neutrinos, thus to derive electromagnetic and neutral weak interactions, their linear combination has to be taken:

$$
\begin{aligned}
Z_\mu &= \frac{1}{\sqrt{g_W^2 + g^2}}(g_W W_\mu^3 - gB_\mu), \\
A_\mu &= \frac{1}{\sqrt{g_W^2 + g^2}}(gW_\mu^3 + g_W B_\mu).
\end{aligned}
\tag{1.4}
$$

where A_μ represents the electromagnetic field. By changing the variables, these relations can be expressed as:

$$
\begin{aligned}
Z_\mu &= (W_\mu^3 \cos\theta_W - B_\mu \sin\theta_W), \\
A_\mu &= (W_\mu^3 \sin\theta_W + B_\mu \cos\theta_W).
\end{aligned}
\tag{1.5}
$$

where θ_W is the weak mixing angle, also called Weinberg angle, which connects the $SU(2)_L$ and the $U(1)_Y$ coupling constants and the electric charge as well. It is the free parameter of the standard model to be determined empirically:

$$
e = g_W \sin\theta_W = g\cos\theta_W. \tag{1.6}
$$

Both, leptons and quarks couple to the weak gauge bosons, and through weak interaction the flavor of the particles may change. The weak eigenstates for quarks are different from their mass eigenstates, therefore, they may change both flavor and type (up-type to down-type) through weak interaction. This quark mixing is described by the Cabibbo-Kobayashi-Maskawa matrix, that gives the amplitudes of such flavor-change between quarks:

$$
\begin{pmatrix} d' \\ s' \\ b' \end{pmatrix} = \begin{pmatrix} V_{ud} & V_{us} & V_{bb} \\ V_{cd} & V_{cs} & V_{cb} \\ V_{td} & V_{ts} & V_{tb} \end{pmatrix} \begin{pmatrix} d \\ s \\ b \end{pmatrix}.
$$

Where the d', s' and b' are the weak eigenstates of the quarks (same relation is true for the down type quarks as well). Flavor change between same generation quarks are preferred to others (the branching ratio of top quark decay to bottom quark is nearly 100%, $V_{tb} \approx 1$). The week process of the quark flavor change, in addition to being parity violating, also violates the charge conjugation. The slight disbalanse in the combined charge-parity (CP) symmetry is also experimentally observed. CP violation is a very important phenomena that contributes to the matter-antimatter asymmetry, however the observed asymmetry in the universe cannot be accounted for only by the CP asymmetry observed in the quark sector so far.

Neutrinos only interact through the weak interaction, therefore, their flavor states are the weak eigenstates. However, the neutrino mixing was experimentally observed, which means that, like quarks, the flavor states of the neutrinos differ from their eigenstates. The matrix similar to the CKM for the neutrinos is known as Pontecorvo-Maki-Nakagawa-Sakata (PMNS) matrix. Neutrino oscillation was a very important observation, because it is an evidence for the non-zero mass of neutrinos, which is not part of the original standard model, but can be included by a simple extension.

Another mechanism, which is necessary for the standard model particles to acquire masses is the Higgs mechanism. Experimental measurements of the weak interactions showed that unlike a photon and a gluon, $W^{\pm}$ and Z gauge bosons are massive, which is the reason for weak force being very short scaled. This problem could be overcome by the introduction of the new scalar field with the non-zero vacuum expectation value. As a result, the electroweak symmetry breaks down to $U(1)_{em}$ electromagnetic interaction, which provides coupling to the charged particles only. Through this mechanism, massless particles dynamically acquire mass by coupling to the Higgs field. The Higgs boson is the spin zero particle corresponding to the Higgs field. Recent discovery of the Higgs-like boson by the CMS and ATLAS experiments was yet another triumph of the standard model [17].

Electroweak theory, as well as the QCD, is non-Abelian gauge theory and, therefore, it allows the gauge bosons to self-couple. This self-coupling is one of the main focuses of this thesis. In particular, standard model allows triple or quartic vertecies with participation of the charged vector bosons 1.2a, but doesn't allow the neutral vertex 1.2b:

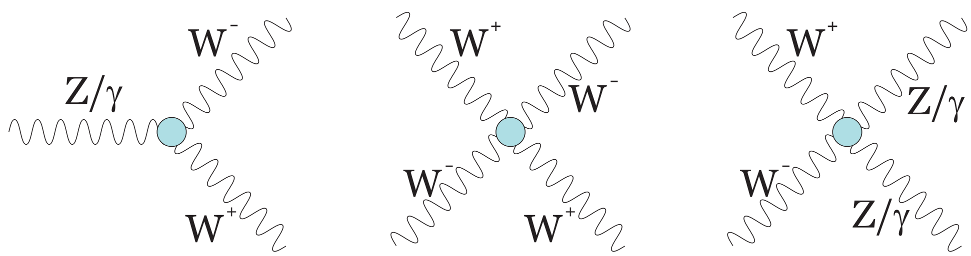

(a) Vertices allowed in the standard model

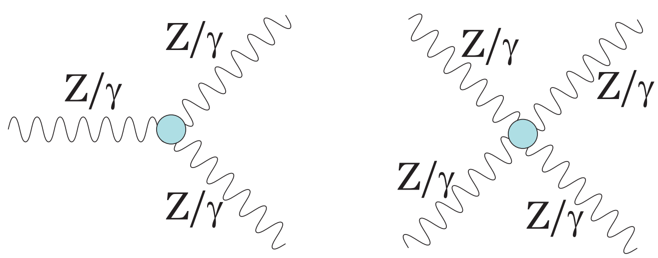

(b) Anomalous vertices not allowed in the standard model

Figure 1.2: Triple and quartic electroweak gauge boson self-coupling vertices.

1.2 $Z\gamma$ production at the LHC

The standard model makes very precise prediction of the coupling parameters between the electroweak gauge bosons, therefore, study of the diboson production at the energy scales of the LHC provides a unique test of the electroweak theory. Recent observations of the pair production of the electroweak gauge bosons at the Tevatron were yet another victory of the standard model.

As already mentioned, the coupling between neutral electroweak gauge bosons is zero in the standard model, thus, the triple ZZZ, $ZZ\gamma$ or $Z\gamma\gamma$ vertices are not allowed at leading order within the SM framework. However, if presence of the new physics can allow such coupling, it can be tested by measuring the $Z\gamma$ or ZZ production. Such couplings are present in numerous non standard model theories, such as supersymmetry, technicolor, little Higgs model, etc. These, so called anomalous triple gauge couplings (aTGCs) would result in higher cross-section or different kinematic distribution of the final state particles. Due to the much greater cross-section of the $Z\gamma$ production than ZZ, this analysis will concentrate on the first one. Much greater number of the event candidates allows us to do a more elaborate and multidimensional analysis of the kinematic distribution of the process.

The sensitive variable to the aTGCs of the $Z\gamma$ production, is the transverse momentum of the photon. Non-zero couplings at the $ZZ\gamma$ or $Z\gamma\gamma$ vertices result in the increased number of the high energy photons. This variable is used to set limits on the aTGCs. However, by considering the kinematics of the process, and breaking down the data into multiple angular dimensions and larger parameter space (helicity amplitudes), we may gain sensitivity throughout the entire photon energy spectrum.

The $Z\gamma$ pair production at the LHC is largely dominated by the leading order, quark-antiquark annihilation processes shown in Fig. 1.3:

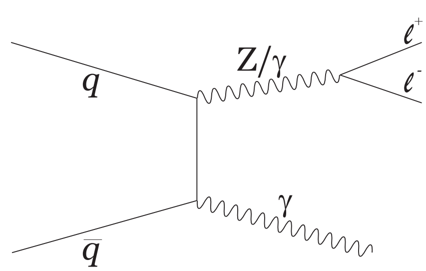

(a) $Z\gamma$ production by photon radiation from one of the quarks (t-channel) – initial state radiation (ISR)

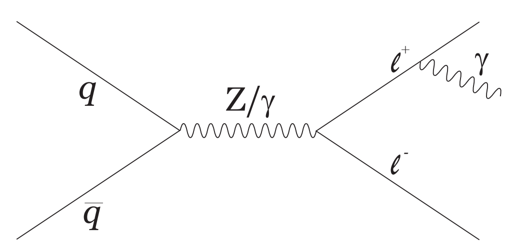

(b) $Z\gamma$ production by photon radiation from one of the leptons (s-channel) – final state radiation (FSR)

Figure 1.3: Dominant channels of the $Z\gamma$ production at the LHC.

These Feynman diagrams show the production processes, where Z decays leptonically, which is the decay channel studies in this thesis. The branching ratio of the leptonic decay of the Z boson is about 30%, and about two thirds of it is taken by the so called invisible decay channel, when the leptons are a neutrino-antineutrino pair. The rest is taken by the hadronic decay channels. However, study of the leptonic channel, where leptons are muons or electrons, is advantageous because this channel could be fully reconstructed, virtually without any background. The $Z \to \ell\ell$ ($\ell = e, \mu$) process is the standard candle for many studies in the high energy physics.

Besides the production processes shown on Fig. 1.3, at the high energies and high quark-gluon luminosities, such as at the LHC, $qg \to Z\gamma$ production process (Fig. 1.4) contribution becomes significant, especially to the high photon transverse energy (high $Z\gamma$ invariant mass) section. The model described in Chapter 2 considers only the leading order production, but the next-to-leading order (NLO) contribution is considered two-fold in the analysis. First, the effect on the kinematic distribution is studied separately and considered as a systematic uncertainty. Second, the higher cross-section of the NLO, from the QCD corrections are considered as a normalization factor. The value of the NLO cross-section is obtained using MCFM Monte Carlo tool [18], which very well describes the Monte Carlo simulation of $Z\gamma$ plus up to 2 jets production shown in Chapter 5. The production through gluon fusion is extremely small in the standard model and is completely neglected.

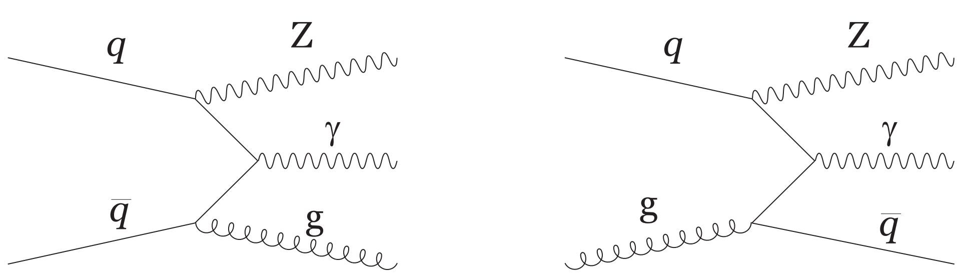

Figure 1.4: Feynman diagrams for the NLO quark-gluon fusion production contribution to the $Z\gamma$ production at the LHC.

The most general vertex function for the triple vertex shown on Fig. 1.5 can be expressed as [19]:

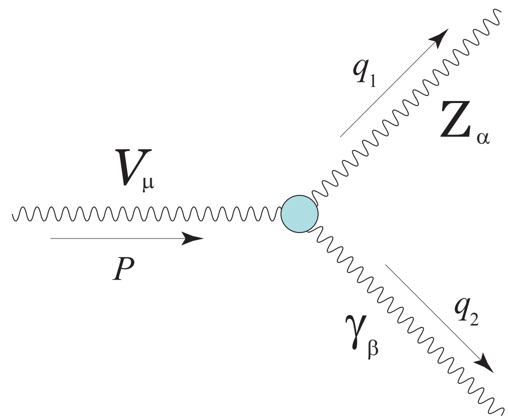

Figure 1.5: Anomalous triple vertex for $VZ\gamma$ (V=Z or γ), showing the incoming and outgoing momenta of the gauge bosons.

$$\begin{aligned}\Gamma^{\alpha\beta\mu}_{ZZ\gamma}(q_1, q_2, P) = \frac{P^2 - q_1^2}{m_Z^2} \Bigg[& h_1^Z \left(q_2^\mu g^{\alpha\beta} - q_2^\alpha g^{\mu\beta} \right) \\ & + \frac{h_2^Z}{m_Z^2} P^\alpha \left((P \cdot q_2) g^{\mu\beta} - q_2^\mu P^\beta \right) \\ & + h_3^Z \epsilon^{\mu\alpha\beta\rho} q_{2\rho} \\ & + \frac{h_4^Z}{m_Z^2} P^\alpha \epsilon^{\alpha\beta\rho\sigma} P_\rho q_{2\sigma} \Bigg],\end{aligned} \tag{1.7}$$

where m_Z is the mass of the Z boson, q_1, q_2 and P are the momenta of the gauge bosons indicated on the figure and h_i^V ($i = 1, 2, 3, 4$) are the anomalous coupling parameters. V here stands for either Z or the γ, because the same function can be rewritten for the $Z\gamma\gamma$ vertex. These coupling parameters violate the charge conjugation, but only h_3^V and h_4^V also violate P-symmetry. Thus, h_3^V and H_4^V are CP conserving. In the standard model all these coupling parameters are zero at tree level and only the CP conserving ones are non-zero when loop diagrams are included.

Chapter 2

Theoretical Model

This chapter describes the method used for the calculations of the angular distribution function and the theoretical model I apply to the $Z\gamma$ process for the measurement of the helicity amplitudes. Treatment of the detector, and selection requirement acceptances and efficiencies in the likelihood function is presented at the end of the chapter.

Presented analysis aims at studying the helicity distributions of the $Z\gamma$ system by looking at the angular distribution of the production and decay processes. As a result, analysis yields the measurement of the helicity amplitudes that govern the process under study. In addition, this approach gives access to the interference terms between different helicity states and therefore is more sensitive to any small deviations of the amplitudes of these states from their standard model predictions. In other words, if there is a small non-zero perturbation to the standard model due to a new physics its effect will be manifested stronger in the interference term with the standard model than on the deviation from the integrated cross-section of the process. So, in this analysis I attempt to gain sensitivity to a new physics by breaking down the $Z\gamma$ production process into its constituent helicity states and access the interference between each state by looking at the four dimensional angular distribution picture.

2.1 Helicity Formalism

The processes that take place at high energy particle colliders are highly relativistic, thus treatment of the $Z\gamma$ production at the LHC using non-relativistic spin-orbit formalism poses technical complications that rise due to the spin and orbital momentum operators being defined in the reference frames that are not at rest with respect to each other. The spin operator is defined in the rest frame of the particle, whereas the orbital momentum operator is defined in the center of mass (CM) frame. The helicity operator $h = \vec{s} \times \hat{p}$, on the other hand, is invariant both, under Lorentz rotations and boosts, thus application of the helicity formalism [20] is very convenient for the treatment of such relativistic processes.

Due to the rotational invariance of the helicity operators, one can define the basis by the two-particle state vectors $\mid j, m, \lambda_1, \lambda_2\rangle$ with total angular momentum j, angular momentum projections m and helicities of the particles λ_1 and λ_2.

The process described in this analysis consists of the quark-antiquark scattering and consequent decay of the Z boson into two leptons.

$$q + \bar{q} \rightarrow Z + \gamma; Z \rightarrow \ell^+ + \ell^-. \tag{2.1}$$

In the Z decay case we can describe the final state by the direction of the decay axis $\hat{n}(\theta, \varphi)$ with respect to the spin-quantisation axis of the Z boson (z axis), by the helicities of the leptons λ_ℓ and $\lambda_{\bar{\ell}}$ and by the momentum of one of the leptons p. Since the process is described in the CM frame of the Z boson $p_\ell + p_{\bar{\ell}} = 0$. The amplitude for the leptons emerging with the angles (θ, φ) from the Z decay process, with initial state $\mid J, m\rangle$, where J is the spin decaying particle and m are the projections, is:

$$A = \langle\theta, \varphi, \lambda_\ell, \lambda_{\bar{\ell}} \mid U \mid J, m\rangle, \tag{2.2}$$

where U is the propagator for the decay process. Thus, helicity treatment naturally yields the angular distribution function by simply taking the probability of the processes $\mid A \mid^2$.

Using the rotation operators in the helicity representation $\mid j, m, \lambda_1, \lambda_2\rangle$, for the decay process, results in the following:

$$
\begin{aligned}
&A = C \times D^J_{m\lambda_{\ell\ell}}(\alpha, \beta, \gamma) A_{\lambda_\ell \lambda_{\bar{\ell}}}, \\
&\lambda_{\ell\ell} = \lambda_\ell - \lambda_{\bar{\ell}},
\end{aligned}
\tag{2.3}
$$

where C is the normalization constants, $A_{\lambda_\ell \lambda_{\bar{\ell}}}$ are the helicity amplitudes, and $D^J_{m\lambda_{\ell\ell}}(\alpha, \beta, \gamma)$ are the Wigner D-functions, with α, β and γ the Euler angles of the decay axis. Without loss of generality, for simplification, one can take $\gamma = -\alpha$ and α and β can be described as the azimuthal and polar angle of one of the leptons in the rest frame of the Z boson, respectively, as shown on Fig. 2.1b. Equation 2.3 can then be rewritten in terms of the small d-functions as:

$$
A = C \times d^J_{m\lambda_{\ell\ell}}(\cos\theta_\ell) A_{\lambda_\ell \lambda_{\bar{\ell}}} e^{-i(\lambda_Z - \lambda_{\ell\ell})}. \tag{2.4}
$$

In this analysis the angles are described in the so called helicity frame of the particles involved in the process. For the quark-antiquark scattering process that would mean that the reference frame is the CM frame of the incoming quarks with its z axsis along their momentum in the lab frame. The direction of the x and y axes is arbitrary in the scattering process. This means that there is no preferred azimuthal direction for the resultant Z boson or a photon. However, the φ_ℓ azimuthal angle of the lepton is not arbitrary anymore, because it is bound by the Euler angle condition I required earlier ($\gamma = -\alpha$). This can be translated into the angle between scattering and decay planes, which is descriptive of the process, and a result of these two processes being coupled. The amplitude for the scattering process is

$$
\begin{aligned}
&T = C' \sum_J [2J+1] d^J_{\lambda_{qq}\lambda_{Z\gamma}}(\cos\theta_Z) e^{i(\lambda_{qq} - \lambda_{Z\gamma})} T^J_{\lambda_q \lambda_{\bar{q}} \lambda_Z \lambda_\gamma}, \\
&\lambda_{qq} = \lambda_q - \lambda_{\bar{q}}; \lambda_{Z\gamma} = \lambda_\gamma - \lambda_Z,
\end{aligned}
\tag{2.5}
$$

where C' is the normalization constant, J is the total angular momentum of the initial state, λ parameters are the helicities of the particles, and $T^J_{\lambda_q\lambda_{\bar{q}}\lambda_Z\lambda_\gamma}$ are the helicity amplitudes involved.

The $A_{\lambda_\ell\lambda_{\bar{\ell}}}$ and $T^J_{\lambda_q\lambda_{\bar{q}}\lambda_Z\lambda_\gamma}$ quantum mechanical amplitudes are complex functions of the rapidity, and mass of the particles involved in the process.

2.2 Angular Distribution Function

In this analysis, helicity formalism is used for calculation of the angular distribution function of the $q\bar{q} \to Z(\ell\bar{\ell})\gamma$ process and measurement of the helicity amplitudes that govern it. It is obtained by calculating the probability of the final state particles emerging with the particular angles. Thus, by taking the absolute square of the convolution of the quark-antiquark scattering (Eq. 2.5) and Z decay (Eq. 2.4) amplitudes. Helicities of the particles are not measured in the experiment, so they have to be summed over. The helicities of quarks and the Z boson have to be summed over on the amplitude level, since they are not directly observable. The helicities of the leptons and the photon have to be summed over incoherently because we do not measure the particular helicity state, but they are directly observable. So, neglecting the normalization constants, and noting that Z boson is a spin one particle:

$$\begin{aligned}\frac{d\sigma}{d\Omega_Z d\Omega_\ell} \sim \sum_{\lambda_\ell\lambda_{\bar{\ell}}\lambda_\gamma} \Bigg| \sum_{J\lambda_q\lambda_{\bar{q}}\lambda_Z} & [2J+1] d^J_{\lambda_{q\bar{q}}\lambda_{Z\gamma}}(\cos\theta_Z) T^J_{\lambda_q\lambda_{\bar{q}}\lambda_Z\lambda_\gamma} e^{i(\lambda_{qq}-\lambda_{Z\gamma})\varphi_Z} \\ & \times d^1_{\lambda_Z\lambda_{\ell\ell}}(\cos\theta_\ell) A_{\lambda_\ell\lambda_{\bar{\ell}}} e^{-i(\lambda_Z-\lambda_{\ell\ell})\varphi_\ell} \Bigg|^2 .\end{aligned} \tag{2.6}$$

where $\Omega_Z(\theta_Z, \varphi_Z)$ and $\Omega_\ell(\theta_\ell, \varphi_\ell)$ are the polar and azimuthal angles for the Z boson and the photon respectively. In Eq. 2.6, the exponents, with helicities in the outer sum, square up to one, and vanish. Note that the quark and the lepton helicities get into summation as the difference of the helicities between particle and its anti-particle, except in the helicity amplitudes. This will cause degeneracy of the helicity amplitudes for the $\lambda_{q\bar{q}} = 0$ and $\lambda_{\ell\bar{\ell}} = 0$

case. For simplicity I will use the following notation:

$$T^J_{\lambda_{qq}\lambda_Z\lambda_\gamma} \equiv \sum_{\lambda_q\lambda_{\bar{q}}}^{\lambda_{q\bar{q}}=\lambda_q-\lambda_{\bar{q}}} T^J_{\lambda_q\lambda_{\bar{q}}\lambda_Z\lambda_\gamma}, \tag{2.7}$$

$$A_{\lambda_{\ell\ell}} \equiv \sum_{\lambda_\ell\lambda_{\bar{\ell}}}^{\lambda_{\ell\ell}=\lambda_\ell-\lambda_{\bar{\ell}}} A_{\lambda_\ell\lambda_{\bar{\ell}}}. \tag{2.8}$$

The above mentioned results in the following final expression for the angular distribution:

$$\begin{aligned}\frac{d\sigma}{d\Omega_Z d\Omega_\ell} \sim \sum_{\lambda_{\ell\ell}\lambda_\gamma} \Bigg| \sum_{J\lambda_{qq}\lambda_Z} & [2J+1] d^J_{\lambda_{q\bar{q}}\lambda_{Z\gamma}}(\cos\theta_Z) T^J_{\lambda_{qq}\lambda_Z\lambda_\gamma} \\ & \times d^1_{\lambda_Z\lambda_{\ell\ell}}(\cos\theta_\ell) A_{\lambda_{\ell\ell}} e^{i[(\lambda_{qq}+\lambda_Z)\varphi_Z-\lambda_Z\varphi_\ell]} \Bigg|^2.\end{aligned} \tag{2.9}$$

This shows that the azimuthal angles, as already mentioned above, get into the expression as difference, which is related to the angle between the production and decay planes.

Exact definition of the angles is given under the vector diagrams describing them, shown on the Fig. 4.7

All the possible helicities are allowed in the process, with exception of the final state leptons. These leptons are decay products of the Z boson, so the helicity suppression results in the opposite helicity leptons contributing to the process $\lambda_{\ell\ell} = \lambda_\ell - \lambda_{\bar{\ell}} = \pm 1$ and $\lambda_{\ell\ell} = 0$ is suppressed by the factor of $\left(\frac{m_e}{m_Z}\right)^4$. For other particles:

$$\lambda_Z = -1, 0, 1; \quad \lambda_\gamma = \pm 1; \quad \lambda_q = -1/2, 1/2.$$

2.3 Assumptions for the Theoretical Model

The number of the helicity amplitudes can be further constrained from the theoretical point of view and by the choice of the model. These constraints and assumptions for the model used in the analysis are presented in this section. Systematic uncertainties that arise from these assumptions are considered in the final result and are presented in the results section.

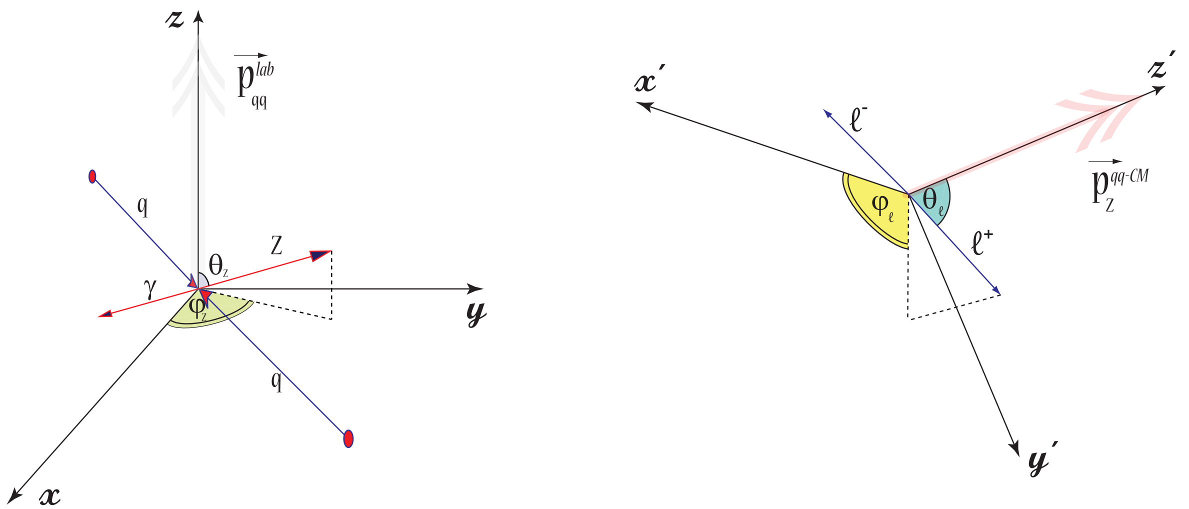

(a) Production angles are measured in the CM frame of the $q\bar{q}$. The z axis is oriented along the direction of the momentum of the $q\bar{q}$ in the lab frame. Orientation of the x and y axes are obtained by rotation of the lab frame by the Euler angles $(\varphi_{q\bar{q}}, \theta_{q\bar{q}}, -\varphi_{q\bar{q}})$, where those angles are the polar and azimuthat angles of the $q\bar{q}$ systems momentum in the lab frame. However, the orientation of the x and y axises is actually arbitrary, in contrast to the orientation of the x' and y' of the decay coordinate system

(b) Decay angles are measured in the rest frame of the Z boson. The z' axis is oriented along the direction of the Z boson in the $q\bar{q}$ CM frame. x' and y' axes are obtained by the rotation of the xyz system of coordinates by the Euler angles $(\varphi_Z, \theta_Z, -\varphi_Z)$ into the $x'y'z'$

Figure 2.1: Definition of the polar and azimuthal angles used in the analysis.

2.3.1 Leading Order Analysis

The angular distribution 2.9 has been calculated for the $q\bar{q} \to Z\gamma; Z \to \ell^+\ell^-$ process, therefor the analysis in this sense is leading order analysis. So I do not consider the initial state gluon radiation by the incoming quarks ($qq \to Z\gamma g$). The final state photon radiation from the leptons ($q\bar{q} \to Z; Z \to \ell^+\ell^-\gamma$) is also removed from the signal sample.

2.3.2 Effective Parity Conservation

The processes studied in this analysis involve weak interactions and are parity violating. However, the specifics of the experiment provide the additional symmetry, that can play out as if $q + \bar{q} \rightarrow Z + \gamma$ process was parity conserving.

The LHC is a proton-proton collider, thus, there is no preferred direction for the quarks and anti-quarks that produce the $Z\gamma$ state, in contrast, to for example, proton-antiproton colliders like Tevatron. Since this hard collision is between the quark that comes from the proton and the antiquark from the sea, there is a longitudinal momentum disbalance towards the direction of the quark. By looking at the high rapidity Z bosons ($|y| > 1$), the direction for the incoming quarks (antiquarks) could be identified. But, in this analysis, I do not focus on the particular rapidity range, therefore using the symmetry of the provided proton-proton collisions and an *effective* parity conservation for the quark-antiquark scattering process:

$$\begin{aligned}\langle \lambda_Z, \lambda_\gamma \mid T^J \mid \lambda_q, \lambda_{\bar{q}} \rangle &= \langle \lambda_Z, \lambda_\gamma \mid \Pi T^J \Pi \mid \lambda_q, \lambda_{\bar{q}} \rangle \\ &= \frac{\eta_Z \eta_\gamma}{\eta_q \eta_{\bar{q}}} (-1)^{s_Z + s_\gamma - s_q - s_{\bar{q}}} \langle -\lambda_Z, -\lambda_\gamma \mid T^J \mid -\lambda_q, -\lambda_{\bar{q}} \rangle,\end{aligned} \tag{2.10}$$

where Π is the parity operator, s and η parameters are the spins and parities of the particles, accordingly.

$$\eta_Z = -1; \quad \eta_\gamma = -1; \quad \eta_q = 1; \quad \eta_\ell = -1. \tag{2.11}$$

Equations 2.10 and 2.11 will result in the reduction of the independent helicity parameters, which in used notations is:

$$T^J_{\lambda_Z \lambda_\gamma \lambda_{qq}} = -T^J_{-\lambda_Z - \lambda_\gamma - \lambda_{qq}}. \tag{2.12}$$

2.3.3 t-Channel Effects

As already mentioned, the standard model $Z\gamma$ production by the quark-antiquark scattering is possible through *t or u-channels*. So, the production cross-section is proportional to $1/t$ and $1/u$ where t and u are the quark propagators for the *t-channel* and *u-channel* respectively and given by:

$$t = -\hat{s} + (\hat{s} - M_Z^2)\cos\theta_Z, \tag{2.13}$$

$$u = -\hat{s} - (\hat{s} - M_Z^2)\cos\theta_Z, \tag{2.14}$$

where, $\hat{s}$ is the center of mass energy of the system:

$$\hat{s} = (p_q + p_{\bar{q}})^2 = (p_Z + p_\gamma)^2; \quad p = (E, \vec{p}). \tag{2.15}$$

In cases when $\hat{s} \gg M_Z$, this results in singularities at the $\cos\theta_Z = \pm 1$. From the point of view of the helicity analysis (Eq. 2.9), this is seen as the states with the large total angular momentum J. In order to avoid the need for the high J values I explicitly factor out the singular behaviour associated with the quark propagators, thus modifying the angular distribution function:

$$\frac{d\sigma}{d\Omega_Z d\Omega_\ell} \to F(\cos\theta_Z)\frac{d\sigma}{d\Omega_Z d\Omega_\ell}, \tag{2.16}$$

where

$$F(\hat{s}, M_Z, \cos\theta_Z) = \frac{\hat{s}^2}{4}\left(\frac{1}{\hat{s} + (\hat{s} - M_Z^2)\cos\theta_Z} + \frac{1}{\hat{s} - (\hat{s} - M_Z^2)\cos\theta_Z}\right)^2, \tag{2.17}$$

and $\hat{s} = M_{Z\gamma}$ is the center of mass energy of the $Z\gamma$ system, equal to the three body invariant mass of two leptons and a photon that comprise the $Z\gamma$ event candidate and is denoted by $M_{Z\gamma}$.

2.4 Likelihood Function

Relatively small background and good angular resolution of the lepton and photon measurements at the CMS, enable the successful usage of the unbinned likelihood method for this analysis. The background and resolution effects are neglected and in order to account for different number of events, or different total integrated luminosities, in data and Monte

Carlo datasets, extended maximum likelihood is considered. The uncertainties that rise from these assumptions are discussed in Chapter 7.

If Eq. 2.16 is recast into a form:

$$W(\Omega) = \sum_{i}^{N_p} A_i \omega_i(\Omega), \tag{2.18}$$

$$\Omega = (\Omega_Z, \Omega_\ell), \tag{2.19}$$

where A_i are the parameters, which are an algebraic construct of the helicity amplitudes to be measured, N_p are the number of those parameters (not the actual number of helicity parameters), and $\omega_i(\Omega)$ are the algebraic construct of the known functions from 2.16. This reformatting is described in detail in Appendix A; and if the probability of the event being detected, which means accepted by the detector and by the selection requirements, is defined as $\epsilon(\Omega)$, then the probability distribution function (PDF) for the observed events is:

$$P(\Omega) = \frac{W(\Omega)\epsilon(\Omega)}{\int W(\Omega)\epsilon(\Omega) d\Omega}. \tag{2.20}$$

Using Eq. 2.20 as the PDF and considering the N_D number of the observed events, yields the following likelihood function:

$$L = \prod_{n=1}^{N_D} P(\Omega_n). \tag{2.21}$$

L is the function of the A_i parameters, which are measured using the maximum likelihood principle $\frac{\partial L}{\partial A_i} = 0$. To do so, the TMinuit minimization package of the ROOT [21] is used to find the parameters that minimize the $-\ln L$ function. Finding the absolute extrema of the function is a challenging task, and finding the maximum of a function is usually done by finding the minimum of the negative of that function. Taking the natural logarithm of the likelihood function before the minimization is very useful due to the feature of the logarithm, to convert a product of factors into a summation of factors. This conversion does not change the result, because taking the natural logarithm of the function is a monotone transformation. Negative logarithm of Eq. 2.21 can be further simplified as:

$$
\begin{aligned}
\mathscr{L} &= -\ln L = -\ln \prod_{n=1}^{N_D} \frac{W(\Omega_n)\epsilon(\Omega_n)}{\int W(\Omega)\epsilon(\Omega)d\Omega} \\
&= -\sum_{n=1}^{N_D} \ln\left(W(\Omega_n)\epsilon(\Omega_n)\right) + \sum_{n=1}^{N_D} \ln\left(\int W(\Omega)\epsilon(\Omega)d\Omega\right) \\
&= -\sum_{n=1}^{N_D} \ln\left(\epsilon(\Omega_n)\sum_{n'}^{N_p} A_{n'}\omega_{n'}(\Omega_n)\right) + N_D \ln\left(\sum_{n'}^{N_p} A_{n'} \int \omega_{n'}(\Omega)\epsilon(\Omega)d\Omega\right) \\
&= \underbrace{-\sum_{n=1}^{N_D} \ln \epsilon(\Omega_n)}_{1} \underbrace{-\sum_{n=1}^{N_D} \ln\left(\sum_{n'}^{N_p} A_{n'}\omega_{n'}(\Omega_n)\right)}_{2} + N_D \ln\left(\sum_{n'}^{N_p} A_{n'} \underbrace{\int \omega_{n'}(\Omega)\epsilon(\Omega)d\Omega}_{3}\right).
\end{aligned}
\tag{2.22}
$$

Part 1 in Eq. 2.22 doesn't depend on the A_i parameters thus is irrelevant for the minimization and can be dropped. After these changes part that includes the $\epsilon(\Omega)$ acceptance function is the part 3. It is included in a form that allows to be estimated at once using the Monte Carlo simulation technique without the need to know the exact analytical form of the $\epsilon(\Omega)$ function itself.

The likelihood function 2.21 is based on the normalized PDF 2.20, therefor the parameters are measured only in a relative sense and do not depend on the number of events. In the cases when amount of data, in my case integrated luminosity, is itself a relevant quantity, usage of extended maximum likelihood method is more suitable. For this analysis corresponding extended likelihood function has the following form:

$$
EL = L \times \frac{\left[\mathcal{L} \int W(\Omega)\epsilon(\Omega)d\Omega\right]^{N_D}}{N_D!} e^{-\mathcal{L}\int W(\Omega)\epsilon\Omega d\Omega}. \tag{2.23}
$$

Taking the negative logarithm of the EL yield the following expression:

$$
\begin{aligned}
\mathscr{E}\mathscr{L} &= -\ln(EL) = -\sum_{n=1}^{N_D} \ln\left(\sum_{n'}^{N_p} A_{n'}\omega_{n'}(\Omega_n)\right) + N_D \ln\left(\int W(\Omega)\epsilon(\Omega)d\Omega\right) \\
&\quad + \ln(N_D!) - N_D \ln\left(\mathcal{L}\int W(\Omega)\epsilon(\Omega)d\Omega\right) + \mathcal{L}\int W(\Omega)\epsilon(\Omega)d\Omega \\
&= -\sum_{n=1}^{N_D} \ln\left(\sum_{n'}^{N_p} A_{n'}\omega_{n'}(\Omega_n)\right) + \cancel{N_D \ln\left(\int W(\Omega)\epsilon(\Omega)d\Omega\right)} \\
&\quad + \ln(N_D!) - N_D \ln\mathcal{L} - \cancel{N_D \ln\left(\int W(\Omega)\epsilon(\Omega)d\Omega\right)} + \mathcal{L}\int W(\Omega)\epsilon(\Omega)d\Omega.
\end{aligned}
\tag{2.24}
$$

Dropping the terms that don't depend on the parameters we get following equation:

$$
\boxed{\mathscr{E}\mathscr{L} = -\sum_{n=1}^{N_D} \ln\left(\sum_{n'}^{N_p} A_{n'}\omega_{n'}(\Omega_n)\right) + \mathcal{L}\sum_{n'}^{N_p} A_{n'}\int \omega_{n'}(\Omega)\epsilon(\Omega)d\Omega}. \tag{2.25}
$$

2.5 Acceptance×Efficiency

As seen in 2.22, the detector acceptance and selection requirement efficiency, sometimes referred to as acceptance×efficiency, enters into the log-likelihood function as N_p efficiency integrals:

$$
\epsilon_n = \int \omega_n(\Omega)\epsilon(\Omega)d\Omega. \tag{2.26}
$$

It is only required to calculate the ϵ_n acceptance coefficients, which we can estimate using the Monte Carlo simulation:

$$
\begin{aligned}
\epsilon_n = \int \omega_n(\Omega)\epsilon(\Omega)d\Omega &= \frac{\int \omega_n(\Omega)\epsilon(\Omega)d\Omega}{\int d\Omega}\int d\Omega \\
&= \langle\omega_n(\Omega)\epsilon(\Omega)\rangle \int d\Omega = 16\pi^2\langle\omega_n(\Omega)\epsilon(\Omega)\rangle.
\end{aligned}
\tag{2.27}
$$

The Monte Carlo simulators generate the requested dataset, which is then run through the detector simulation. The selection requirements are applied on top of the dataset, which has gone through the detector simulation to obtain the so called reconstructed data sample. In case of the uniformly distributed data sample the average of the $\omega_n(\Omega)\epsilon(\Omega)$ over this data could be calculated as the sum of the $\omega_n(\Omega_n^{RECO})$ averaged by the number of the events that has been generated N_{GEN}

$$\epsilon_n = 16\pi^2 \frac{\sum_{n'}^{N_{RECO}} \omega_n(\Omega_{n'})}{N_{GEN}}, \tag{2.28}$$

where N_{RECO} is the number of the reconstructed events (i.e. those survived the detector acceptance and selection requirements). The technical issue is that the Monte Carlo generators generally produce the *unweighted* dataset, distribution of which is not uniform, but rather distributed according to the proper PDFs involved. In this case, the sample can be converted into a flat distribution by parametrizing the distribution and reweighting it. The event weights then can be used similarly to calculate the ϵ_n acceptances:

$$\epsilon_n = 16\pi^2 \frac{\sum_{n'}^{N_{RECO}} \omega_n(\Omega_{n'})/p(\Omega_{n'})}{\sum_{n''}^{N_{GEN}} 1/p(\Omega_{n''})}. \tag{2.29}$$

To parametrize the $\Omega(\theta_Z, \varphi_Z, \theta_\ell, \varphi_\ell)$ distribution, I use the simple two dimensional polynomial fit in the $(\cos\theta_Z, \cos\theta_\ell)$ space, using the fact that azimuthal angle distributions are generated flat (Fig. 2.2)

$$\mathscr{F}(\cos\theta_Z, \cos\theta_\ell) = \sum_{i=0}^{P_1}\sum_{j=0}^{P_2} a_{ij} \cos^i\theta_Z \cos^j\theta_\ell. \tag{2.30}$$

In order not to require very high powers P_1 and P_2 and run into the problem of overfitting the distribution, I add the t-Channel correction function to the 2.30 fit function with fixed $M_Z = 91$ GeV and $M_{Z\gamma} = 140$ GeV. This procedure could be further improved, bringing P_1 power even lower, by noticing that $M_{Z\gamma}$ and $\cos\theta_Z$ are correlated in such a way that $M_{Z\gamma}$ is higher at the ± 1 edges of the $\cos\theta_Z$. But this further technical complication is avoided, because the final fit result without it is sufficiently good with χ^2s of 1680.76 and 1664.33 in electron and muon channels accordingly, over the 40×40=1600 bins and 33 free fit parameters (NDF = 1567). After appending fit function with Eq. 2.17 it is:

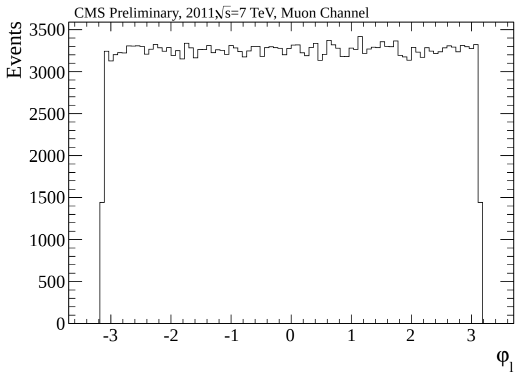

(a) Decay angle in muon channel

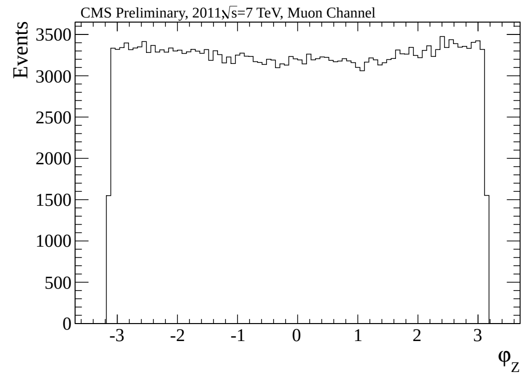

(b) Production angle in muon channel

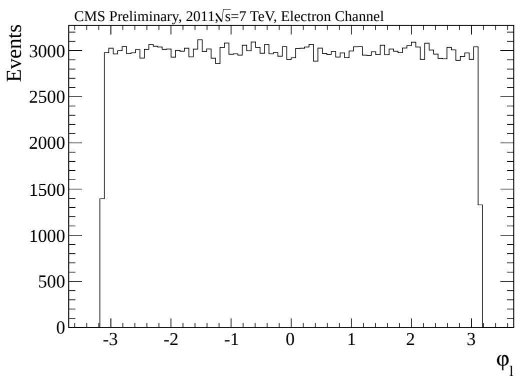

(c) Decay angle in electron channel

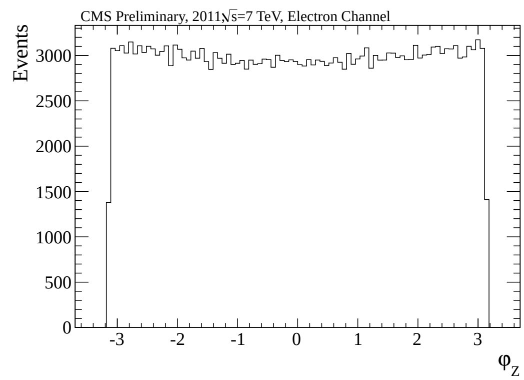

(d) Production angle in electron channel

Figure 2.2: Azimuthal angle distributions for the decay and production processed in the electron and muon channels.

$$\mathscr{F}(\cos\theta_Z, \cos\theta_\ell) = F(M_Z = 91\text{ GeV}, M_{Z\gamma} = 140\text{ GeV}, \cos\theta_Z) \sum_{i=0}^{P_1} \sum_{j=0}^{P_2} a_{ij} \cos^i\theta_Z \cos^j\theta_\ell. \tag{2.31}$$

The results of the fit are shown on Figs. 2.3 and 2.4 for each projection of the $\cos\theta_Z$vs.$\cos\theta_\ell$ distribution and a single bin slice projections accordingly. After the fit each event, for both generated and reconstructed event sets, is assigned the weight according $p = \mathscr{F}(M_Z = 91\text{ GeV}, M_{Z\gamma} = 140\text{ GeV}, \cos\theta_\ell, \cos\theta_Z)$. This weight is then used for calculating the ϵ parameters.

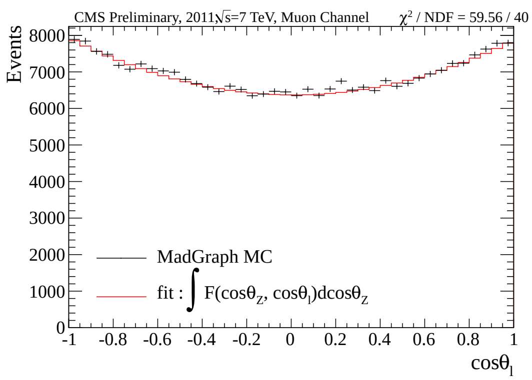

(a) Decay angle in muon channel

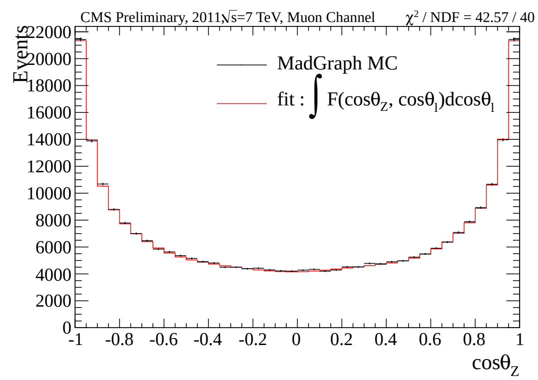

(b) Production angle in muon channel

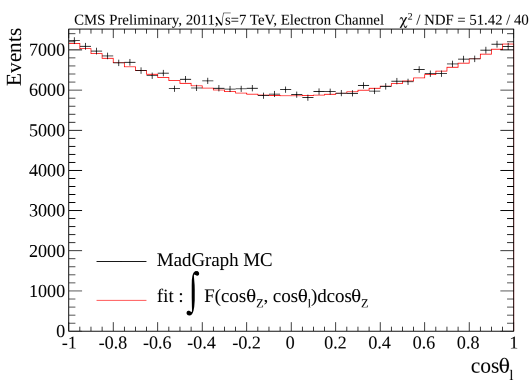

(c) Decay angle in electron channel

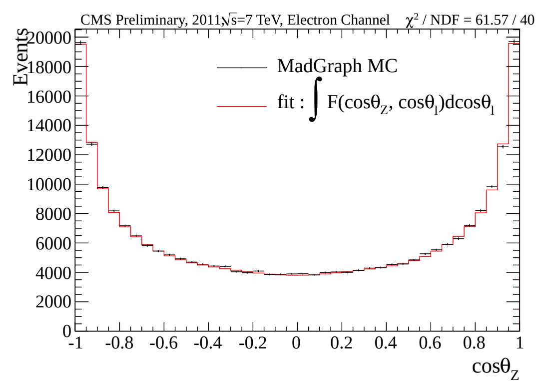

(d) Production angle in electron channel

Figure 2.3: Polar angle distributions for the decay and production processed in the electron and muon channels with the parametrization fits.

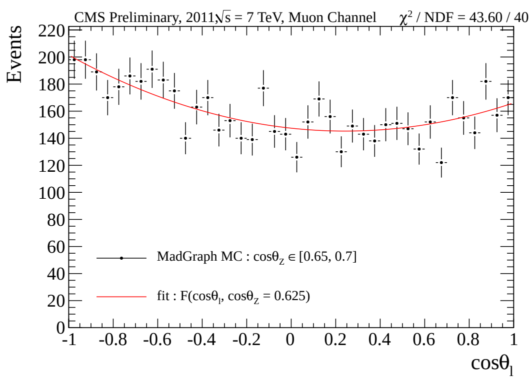

(a) Decay angle in muon channel

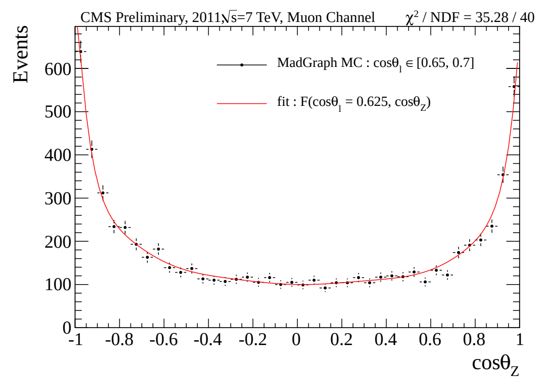

(b) Production angle in muon channel

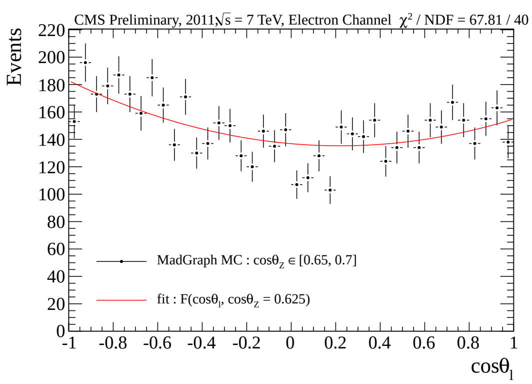

(c) Decay angle in electron channel

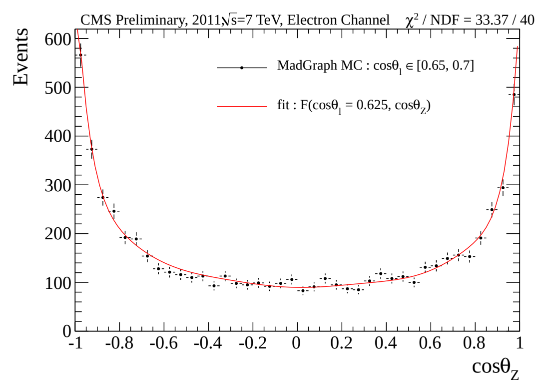

(d) Production angle in electron channel

Figure 2.4: Slice of the two dimensional polar angles distributions in both angles while the other one is in particular bin range.

Chapter 3

The Large Hadron Collider and Compact Muon Solenoid

This chapter presents an overview of the experimental facilities used for the data acquisition and analysis for this thesis. The particle accelerator and the main detector components are described. The barrel pixel detector is reviewed in more detail, since I spent a year on its testing, commissioning and calibration at the Paul Scherrer Institute in Zurich, Switzerland before its insertion into the core of the CMS detector and at CERN after.

3.1 The Large Hadron Collider

The Large Hadron Collider (LHC) is a synchrotron accelerator facility designed to deliver proton-proton collisions at $\sqrt{s} = 14$ TeV center-of-mass energy with nominal instantaneous luminosity of $\mathcal{L} = 10^{34}$ cm^{-2}s^{-1}. Due to the unprecedented running conditions the LHC started operating with a lower energy in 2009. In 2011 the operating center of mass energy was 7 TeV, which resulted in 5 fb^{-1} integrated luminosity used in this analysis. Producing the highest energy and luminosity ever studied, its main goal is to explore the physics above the electroweak symmetry breaking (EWSB) energy scale.

The LHC storage ring is installed in the pre-existing 26.7 km tunnel of its predecessor, the Large Electron-Positron Collider (LEP), near Geneva, Switzerland. The accelerator facility is hosted by the European Center for Nuclear Research (CERN). Circular colliders are limited by the synchrotron radiation that is estimated by the following formula for relativistic particles: $-\Delta E_{sr} = \frac{4\pi\alpha}{3R}\beta^3\gamma^4$; where $\beta = \frac{v}{c} \approx 1$; $\gamma = \frac{E}{mc^2}$; R is the radius of the accelerator; E, m and v are the energy, mass and the speed of the particle, respectively; and α is the fine structure constant. As already mentioned, the LHC is using the existing LEP tunnel, so the radius is the same, but due to the proton's mass being $\sim$ 2000 times larger than that of an electron, the energy loss of the LHC through synchrotron radiation is $\sim 16 \cdot 10^{12}$ less than for LEP. So, the proton-proton collision energy becomes limited by the magnetic field necessary to keep particles in the orbit.

There are 1,232 superconducting NbTi dipole magnets at the LHC, which bend the counter-rotating proton beams in two separate rings, needed due to the same charge of the colliding particles, unlike the case for the proton-antiproton collider at Tevatron, Fermilab. These magnets produce a nominal dipole magnetic field of 8.33 T. They are cooled by superfluid helium II, which requires temperatures below 2 K. At high energy proton-proton collisions actually reflect collisions of their constituent quarks and gluons, which carry only a part of the beam energy. Thus, in contrast to elementary particle colliders, to probe processes at a TeV scale the LHC has to provide collisions of multiple TeV protons. Given the magnetic field of dipole superconducting magnets, the LHC can deliver 7 TeV energy proton beams that result in $\sqrt{s} = 14$ TeV center-of-mass energy.

Each beam consists of a train of bunches of protons with 25 ns separation and $> 10^{11}$ protons in each bunch. This results in a bunch crossing frequency of 40 MHz and 3,564 bunches per beam. To account for the time needed to ramp up or down kicker magnets, needed for injection of the SPS beam into the LHC, some bunches are empty, so total of 2,808 bunches are filled per beam. The large number of protons in each bunch leads to a high rate R of pp inelastic collisions, also known as minimum bias events, which can be estimated using the following equations:

$$R = \sigma_{mb}\mathcal{L}; \quad \mathcal{L} = f\frac{n_1 n_2}{4\pi\sigma_x\sigma_y}, \tag{3.1}$$

where, σ_{mb} is the pp inelastic collision cross-section, which is at the order of few millibarns, n_1 and n_2 are the number of protons in each colliding bunch, σ_x and σ_y are the Gaussian transverse widths of the beam profile. For the nominal running conditions of the LHC, Eq. 3.1 yields $\sim 20 - 30$ interactions per bunch crossing, a phenomena known as "pile-up". These events are superimposed on top of the interesting events with much smaller rate (e.g. cross-section of the $Z\gamma$ production in electron channel is about 5.2 pb, thus nine orders of magnitude smaller then σ_{mb}). The high bunch crossing frequency and high pile-up conditions require a detector with very high time and spacial resolution.

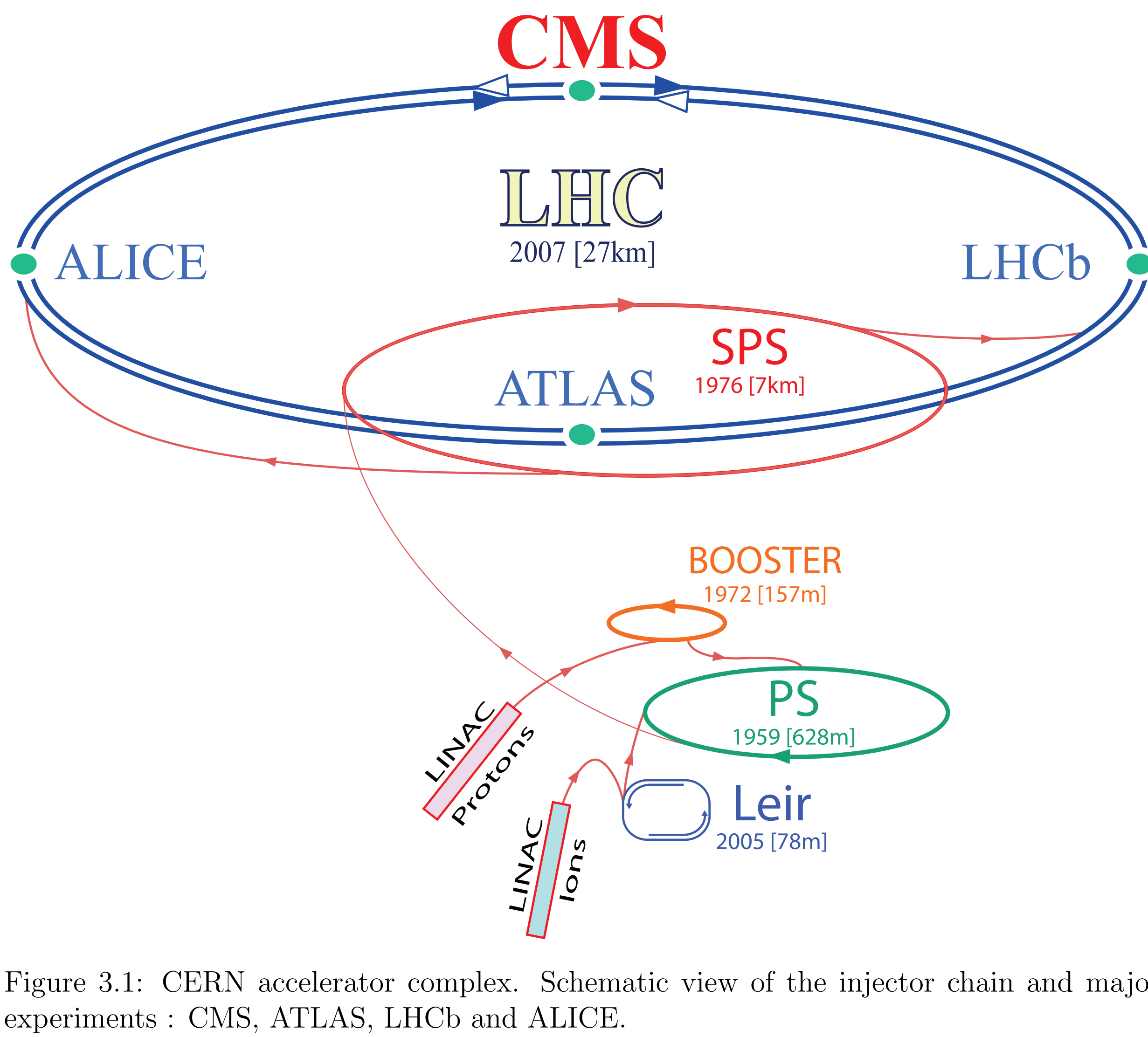

Figure 3.1: CERN accelerator complex. Schematic view of the injector chain and major experiments : CMS, ATLAS, LHCb and ALICE.

To accelerate protons and produce proton-proton collisions, the LHC is supplied through the injector chain shown in Fig. 3.1. The linear accelerator (LINAC) accelerates protons to 50 MeV that are then injected into the Proton Synchrotron Booster (PSB) and then to the Proton Synchrotron (PS). The PS further accelerates protons and prepares the bunch structure with proper separation of 25 ns. Bunches then are injected into the Super Proton Synchrotron (SPS), which accelerates protons to an energy of 450 GeV and feeds them to the LHC ring. The LHC then provides further acceleration and high energy proton-proton collisions for four major experiments. Two of them, CMS and ATLAS, are multipurpose experiments addressing a wide range of physics topics. Another major experiment, LHCb, is designed to mainly focus on the physics of b-quarks and the study of CP violation and rare decays of c and b mesons. The fourth interaction point is at A Large Ion Collider Experiment (ALICE), which is focused on heavy ion collisions to study the quark-gluon plasma.

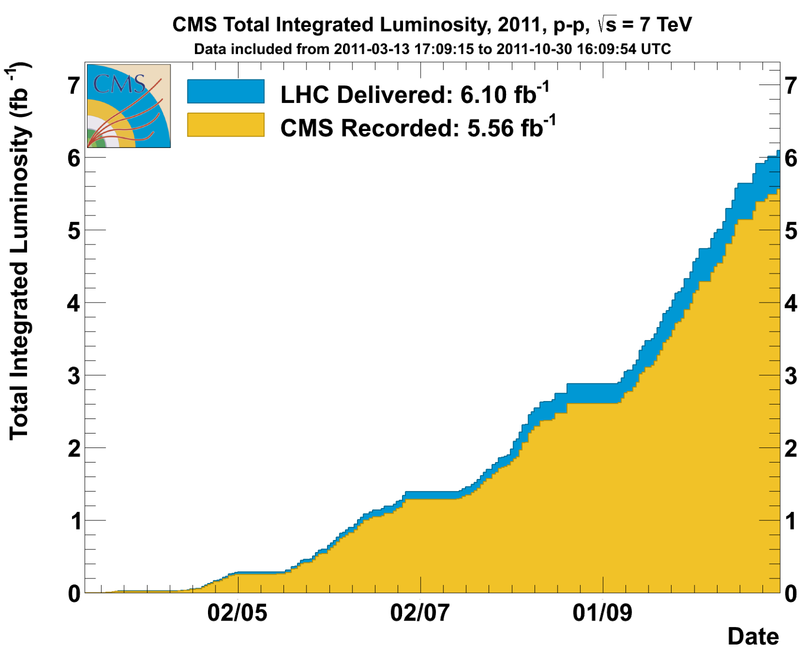

Figure 3.2: Integrated luminosity delivered by the LHC and recorded by the CMS vs. time [mm/dd] during 2011.

Proton beams are provided during periods called LHC Fills. When stable beams are achieved, experiments can take data. A single uninterrupted period of data-taking by the CMS is called a CMS Run. Successful operation of the LHC has resulted in over 5 fb^{-1} integrated luminosity in the year of 2011. This analysis is based on the data recorded by the CMS experiment during 2011 (Fig. 3.2). The analysis could be easily extended to the full data currently available once the correction factors described in Section 5.4 are calculated for the running condition of the LHC in the 2012.

3.2 Compact Muon Solenoid

CMS is a general purpose particle detector designed and built to work at LHC. It is situated at the LHC interaction point 5, on the French side of the CERN, about 100 meters underground. The main goal of the experiment is to shed light on EWSB and the existence of the Higgs boson, as well as to gain more insight into possible new physics, such as supersymmetry (SUSY) and models with extra dimensions. Searches for the Higgs boson and many of the new physics signatures require detecting muons in their final states, thus making good muon identification one of the key requirements for the detector. To meet this goal, the decision for CMS was made in favor of a high magnetic field and compact design. The harsh environment of the LHC, with its very high bunch-crossing frequency and pile-up requires a detector of high granularity and readout capability. All these aspects were considered in the designs of the CMS subdetectors.

CMS surrounds the interaction point with almost complete 4π solid angle coverage, which is essential for good missing transverse energy resolution. Weakly interacting neutral particles, such as neutrinos or hypothesized dark matter particles, escape the detector without any trace. The presence of these particles could be inferred from the momentum imbalance in the plane transverse to the beam and is described by the missing transverse momentum. Its magnitude is called missing transverse energy $\not\!\!E_T$ and is one of the main observables. It is the important discriminating factor between many interesting searches in-

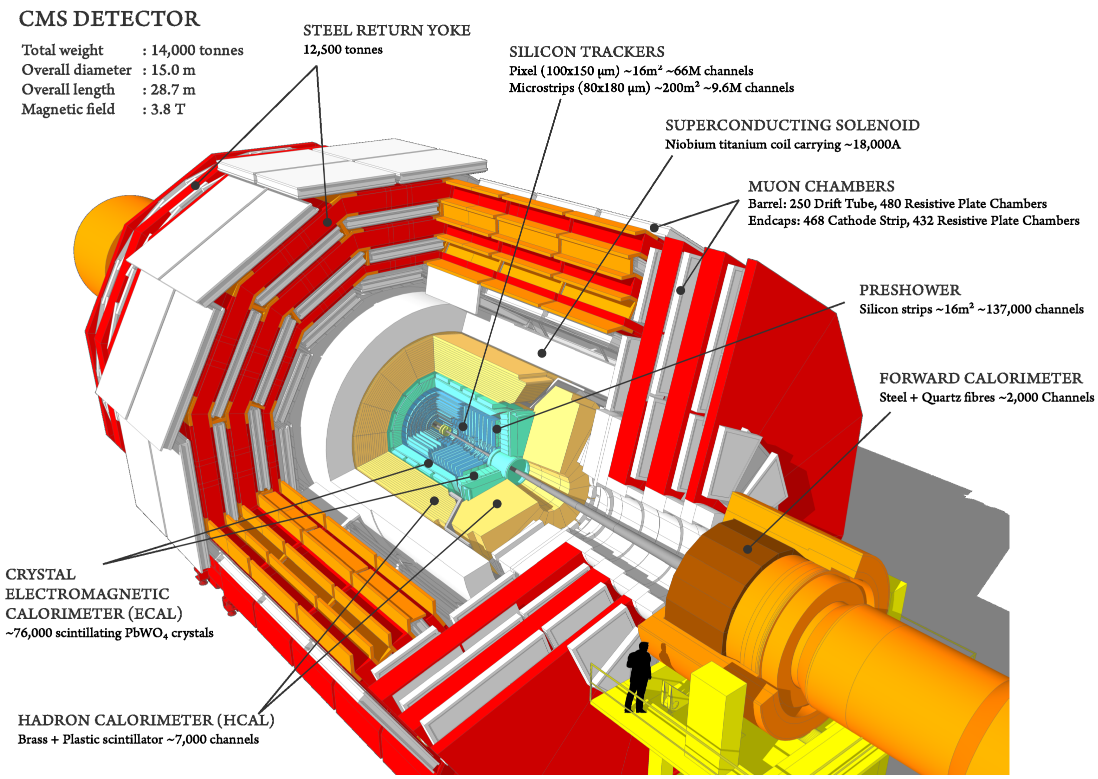

Figure 3.3: Sectional view of the CMS detector.

volving neutrinos from the background. The searches for many beyond the standard model theories, such as SUSY, involve new weakly interacting neutral particles thus depend on a good measurement of the $\not{E}_T$. The CMS is centered around the nominal collision point and has cylindrical symmetry. As a general purpose detector, CMS consists of a tracker system followed by calorimeters and muon detectors. High magnetic field is generated by the superconducting solenoidal magnet. Each subsystem consists of a cylindrical shell (barrel) and disk shaped parts, concentric with the beam pipe from both sides (endcaps) as shown in Fig. 3.3. High magnetic field is essential for particle charge identification and momentum resolution, which in CMS is ensured by the 3.8 T solenoid. High resolution of charged-particle momentum and efficient tagging of τ leptons and b-quarks require a very high granularity pixel detector to be located very close to the interaction point.

The CMS detector is 21.6 m long and has a diameter of 14.6 m. It has a total weight of

12,500 metric tons.

3.2.1 System of Coordinates

The convention for CMS is to have a right handed coordinate system with its origin in at interaction point and the orientation such that x axis points towards the center of the LHC ring, the y axis - vertically upward and, consequently, the z axis - along the counter-clockwise proton beam. In spherical coordinates: the radial coordinate is denoted by r. The polar angle θ is measured from the z axis in the $[0, \pi]$ range. The azimuthal angle φ is measured in the xy plane from the x axis within the $[-\pi, \pi]$ range (Figure 3.4).

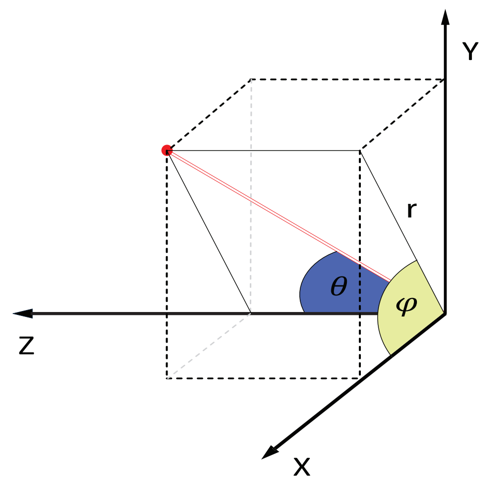

Figure 3.4: Cartesian and spherical systems of coordinates for the CMS.

From the physics point of view, a more useful parameter to describe the polar coordinate of particle tracks in the detector that is heavily used in high energy physics is pseudorapidity η defined as:

$$\eta = -\ln\left[\tan\left(\frac{\theta}{2}\right)\right]. \tag{3.2}$$

For massless particles, it reduces to a rapidity of the particle. At the LHC the number of particles produced per unit of pseudorapidity is roughly constant.

3.2.2 Superconducting Magnet

The single most important aspect for high performance physics results, and the key feature of the CMS detector, is the high magnetic field generated by the superconducting magnet. It is designed to produce a nearly homogeneous 4 T magnetic field in the free bore of 6 m diameter and 12.5 m length. With full operating current the cold mass of 220 tons stores 2.6 GJ of magnetic field energy. These factors, combined with the limited space for coil inside the detector, require great attention to the design, to avoid mechanical stresses. For this reason, it was expected that operational field would be slightly lower than the designed 4 T, and endeed, the working field strength is 3.8 T.

The magnetic flux is returned through a saturated iron yoke with a magnetic field of 2 T, comprised of 5 wheels in the barrel and 3 disks in each endcap. The yoke harbors the muon detector parts, coil and a cryostat. The weight of the yoke parts is 400 mt for the lightest and 1,920 mt for the heaviest, resulting in the total weight of 10,000 metric tons of iron yoke. The CMS design considers the ease of access to the parts of the detector. So to displace each element, a combination of heavy-duty air pads and grease pads are used in order to minimize the risk of transverse displacement or physical damage at closing.

The operational temperature of the superconducting magnet is extremely low, so the cool down has to be very slow to account for the mechanical deformation by the magnetic field and the shrinkage due to the cooling. The magnet was fully tested in 2006, the smooth cool-down to 4.6K took 24 days.

3.2.3 Pixel Detector

At high energy experiments, fundamental physics is derived by precisely identifying photons, muons, electrons and jets. One of the key aspects to succeed in doing so is track and vertex reconstruction of these particles in the strong magnetic field. The CMS tracking system is comprised of the pixel detector and silicon strip tracker (Section 3.2.4).

The CMS pixel detector provides high resolution measurements of particle tracks and is vital for secondary vertex reconstruction, which is necessary for precise b-tagging. Tagging of b-quarcks plays a major role for the Higghs boson and SUSY searches. At design luminosity the LHC will pierce the detector with about 1,000 particles every 25 ns. To deal with these conditions the pixel detector has to have a very high granularity, to keep the detector occupancy low, and very fast response time. It also has to satisfy a low material budget requirement to limit multiple scattering, bremsstrahlung, photon conversion and nuclear interactions of charged particles before they reach the outer tracker and calorimeters. High efficiency secondary vertex reconstruction requires the detector to be very close to the interaction point, thus making it a subject to extreme radiation conditions. To meet the above requirements the CMS pixel detector uses silicon as the only active material.

The CMS pixel detector covers the pseudorapidity range of $|\eta| < 2.5$, and consist of 66 million readout channels distributed in three barrel layers and two endcap disks on each side. The overall detector layout is shown in Fig. 3.5.

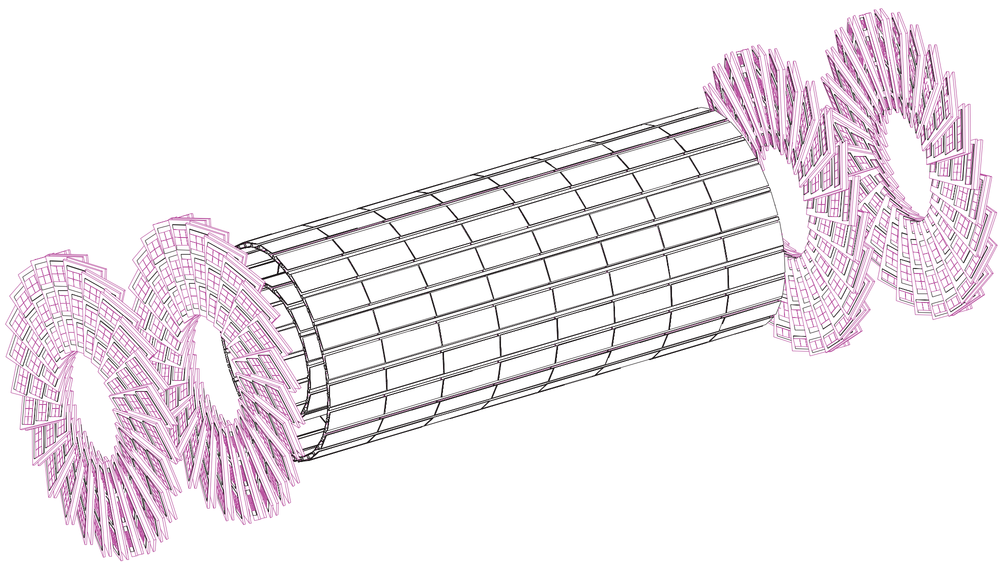

Figure 3.5: Schematic view of the CMS pixel detector.

Barrel Pixel Detector

The Barrel Pixel Detector (BPIX) has three layers at 4.4 cm, 7.2 cm and 10.2 cm radii from the proton beam. It has a total of 768 highly segmented silicon pixel detector modules. Very high track resolution in both rz and $r\varphi$ direction is achieved by about 48 million readout channels from the 100 μm$\times$150 μm size pixels. The modules are mounted to carbon-fiber ladders from which the six half shells (two for each layer) of the barrel layers are constructed. Ladders are arranged in an overlapping geometry as shown in Figure 3.6.

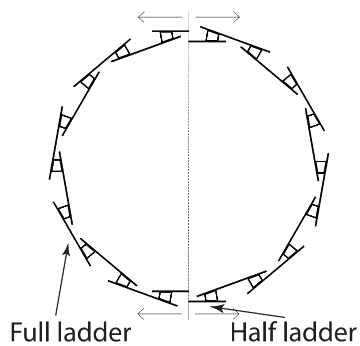

Figure 3.6: Schematic cross-section of the barrel layer showing the geometric structure of the ladders.

The BPIX is attached to 2.2 m long supply tubes, which carry the electrical and optical signals as well as cooling lines, along the beam pipe. Supply tubes are outfitted with the electronics for the detector readout and control.

BPIX Module: There are two types of modules in the barrel, standard modules containing 16 ReadOut Chips (ROC) and half modules containing 8 chips. Figure 3.7 shows the components of the barrel module. Each ROC on the module is bump-bonded to the $52 \times 80 = 4,160$ sensor pixels using indium bumps. On the other side of the silicon sensor a high density interconnect (HDI) circuit is glued and wire-bonded to the ROCs. On top of HDI sits a token bit manager (TBM) that controls the readout from the ROCs. From the ROC side of the module two base strips, made of 250 μm thick silicon nitride (Si_3N_4), are glued to provide the necessary mechanical rigidity and cooling, and to mount the module to the barrel structure.

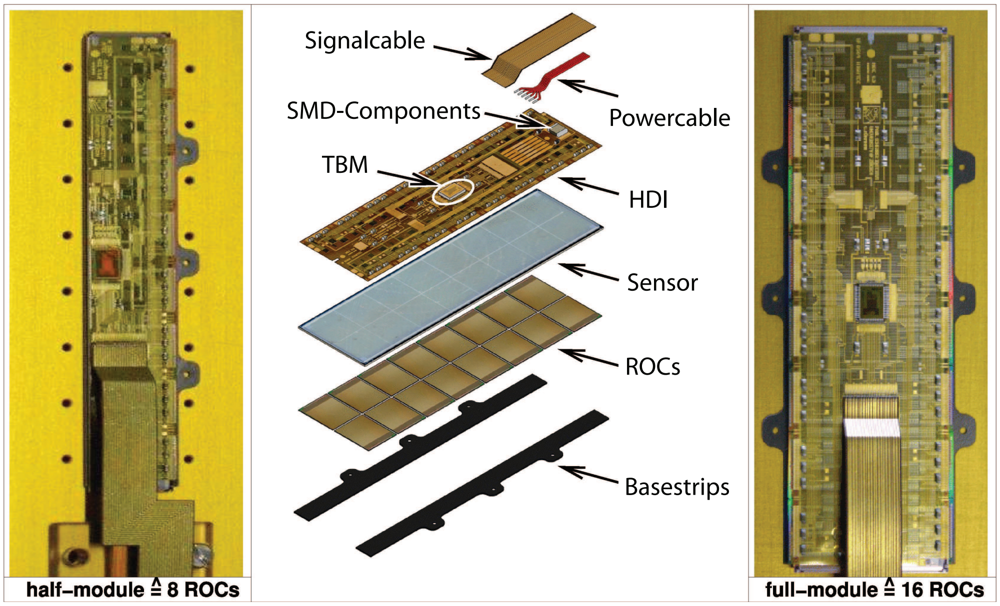

Figure 3.7: Exploded view of a barrel pixel detector module.

A Summary of the main properties of a barrel module is given in Table 3.1.

Size	66.6 mm×26mm
Weight	3.5 g
Number of ROCs	16
Number of Pixels per ROC	52×80 = 4,160
Pixel size	100 μm×150 μm
Sensor thickness	285 μm

Table 3.1: Properties of the full CMS BPIX modules.

BPIX ROC: (Fig. 3.8) The bump-bonding connects each silicon pixel to a ROC pixel unit cell (PUC). The PUCs are arranged in 26×80 double columns and are controlled by the double column periphery. The ROC records and stores the position of each pixel with 25 ns time resolution by the means of double columns, double column periphery, and chip periphery. The ROC is controlled by 26 40 MHz programmable, digital-to-analog converter (DAC) registers.

BPIX TBM: All the ROCs of the module are controlled by a single TBM. Its main

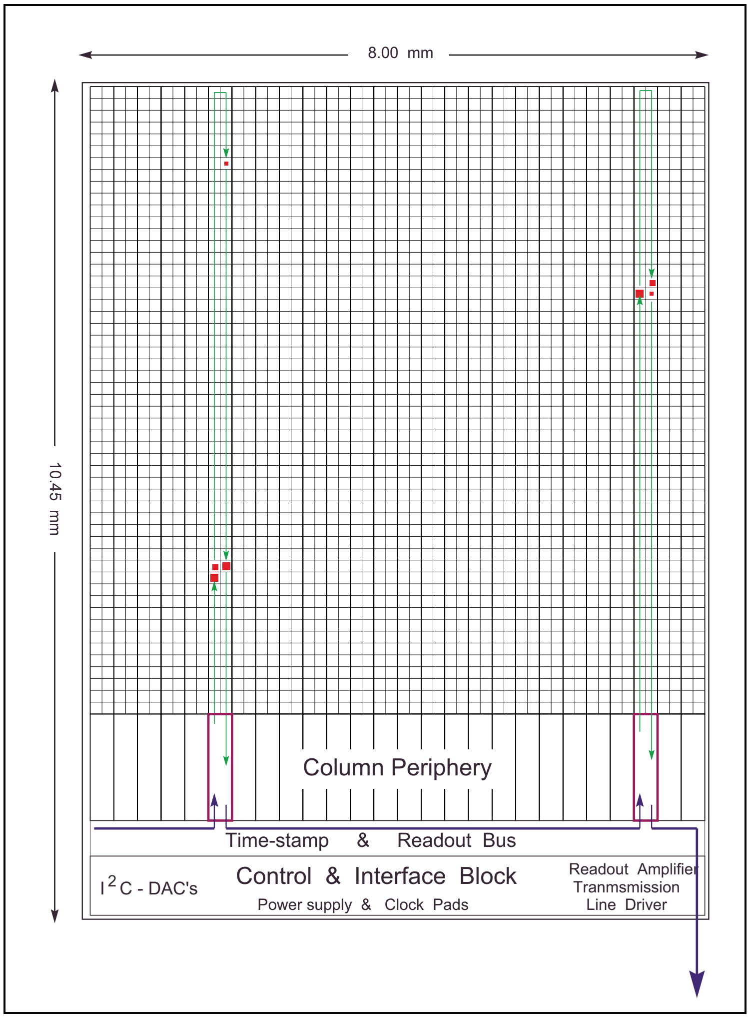

Figure 3.8: Conceptual layout of the BPIX readout chip.

function is to synchronize data transmission. Once an L1 trigger is received by the TBM, it issues a readout token to the ROCs and initializes readout. The last ROC, in the readout chain sends the readout token back to the TBM, which multiplexes the signal, adds a header and a trailer, and sends the signal through the readout link. The TBM also distributes the clock to the ROCs.

Forward Pixel Detector

The pixel detector endcap sections or the forward pixel detector (FPIX), consists of two disks on each side of the BPIX. It is installed inside the supply tube at 34.5 cm and 46.5

cm from the interaction point. Each disk is split into two parts, called half-cylinders, so the detector can be mounted around the beam pipe. Modules of the FPIX are called *plaquettes* and are attached to trapezoidal *panels*. The support structure of the FPIX is arranged into *blades*. Each blade has a panel attached from on its both sides. In order not to leave gaps in between plaquettes when covering the trapezoidal panels of the FPIX, there are several types of plaquettes depending on the number of raws and columns of the ROCs on them (raw$\times$column : 1$\times$2, 2$\times$3, 2$\times$4, 1$\times$5, 2$\times$5). There are 24 panels and 12 blades in each half-disk, with a total of 672 plaquettes.

3.2.4 Silicon Strip Tracker

At radii above 20 cm, the reduced particle flux (hit rate $\sim$ 60 kHz/mm^2) allows the use of a silicon micro-strip detector. At the LHC nominal operation conditions, with the typical cell size of 10 cm$\times$80 μm, occupancy can be kept under 2-3%. For the layers further from the collision point, the strip pitch can be increased keeping the occupancy low, however the strip capacitance, hence the electronics noise, will also increase with its length. So, for the intermediate radii, the CMS detector is equipped with the silicon strip tracker (SST), making CMS the first experiment equipped with a fully silicon tracker in the outer region. The SST is designed to deal with harsh conditions of the LHC and keep the tracker occupancy low. At the same time it satisfies all the requirements of high position resolution, radiation hardness and fast response time.

The SST is comprised of three different subsystems, tracker inner barrel and disks (TIB/TID), tracker outer barrel (TOB) and tracked endcaps (TEC). It occupies the radial region between 20cm to 119cm. The schematic layout of the entire tracker system is shown on Fig. 3.9.

The TIB/TID consists of four concentric barrel layers and three disks on each side. Barrel layers are at 25.5 cm, 33.9 cm, 41.85 cm, and 49.8 cm from the beam line. Discs are divided into three concentric rings and are placed between 80 cm and 90 cm from the

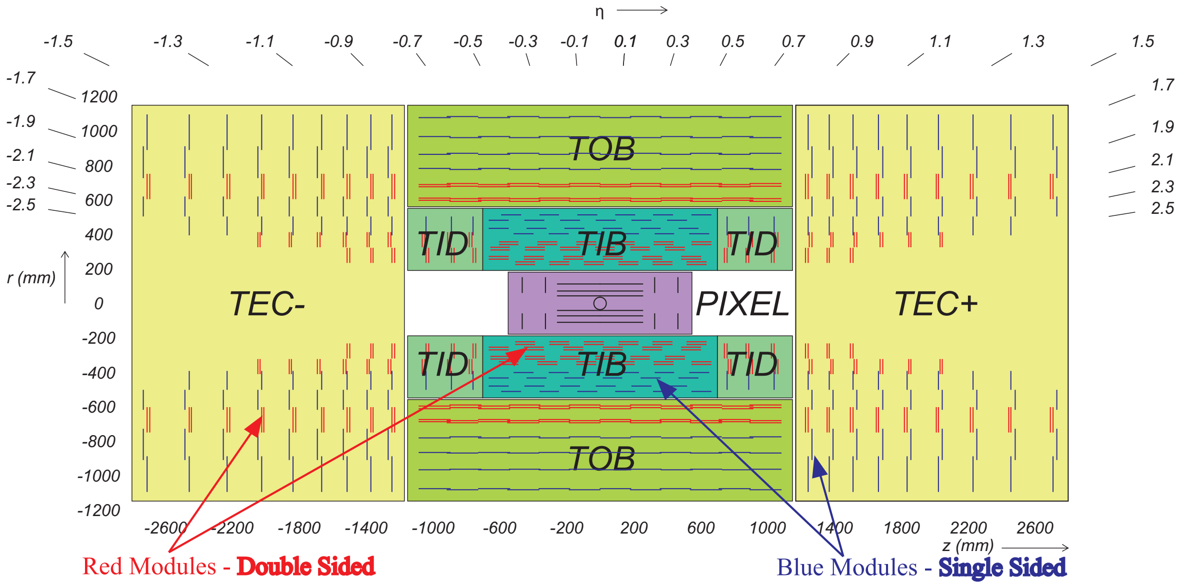

Figure 3.9: Schematic view of the CMS traker system.

interaction point on each side. Outside of the TIB/TID is the tracker outer barrel, which is arranged in three inner and three outer layers of sensors. It has a radius of 116 cm and extends to ±118 cm in the z direction. Beyond this range in the z direction are stationed 9 disks of the TEC. They cover the region of 124 cm$< |z| <$ 282 cm and 22.5 cm$< |r| <$ 113.5 cm. These disks are divided into concentric rings. Seven rings make up the innermost disk, and four constitute the outermost one. The SST provides pseudorapidity coverage of $|\eta| < 2.5$.

These four subsystems of the silicon tracker comprise a total of 15,148 detector modules made of 24,244 single-sided p-on-n type silicon sensors. The TIB/TID and four inner rings of the TEC, being closer to the interaction point and experiencing higher particle rates, use thin 320 μm sensors, whereas the outer parts of the tracker, the TOB and the three outer rings of the TEC, use thicker 500 μm sensors. Sensors in the modules are positioned in such a geometry that they provide very high precision measurement of r-φ and r-z coordinates in the barrel and endcaps respectively. In addition, the modules in the first two layers and rings of TIB/TID and TOB, as well as TEC rings 1,2 and 5 are double-sided. In these modules, micro-strip detectors are mounted back-to-back with a stereo angle of 100 mrad, this provides a measurement of the third coordinate (z in the barrel and r on the disks).

The SST geometry described above provides at least ~ 9 hits, with at least 4 of them being two-dimensional module measurements per track (Fig. 3.10). This ensures very high quality track reconstruction.

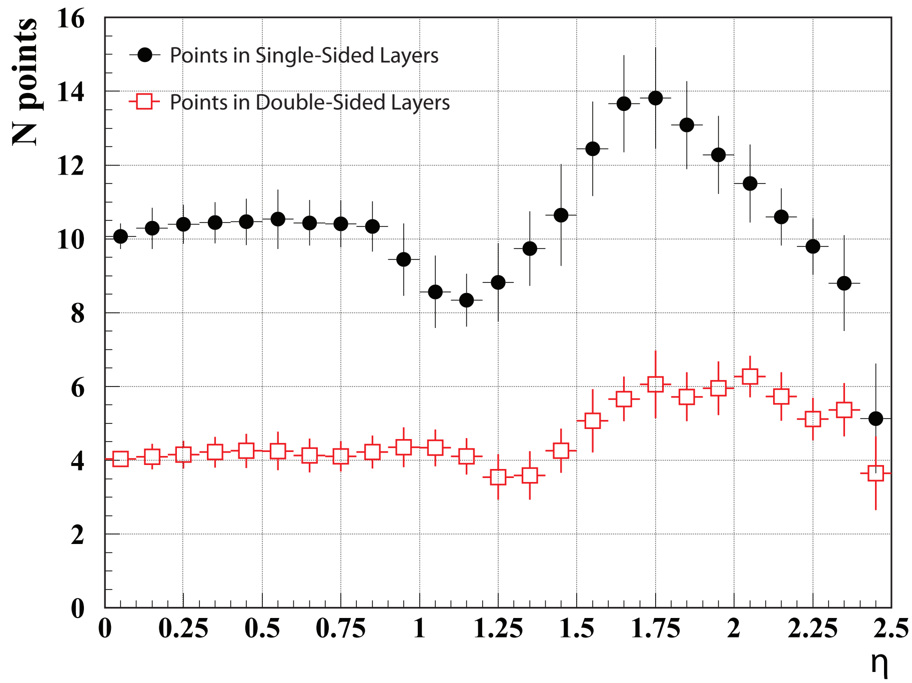

Figure 3.10: Number of measurement points in the SST as a function of pseudorapidity.

3.2.5 Electromagnetic Calorimeter

The electromagnetic calorimeter measures the energies of electrons and photons with very high precision. It is a hermetic homogeneous calorimeter made of lead tungstate ($PbWO_4$) crystals. High density (8.28 g/cm^3), small radiation length X_0 (0.89 cm) and small Molière radius R_M (2.2 cm) of the lead tungstate result in a compact size of the ECAL with very high granularity. It also ensures better shower position resolution and better shower separation due to a smaller degree of shower overlaps. Material choice was also based on the radiation hardness and fast response time of the $PbWO_4$. Its scintillation decay time is of the order of magnitude of the LHC bunch crossing time. About 80% of the light is emitted in 25 ns. The light yield of these crystals is relatively low, about 4.5 photoelectrons per MeV at nominal operation temperature of 18°.

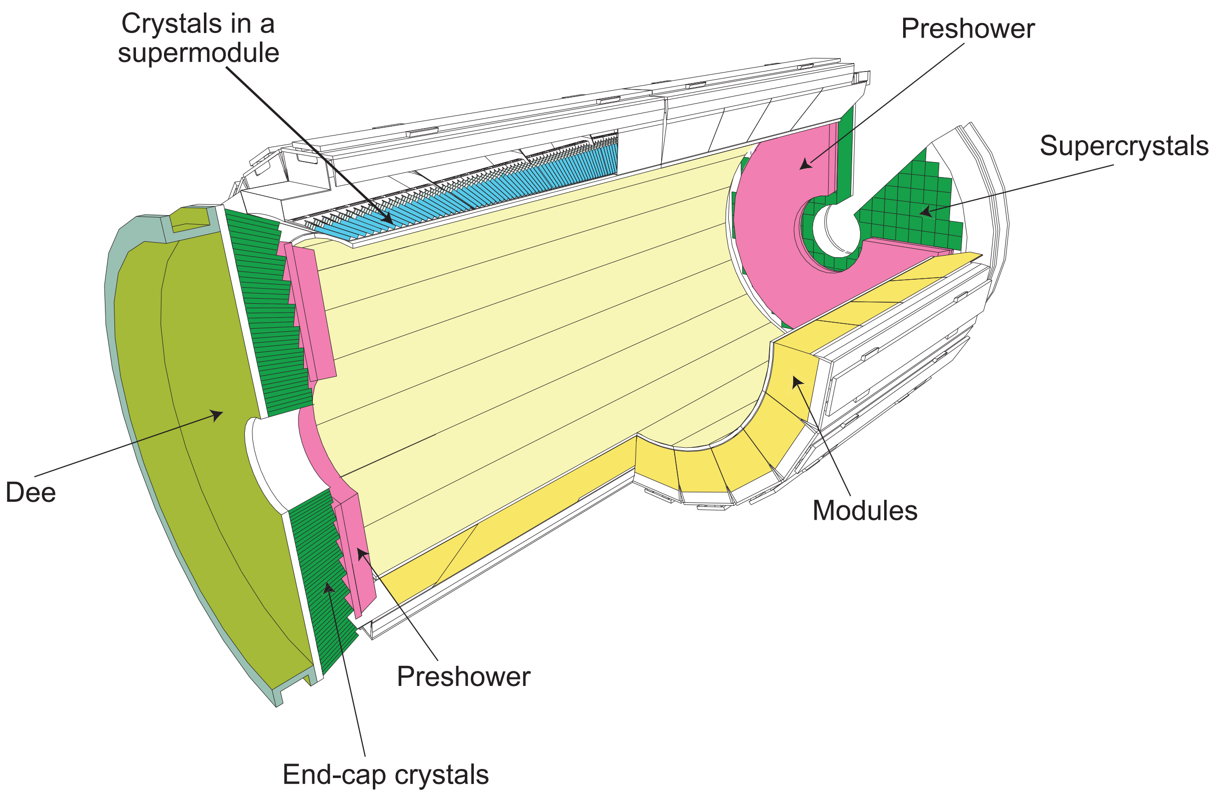

Figure 3.11: Layout of the CMS ECAL, showing the arrangement of crystal modules, supermodules and endcaps, with the preshower in the front.

The barrel part (EB) of ECAL consists of 61,200 crystals that are oriented radially in a quasi-projective geometry. To avoid gaps, the crystals have a tapered shape and are tilted by a small angle (3°) with respect to the radial direction. The resulting cross-sectional areas are $\sim$22$\times$22 mm^2 at the front face of crystal, and $\sim$26$\times$26 mm^2 at the rear face. Each crystal is 230 mm long or 25.8 radiation lengths. The front face of the crystals is at the radius of 1.29 m from the beam line. The EB covers the pseudorapidity range $|\eta| < 1.479$. Due to the high magnetic field and low light yield from the crystals, conventional photomultiplier detectors were replaced by avalanche photodiodes (APDs) for barrel crystals.

The ECAL endcaps (EE) are positioned 316 cm from the interaction point. The endcaps consist total of 7,324 crystals that are grouped into units of 5×5 crystals (supercrystals or SCs). The crystals and SCs are arranged in a grid, with the crystals tilted few degrees $(2 - 8°)$ to point at a focus 1.3 m beyond the interaction point. Each crystal has an area of 28.63×28.62 mm^2 at the front face and 30×30 mm^2 at the rare face, with 220 mm length, that corresponds to 24.7 radiation lengths. The EE covers the pseudorapidity range of $1.479 < |\eta| < 3.0$, thus leaving a little crack in between the barrel and the endcap. In the endcaps, vacuum phototriodes (VPTs) are used as photodetectors.

A preshower detector (ES) is placed in front of the ECAL endcaps. The main aim of the ES is to help identify neutral pions in the endcaps. It also helps to separate electrons from minimum ionizing particles (e.g. cosmic rays), and improves the position resolution of electrons and photons. The ES has a thickness of $3X_0$ and covers a presudorapidity range of $1.653 < |\eta| < 2.6$.

The energy resolution of the ECAL was studied in the CERN H4 electron test beam measurements. The typical energy resolution for the EB crystals was found to be:

$$\left(\frac{\sigma}{E}\right)^2 = \left(\frac{2.8\%}{\sqrt{E}}\right)^2 + \left(\frac{0.12}{E}\right)^2 + (0.3\%)^2, \tag{3.3}$$

where the first term is stochastic; the second is due to electronic, digitization and pileup noise; and the third is a constant term due to the non-uniformity of the longitudinal light collection, intercalibration errors and leakage of energy from the back of the crystal.

3.2.6 Hadron Calorimeter

The LHC is a hadron-hadron collider that produces an unprecedented amount of hadronic activity in the CMS detector. Having a good hadron calorimeter (HCAL) is particularly important to measure hadronic jets, and it should have near 4π coverage to efficiently measure the imbalances in transverse energy $\not{E}_T$ to indirectly detect neutrinos or other exotic particles that leave detector without interacting.

The design of the HCAL is driven by the desire to put it inside the solenoid and maximize the pseudorapidity coverage without compromising the performance. To achieve this goal it consists of: the barrel part (HB), which is radially restricted from inner side by the ECAL and outer side by magnet solenoid ($1.77 < r < 2.95$) and covers range $|\eta| < 1.3$; the outer part (HO), which extends the HB outside the solenoid and supplements it to ensure the adequate sampling depth that is otherwise restricted by the material that could be put inside the magnet; and the endcaps (HE), which cover the psudorapidity range $1.3 < |\eta| < 3$ and forward calorimeters, wchich are placed at 11.2 meters from the interaction point and extend the angular coverage to $|\eta| = 5.2$.

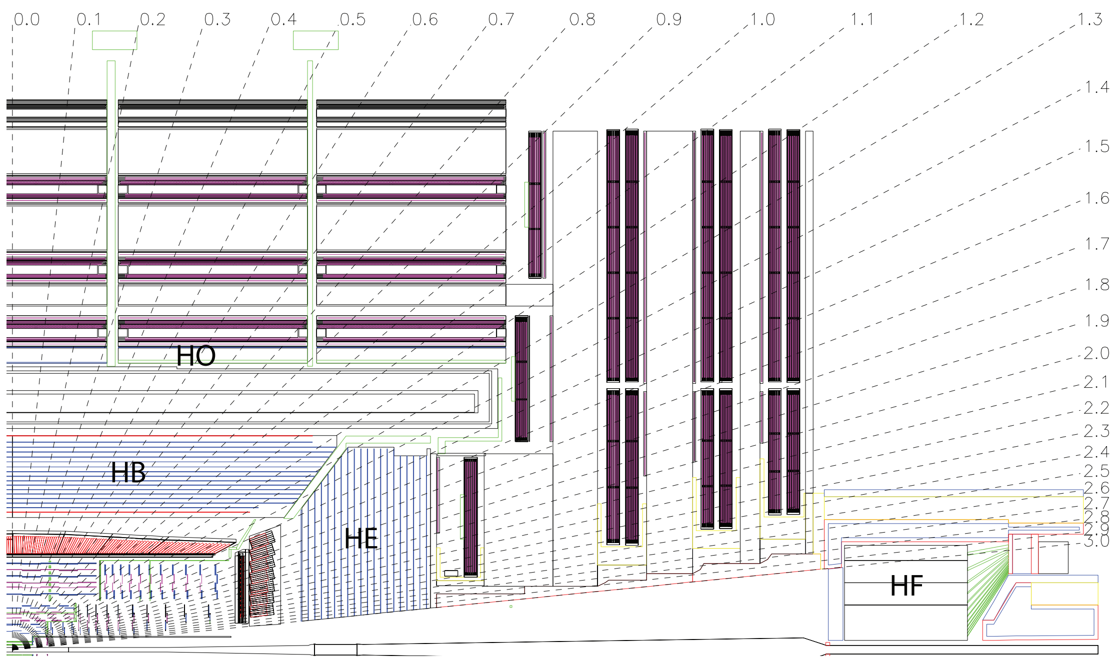

Figure 3.12: Longitudinal section of the CMS HCAL, showing the arrangement of the layout of the HB, HE, HO and HF components.

The HB and HE consist of layers of steel and brass (70% Cu, 30% Zn) absorber material and an active medium. Total absorber length for calorimeters including electromagnetic is about ten interaction lengths ($10\lambda_I$). The active material consists of plastic scintillator tile and wavelength shifting fiber to bring out the light. There are about 70,000 tiles in the CMS HCAL, which are grouped into a single mechanical scintillator tray unit for each layer.

Layers are arranged in a projective geometry with fine granularity to provide good di-jet separation and mass resolution.

The HO, a *tail catcher* part of the hadronic calorimeter, is placed outside of the solenoid in the 75 mm thick stainless steel beam structure of the return yoke and further extends the depth of the HCAL system to $11.8\lambda_I$. It utilizes the solenoid as an absorber material and is used to identify late starting showers.

The necessity to survive extremely harsh conditions of the LHC is the most important aspect of the forward calorimeter. It has to withstand $\sim$750 GeV of deposited energy per proton-proton interaction and extremely high charged hadron fluence of $10^{11}\mathrm{cm}^{-2}$. This puts very strict requirements on the active material. To deal with such a hostile environment, quartz fibers were chosen as active medium. These are inserted in the grooves of the steel absorber plates. They detect Cherenkov light, thus making the HF mostly sensitive to the electromagnetic component of the hadron shower. The design of the HF structure allows to align it within 1 mm with respect to the rest of the CMS experiment.

3.2.7 Muon Detector System

Muon, being the "middle name" of CMS, is the most important particle to be detected at the experiment. Muons are present in the Higgs boson decay *golden channel* $H \rightarrow ZZ \rightarrow 4\mu$ and in many final states of possible SUSY objects. High precision measurement of muon momentum is achieved by the combination of the high magnetic field, central tracker and the muon detection system.

The CMS muon detector was designed to have high pseudorapidity coverage and serve the purpose of muon identification, momentum and charge reconstruction, and triggering, over the full kinematic range of the LHC. It consists of three types of gaseous detectors, which are embedded into a return yoke structure.

Drift Tubes

The barrel part of the muon detector is characterized by a relatively small neutron-induced background, low muon rate, and a uniform magnetic field that is mostly contained in the steel structure of the return yoke. This allows for successful usage of regular drift chambers. The CMS drift tube (DT) chambers are filled with gas mixture of 85% Ar and 15% CO_2, and cover the pseudorapidity range of $|\eta| < 1.2$. The DTs are arranged in four concentric cylinders. The three inner cylinders consist of 60 drift chambers each, and the outer one has 70 chambers. There are about 172,000 sensitive wires, which are arranged perpendicular to each other so that DTs can measure muon position in r-φ or z direction. This results in a fine granularity of muon system with the position resolution of about 100 μm in both $r\varphi$ and rz directions.

Cathode Strip Chambers

In contrast to the barrel region, in the muon endcaps, which span the pseudorapidity range of $0.9 < |\eta| < 2.4$, the muon rate and background level are very high, so they use cathode strip chamber (CSC) technology, which has superior radiation hardness and faster response time compared to the DTs. Each endcap consists of four CSC stations, which are positioned perpendicular to the beam line in the disks of the return yoke. By combining measurements from the cathode strips that run radially outward and anode wires perpendicular to the strips, CSCs give the position of muons in r-φ-η coordinates along with the beam-crossing time of the muon. Position resolution in the encaps is about 80-85 μm.

Unlike the ECAL, the geometry of the muon barrel and endcaps doesn't leave any gaps. This allows for muon reconstruction over polar angles of $10° < \theta < 170°$

Resistive Plate Chambers

An important characteristic of the muon system is its ability to trigger on muons independent of the rest of the CMS. In order to enhance triggering capability, mostly in the barrel region where eventual rise in the background rate can cause the high occupancy in the DTs (with a drift time of 380 ns), the resistive plate chambers (RPC) are added to both, barrel and endcap regions. The RPCs compose a complementary trigger system that provides time resolution of about 1 ns over the pseudorapidity range of $|\eta| < 1.6$. They are double-gap chambers that operate in an avalanche mode. Besides the fast triggering capability, the RPCs provide additional position resolution to help to resolve ambiguities in the track reconstruction from multiple hits in a chamber. Two layers of RPCs are embedded in each of the first two stations of barrel region, providing triggering capability even on low transverse momentum muon tracks that don't reach the outer layers. There is a plane of RPCs in each of the first three stations of the endcap region, which by using coincidences between stations, helps reduce background and improve time resolution for bunch-crossings.

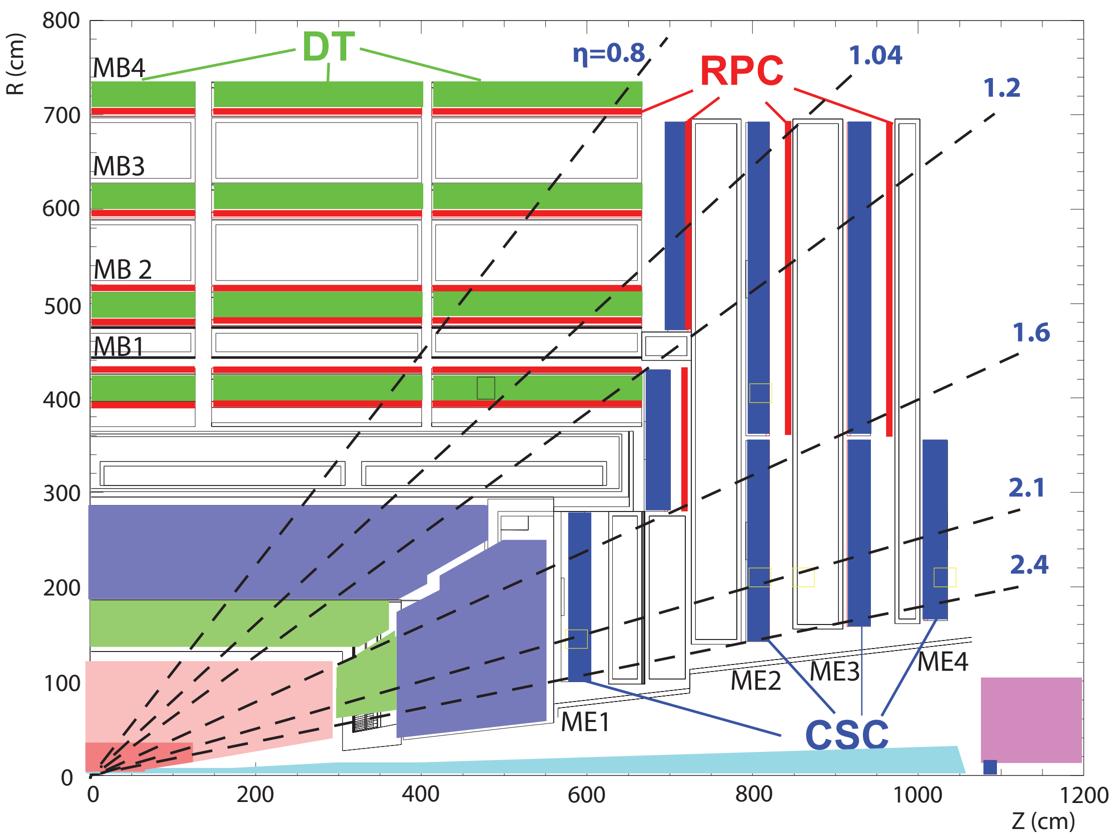

Figure 3.13: Sectional view of the CMS muon detector system showing the locations of DTs, CSCs and RPCs.

3.2.8 Forward Detectors

In addition to the main CMS subdetectors described above, there are two more calorimeters installed at the very forward regions of the CMS: CASTOR detector and ZDC. They cover the pseudorapidity range of $5.2 < |\eta| < 6.6$ and $|\eta| > 8.3$ respectively. As mentioned earlier, the forward regions experience very high radiation rates, therefore radiation hardness is a driving feature for the forward calorimeters. They are quartz-tungsten sampling calorimeters, thus ensuring their radiation hardness, fast response time, and compact size.

3.3 Trigger System

The amount of the collision data produced by the LHC is extremely high, and it is impossible to store all of it. Plus, most collisions produce known physics of little interest. Drastic reduction of the data amount for storage and further physics analysis is done by the trigger system. The trigger system at the CMS is composed of two parts, the level 1 (L1) trigger and high level trigger (HLT). Combined, they decrease the LHC's nominal 40 MHz data production frequency by about factor of 10^6.

The L1 trigger system consists of largely programmable electronics, based on the FPGA technology where possible, and on custom programmed ASICs (application-specific integrated circuit) and programmable memory lookup tables (LUT) - where speed and radiation hardness become important. The design output rate of the L1 trigger is 100 kHz, which can be handled by the HLT for the final decision of storing the data. The L1 has to consider every bunch-crossing and make decision within 2.3 μs, while keeping the high resolution data pipelined in the memories of the front-end electronics of the subdetectors. It is split into three components: local, regional and global. The local L1 trigger is based on the track pattern information received from the muon chambers and energy depositions in the trigger towers of the calorimeters. Using pattern logic, this information is combined and ranked as a function of energy and momentum. The rank is reflective of the quality and confidence of the L1 parameter measurements, based on detailed knowledge of the detectors and trigger electronics and on the amount of the information available. Global triggers receive information from the global muon trigger and global calorimetric trigger, which on their side determine the highest ranked objects from the entire detector. The decision about accepting or rejecting the event is based on the algorithm calculations and the readiness of the sub-detectors and data acquisition system (DAQ), which is determined by the trigger control system(TCS). The decision of the L1 is communicated back to the subdetectors by the timing, trigger and control (TTC) system. The architecture of the L1 trigger system is shown on Figure 3.14.

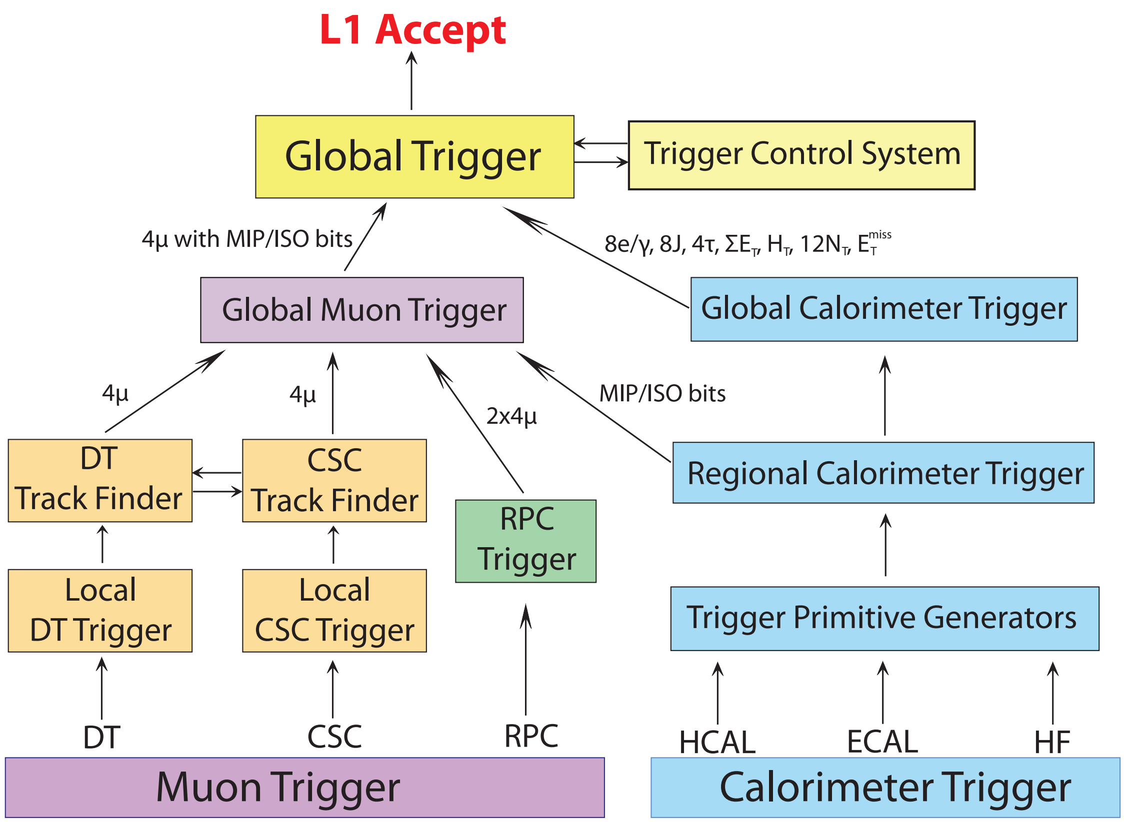

Figure 3.14: Architecture of the L1 trigger system.

The level-1 accept (L1A) signal means that the high resolution data ($\sim$ 1 MByte) is read-out by the DAQ and completely passed on to the HLT for further filtering. The HLT is entirely a software system that preforms complex calculations executed on a multi-processor filter farm. The HLT menu is composed of a set of trigger paths, each path addressing a specific physics object selection. The execution of a path is terminated if the processed event does not meet the conditions imposed by a given filter module.

The HLT paths are seeded by the L1 trigger that accepted the signal. There are complex reconstruction and filter algorithms [22] that are executed at the HLT CPU farm. With the increase of complexity of the algorithms the CPU time required increases, so the termination of the HLT process happens as early as possible, once the requirement of the path is not met. Electron HLT paths used in this analysis are seeded by the single and double electron/photon L1A signal, while muon HLT paths are seeded by the double muon L1A.

An electron L1A from *SingleEG12* means that an ECAL trigger tower energy exceeds the L1 threshold energy of 12 GeV, while the double electron L1 trigger *DoubleEG_12_5* requires two trigger towers, one with the energies more then 5 GeV and another with more then 12 GeV. Electron and photon candidates are not distinguished at the L1 level. An electron HLT uses the electron identification and isolation variables similar to those described in Section 4.3.4 for the online electron isolation and identification. It proceed in following steps:

- ECAL cluster reconstruction within regions corresponding to L1 triggers in the event. Margins are included around the trigger regions to collect bremsstrahlung radiated energy (described in Section 4.3.4).
- ECAL isolation requirement.
- HLCAL energy reconstruction and HCAL isolation requirement.
- Global reconstruction of hits in the pixel detector.
- Reconstruction of the electron track using the Kalman filter.
- Regional track reconstruction using pairs of hits in the pixel layers positioned within a rectangular $\eta - \varphi$ region around the direction of the reconstructed electron.
- Tracker isolation requirement.

Reconstruction, isolation, and identification of the objects used in the analysis are discussed in Chapter 4 and electron and muon HLT paths are given in Tables 4.5 and 4.6 respectively.

The first step of the muon reconstruction in the muon HLT is seeded by the candidates from the muon L1 triggers. In this step reconstructed muon candidates are required to exceed the p_t threshold values specified by the trigger path, after which the muon rate is sufficiently reduced. The next step of reconstruction is done by combining already filtered muons and charged-particle tracks reconstructed in the central tracker. The final filtering is applied on the precisely measured muons reconstructed in both tracking systems. Isolation requirements are an optional step in the muon HLT reconstruction and are not used in this analysis.

Chapter 4

Data Reconstruction and Event Selection

The physics analysis is performed using the four-momentum of the identified particles in the final state of the physics process under study. To obtain this information detector measurements are reconstructed as physics objects like electrons, muons, jets and photons. Reconstruction is based on the combination of the information provided by each subdetector, described in Chapter 3.2. Combining information from different subsystems resolves the ambiguity in the object reconstruction and aids to the correct identification. For example, similarity of the electron and the photon signatures in the ECAL could be disentangled by the presence of associated charged tracks in the tracker system. This chapter explains the reconstruction and identification of the objects used for the analysis. It also provides the details of the final event selection criteria and the efficiencies associated with it.

In addition, a brief overview of the web-based monitoring tools, which are used for constant online and offline monitoring of the CMS detector, is presented. As a member of the CMS WebBased monitoring (WB) team, I have developed and maintained many of these tools.

4.1 Data Quality Monitoring

The data recorded by the CMS detector goes through detailed quality checks before it is used for the physics analysis. The data certification is done by a complex data quality monitoring (DQM) procedure. The data quality is certified by the online and offline DQM. The online stage of DQM runs data-stream parallel to the data acquisition, and provides immediate feedback about the performance of each subdetector during each *CMS Run*. The offline certification is done in several steps: a) for prompt certification of the data quality, a subset of the recorded data is reconstructed using relatively fast algorithms; b) the full dataset is reconstructed using the alignment information; c) the full dataset is reconstructed using full reconstruction algorithms and alignment and is available for the data analysis.

The data certification by DQM takes into consideration the status and performance of an individual subsystem, quality of reconstructed physics objects, and even the correlation between physics objects and higher level objects (such as di-lepton mass peaks). To maximize the amount of data useful for the physics analysis, the data certification granularity is based on small CMS Run periods called lumi-sections, which corresponds to about 23 seconds of data taking.

4.2 WebBased Monitoring

Quality data collection requires very close monitoring of the detector and prompt identification of any problem. The challenging experimental environment and extremely complex detector, trigger, and data acquisition (DAQ) systems impose the necessity of constant and close monitoring tools. The continuous monitoring of the beam conditions, as well as detector hardware and software elements, is the key factor in the high quality data taking. The large geographical scale of the experiment, with over 3000 collaborators from over 40 countries, demands a common framework and remote accessibility of the monitoring tools. *WebBased Monitoring* (WBM) was developed to address the monitoring needs and the security requirements of the experiment, and has become one of the most important tools for the

CMS collaboration. In this section, I will briefly present the WBM tools that I developed with WBM group.

4.2.1 Data Sources

The main idea is to have information aggregated from all the sources that make separate measurements for a particular purpose, into a central monitoring portal providing digested information in a concise manner. Information about the LHC and CMS status, and performance is provided to WBM by specialized hardware via various messaging systems and the Oracle database:

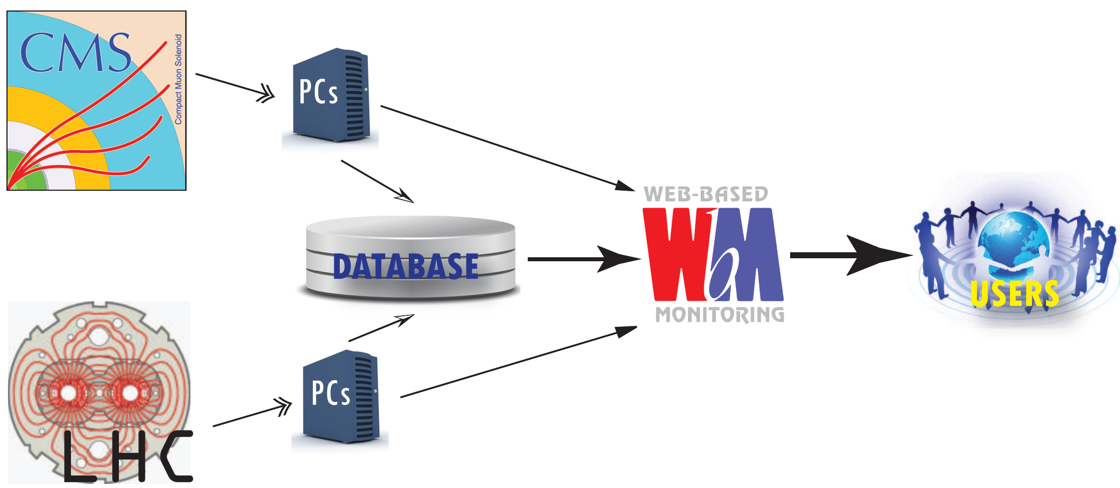

Figure 4.1: A simplified wiev of the WBM system architecture.

The data from various heterogeneous sources are aggregated by WBM, and translated into a user-friendly and convenient form. The fact that WBM provides online and archival monitoring capabilities by obtaining the data from different sources, also makes it a perfect monitoring tool for correct and uninterrupted functioning of the primary data sources. Due to the summarizing nature of the resultant information (tables, plots, etc.), any unexpected behavior of the WBM monitoring tools can promptly indicate and identify a problem in the primary data-provider hardware or software. Figure 4.2 shows the WBM main page with all its services available for the moment.

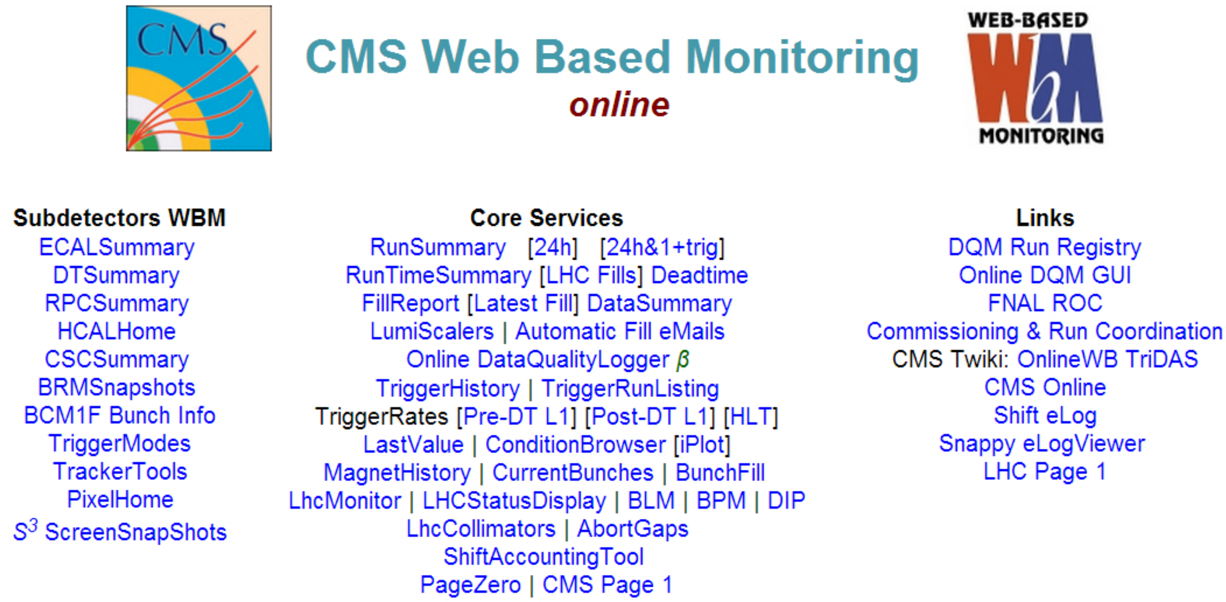

Figure 4.2: WBM main page with all the available services.

4.2.2 Page1 and PageZero

It is very important to have a concise information aggregated at one place and easily accessible for run coordinators and shifttakers. To have all the important information at one glance the following pages were created. *PageZero* (Fig. 4.3) summarizes the status of the CMS and the LHC in various tables, while *CMS Page1* (Fig. 4.4) gives a high level summary, which includes beam conditions, delivered and recorded luminosity, detector high voltage and readout status, trigger rate, and a comment from the shift leader. Pages are presented to the user side as a simple image or an html page, while all queries of the information are done on the server side just once per update period, regardless of the number of accesses from the user side. Both pages are very important for the CMS run coordination, because they give prompt visual feedback of the LHC status and CMS condition by displaying the data acquisition and data control system status for each subdetector. *CMS Page1* also has an outreach aspect to it, since it is a CMS public page, giving the general public access to the details of the CMS experiment in live regime.

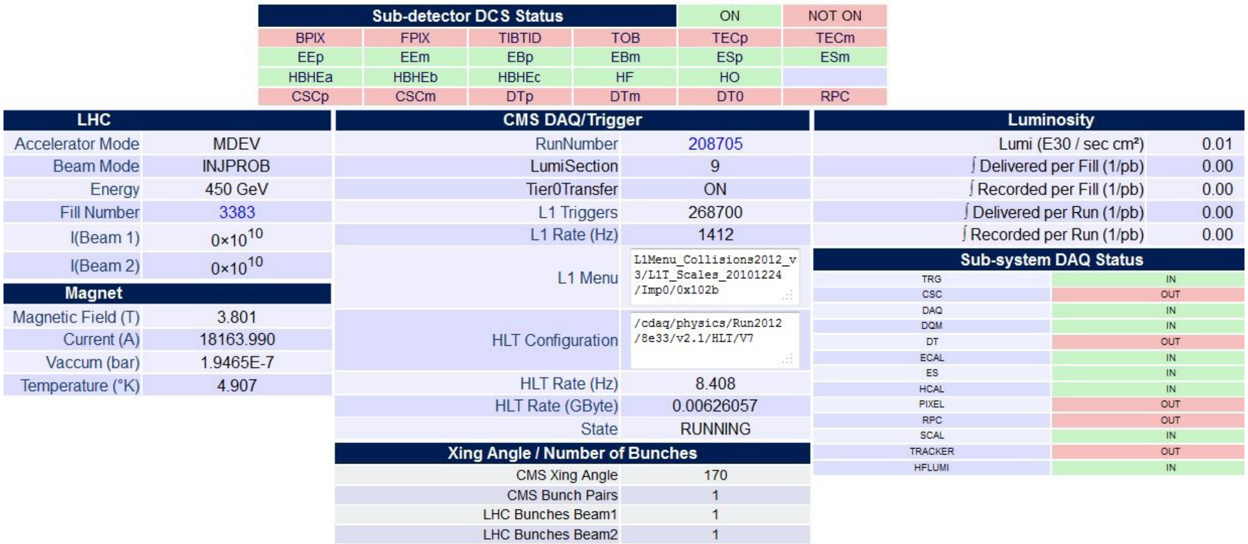

Figure 4.3: CMS PageZero during the stable proton beams.

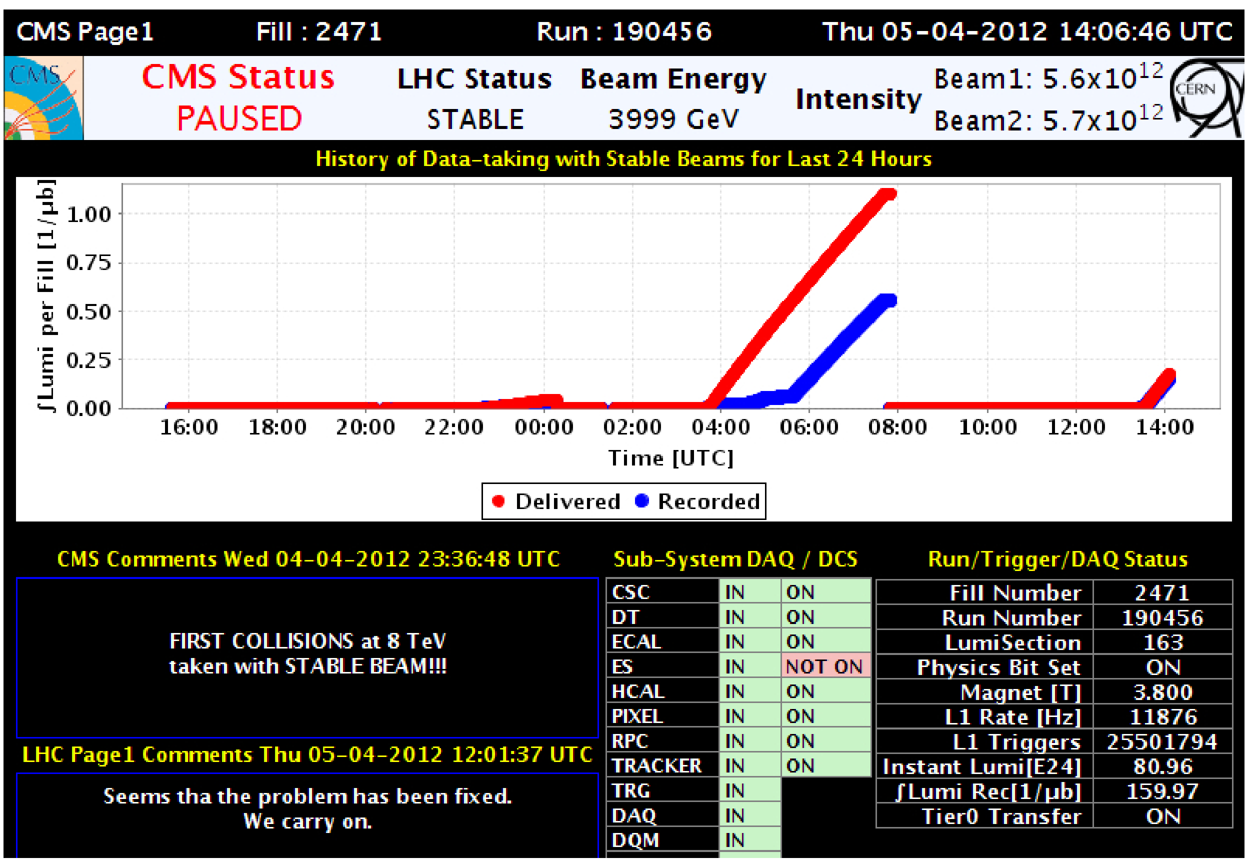

Figure 4.4: CMS Page1 during the LHC fill.

4.2.3 FillReport

FillReport provides users with the online monitoring of the crucial components of the ongoing LHC fill, as well as archival information for all previous fills. At the front summary page (Fig. 4.5), a user can see the list of the latest fills along with the summarized characteristics. The report page of each fill provides plots of important quantities (instantaneous and online measured integrated luminosity, background measurements, vacuum pressure, collimator position, etc.). It also provides the summary table with the numerical values for those quantities. The plots (Fig. 4.6) are generated on the WBM server, using C++ code with ROOT libraries, and provided to the user as '.gif' graphics files, thus eliminating the user side querying the database and optimizing the speed and performance of the web-service.

Fill	Begin Time *YYYY.MM.DD HH:MM*	Duration *HH:MM*	PeakInstLumi $\times 10^{30} cm^{-2} s^{-1}$	DeliveredLumi pb^{-1}	RecordedLumi pb^{-1}	EffByLumi %
2083	2011.09.07 12:36	6:01	573	9.6	8.4	87.5
2085	2011.09.07 21:59	6:06	940	15.1	13.6	89.9
2086	2011.09.08 06:56	10:16	1980	49.6	44.4	89.5
2090	2011.09.09 03:38	1:13	2660	10.6	6.6	62.8
2091	2011.09.09 10:06	2:22	2694	20.6	20.0	96.8
2092	2011.09.09 18:53	6:19	2952	52.3	49.0	93.5
2093	2011.09.10 08:46	0:41	2908	6.8	6.5	96.1
2094	2011.09.10 15:08	0:35	2956	6.0	5.8	96.1
2101	2011.09.12 11:15	3:24	3023	29.9	15.9	53.2
2103	2011.09.12 22:56	8:11	3158	70.0	65.5	93.6
2104	2011.09.13 15:43	3:22	3103	32.6	31.1	95.6
2105	2011.09.14 00:39	16:35	3195	117.4	113.4	96.6
2110	2011.09.15 17:56	6:19	3208	56.7	42.3	74.7
2117	2011.09.16 16:38	8:50	2902	75.2	61.3	81.5
Summary		**80:13**	**3208**	**552.5**	**483.8**	**87.6**

Figure 4.5: Shortened version of the FillReport summary page.

Every quantity on the page is linked to the more detailed information regarding it. Therefore a user can easily drill down to this detailed information using convenient and clear links to WBM tools with more refined information. Due to the importance of information being promptly conveyed to the collaboration, this service is able to send emails to subscribed users with notifications of start and end of the fill and provide the concise summary.

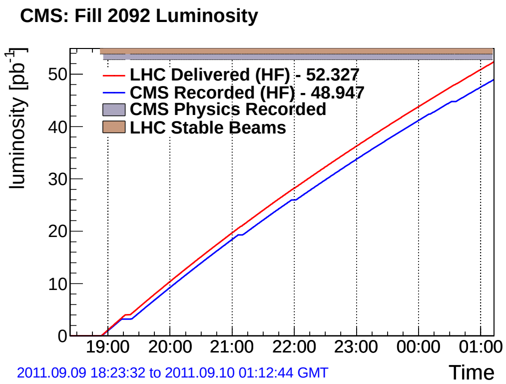

(a) Integrated luminosity

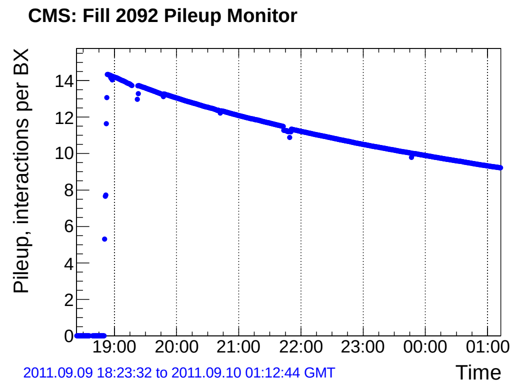

(b) Pileup condition

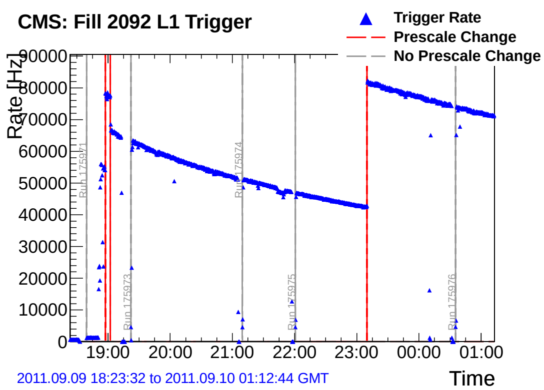

(c) L1 trigger rate

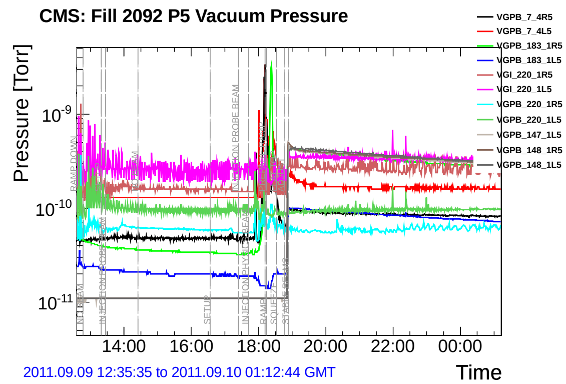

(d) Vacuum level measurements by different vacuum systems

Figure 4.6: Few plots from the FillReport for particular fill, showing values vs. time.

FillReport contains the information regarding all previous fills, which can be useful to analyze the changes or debug the problems. The tool is important not only for online monitoring but also for the data analysis. Besides summarizing the information, it keeps track of the most important values and updates the database with the important record value information, which is used for performance assessment and data analysis.

4.2.4 DataSummary

Efficient data taking on a longer time scale is very important in high energy experiments, which are driven by the amount of quality data. WBM provides a very concise web-service called *DataSummary*, which shows progress of data collection, trend of instantaneous luminosity, and efficiency of data taking on a daily, weekly and yearly basis. The LHC is a complicated machine that can produce head-on collisions of both protons and heavy ions. *DataSummary* provides information for both types of collisions separately.

It also carries both archival and online-monitoring importance. Plots for current day, week, and year are updated frequently to achieve online monitoring capabilities. Like *Fill-Report*, *DataSummary* also tracks the shown quantities to provide the information about record values (highest instantaneous luminosity, most data collected during day, week or month, etc.). Users can drill to the details of every fill and CMS run of the time period shown, using the clear links in the tables. A CMS run is the time period, during which CMS takes data with a well defined configuration.

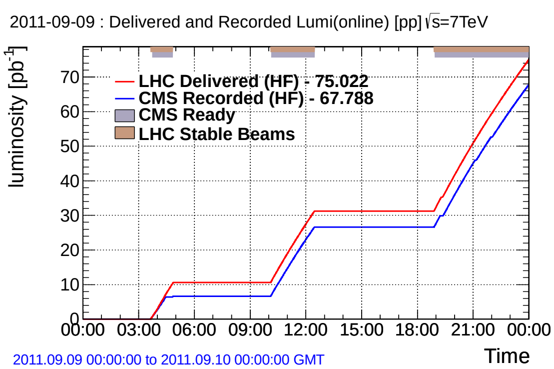

(a) Integrated luminosity per day

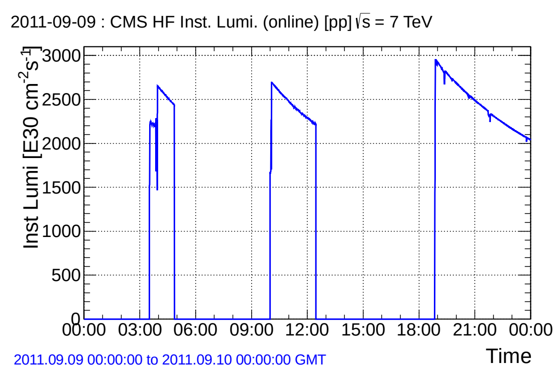

(b) Instantaneous luminosity per day

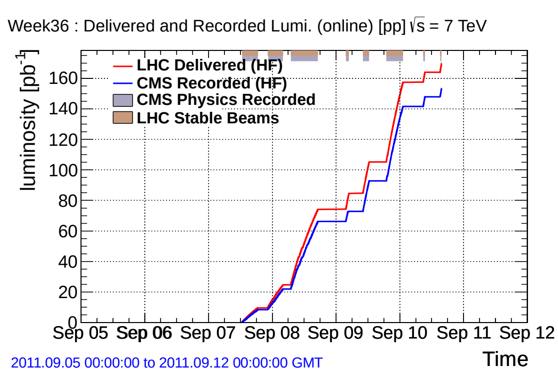

(c) Integrated luminosity per week

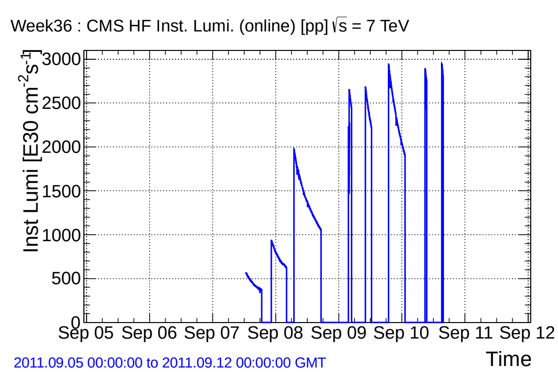

(d) Instantaneous luminosity per week

Figure 4.7: Few plots from the DataSummary for particular day and week.

4.3 Data Reconstruction and Object Identification

Reconstructed physics objects used in this thesis are electrons, muons and photons. The offline reconstruction, isolation and identification of these and related physics objects are described below.

4.3.1 Primary Vertex Reconstruction

The primary vertex (PV) is the point from which the event of interest originates as a result of the colliding beams. The PV reconstruction starts by finding the vertex which is done by clustering the tracks, that are compatible with beam line, by their z coordinate. Next comes vertex fitting, which determines the best estimate of the vertex parameters (position, covariance matrix, track parameters constrained by the vertex position, and their covariances) for a given set of tracks and evaluates the quality of the fit (by χ^2).

There are online and offline PV reconstruction algorithms. The online reconstruction uses track candidates reconstructed from the pixel detector only [23] (from so called hit triplets). It is used for a fast determination of the primary vertex z coordinate for the high level triggers. The offline PV reconstruction, on the other hand uses fully reconstructed tracks. It requires at least 4 tracks, and is required to be within the luminous region, which is defined as the region with transversal distance of 2 cm and longitudinal distances of 24 cm from the origin of the CMS. This requirement ensures that a PV is from a real collision. A large number of inelastic collisions take place at the LHC at every bunch crossing, but usually there is only one vertex containing the event of interest. In this analysis, in order to further suppress background from jets misidentified as electrons due to pileup, we require that primary vertex impact parameter d_0 satisfy $d_0 < 0.02$ cm and longitudinal distance d_z satisfy $d_z < 0.1$ cm.

4.3.2 Track Reconstruction

About 1000 charged particles traverse the CMS tracker at every bunch crossing, making the track reconstruction a very complex challenge. The reconstruction consists of two parts: (1) finding the hits, which are signals in the silicon sensors caused by the passing charged particle, and (2) reconstructing the tracks using these hits. The near hermetic design of the CMS tracker simplifies the task of the efficient search for the hits in the detector. The fact that most of the support structure is concentrated on the layers of the detector and that the magnetic field is almost constant throughout the tracker ensures the faster track reconstruction by allowing to use the relatively simple helical model for the track trajectories.

The digitized information from the CMS tracker detectors, containing the signal and the noise information from the readout channels, is used to build the clusters. During the clustering, the information about the detector alignment is taken into account, and it is done separately for the pixel detector and the silicon tracker. Grouping the neighboring channels into the cluster is based on certain signal to noise ratio requirements. The final cluster is also subjected to this selection criterion. These clusters then are translated into a hit measurements using the cluster parameter estimator (CPE) algorithm. The results of the first step are hits with assigned coordinates and uncertainties, as well as the charges and the profiles of the clusters they originate from. Detailed information about clustering, hit finding and track reconstruction algorithms can be found in [24].

In the second part of the track reconstruction, CMS uses a combinatorial track finder (CFT) as the default algorithm. It consists of three main stages: seed generation, pattern recognition, and final track fit. The seed generation searches for the start points of the tracks, called seeds. The seeds are reconstructed from the hit pairs or hit triplets and the beam line. Seeds are mainly generated from the hits in the pixel detector due to a low occupancy, high efficiency and unambiguous two-dimensional position information.

The pattern recognition stage is based on the Kalman filter method [25]. The filter starts from coarse measurements of the initial seed and successively includes every layer with each iteration. Each layer refines the measurement, thus, after every iteration track parameters are measured with the better precision. In the first step, a dedicated navigation component determines those layers, hits of which are compatible with the initial seed. Then, the trajectory is extrapolated using the equations of motion for the charged particles in the uniform magnetic field. At this point, the geometry and the material budget of the tracker are considered to properly account for the multiple scattering and the energy loss in the material. An additional layer may have several hits that are compatible with the initial seed, so several trajectories are constructed. In order to account for the case when the particle did not produce the hit in the particular layer, one more trajectory, without hit, is constructed. This procedure is repeated for the next layer and so on until the last layer is reached (Fig. 4.8).

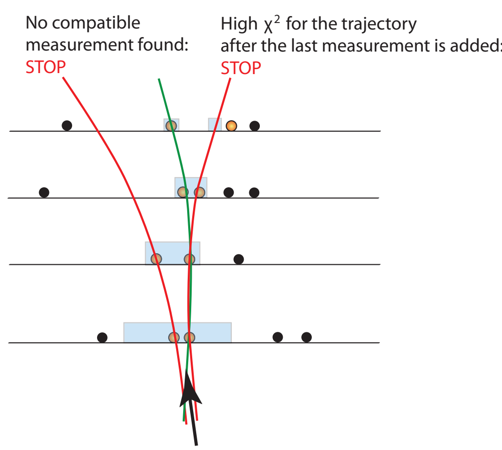

Figure 4.8: Schematic view of the Kalman filter track pattern recognition.

After the track fitting for each layer, the maximum number of trajectories that are propagated to the next level is limited to five, based on the χ^2 and number of hits in the layer, to avoid the exponential growth of the number of track candidates. Thus, the lower quality candidates are dropped. But the full information consists of all the layers, so, in order not to bias the fit, all the valid tracks are refitted starting from the outermost layer and working towards the beam line. The two obtained results are combined with a Kalman smoother to get the final estimate.

4.3.3 Photon Reconstruction

Offline reconstruction of photons and electrons starts from the recovery of the energy deposited by them into the ECAL. In the absence of the magnetic field and any material in front of the calorimeter crystals, approximately 94% (97%) of the energy of a single electron or photon would be contained in the 3×3 (5×5) cluster of the ECAL crystals. Due to the material in front of the ECAL, electrons and positrons undergo bremsstrahlung and photons convert to $e^{+}e^{-}$ pairs. The magnetic field causes the energy reaching the ECAL to be spread in the φ direction. To account for this energy spread, electron and photon objects are reconstructed from the clusters of the ECAL clusters, called superclusters (SCs).

To find SCs, different clustering algorithms are used in the ECAL barrel and ECAL endcaps, due to the difference in their position and geometry. In the barrel hybrid algorithm [26] is used that considers the geometry of the EB crystals in the $\eta - \varphi$ direction to use the knowledge of the shower shape in η direction, making a group of 5×1 crystals, while dynamically searching for the separated (bremsstrahlung) energy in the φ direction. In the endcaps the superclustering algorithm, *Multi5×5*, in addition to the information from the ECAL, also considering the information from the ES. *Multi5×5* first collects the energy from 5×5 clusters and then forms superclusters from such clusters that lie within a road of extension 17° in both directions. The ES clusters are built the similar way at the positions, which are extrapolated from the EE cluster positions. The total endcap basic cluster energy is the sum of the cluster energies in the EE and ES.

After clustering is done, a small energy correction is applied and then SCs are used to reconstruct the photons and electrons, and to seed the electron track reconstruction.

Further high efficiency photon identification and isolation is based on the following criteria required for this analysis:

- A very convenient way to distinguish between the converted and unconverted photons, and further remove the background from the jets, is to use the observable called $R9$, which is defined as the ratio of energy contained in a 3×3 array of crystals centered on the seed crystal of the photon candidate's SC to the total energy of the SC. For unconverted photons, or for photons converted very close to the ECAL, $R9$ values approach unity and smaller values are obtained with increasing distances of the conversion vertex from the ECAL.

- Photon SCs are required not to match a track originating from the interaction point.
- ECAL Isolation (particularly for this analysis so called 'Jurassic' isolation): the sum of the ECAL energy around the photon candidate in an annular region of the inner radius $R = \sqrt{\Delta\eta^2 + \Delta\varphi^2} = 0.06$ and outer radius 0.4, with the exclusion of a rectangular strip of the crystals with $\Delta\eta \times \Delta\varphi = 0.04 \times 0.40$.
- HCAL isolation: the sum of HCAL E_T around the photon candidate in an annular region of inner radius $R = 0.15$ and outer radius 0.4.
- Tracker isolation: the scalar sum of p_T of tracks consistent with the primary vertex in a hollow cone around the photon candidate in an annular region of inner radius $R = 0.04$ and outer radius 0.4. The inner radius is chosen to avoid counting the momentum of the photon conversion tracks in the isolation sum.
- To suppress the photon (electron) background that comes from the hadronic activity, the H/E variable is used, which is defined as the ratio of the total E_t in the ECAL to the total energy in the HCAL in the cone of $R = 0.15$ about the center of the photon (electron) supercluster.
- Another variable to describe the shower shape for the higher purity of the photon or electron identification is $\sigma_{\eta\eta}$, which is given by the following expression:

$$\sigma_{\eta\eta}^2 = \frac{\sum_i \omega_i (i\eta_i - i\eta_{seed})^2}{\sum_i \omega_i} \omega_i = \max\left(0, 4.7 - \ln\frac{E_i}{E_{5\times 5}}\right), \tag{4.1}$$

where E_i and $i\eta_i$ are the energy and η of the i^{th} crystal within the 5×5 ECAL cluster, $E_{5\times5}$ is the energy of the 5×5 crystals around the seed crystal, and $i\eta_{seed}$ is the η of the seed crystal itself.

In these analysis, all the above mentioned variables are used for the photon identification and isolation to achieve high purity and reduce background from jets misidentified as photons. High pile-up condition requires additional care to be taken to account for the additional energy deposition in the ECAL. Following correction to the photon isolation is made:

$$Iso^{new} = Iso^{orig} + \rho_{event} \times A_{eff}, \tag{4.2}$$

where ρ_{event} is the energy density measure for the pile-up activity in the event, which is the median background energy density per unit area (computed using FASTJET package [27]). A_{eff} is the effective area, defined as the ratio of the slope, obtained from the linear fit to $Iso(N_{vtx})$ distribution, to the slope of the linear fit to the $\rho_{event}(N_{vtx})$ distribution, where N_{vtx} is the number of the primary vertices in the event. These corrections stabilize the efficiency with respect to the changing pile-up conditions. Figure 4.9 shows the isolation variable after pile-up correction and its comparison to the data. Table 4.1 shows the A_{eff} used for the pile-up correction of the isolation variables.

Isolation	A_{eff}	
	Barrel	Encdaps
ECAL	0.183	0.090
HCAL	0.062	0.180
Tracker	0.0167	0.032

Table 4.1: A_{eff} used for correcting the isolation variables due to the pile-up activity in the ECAL.

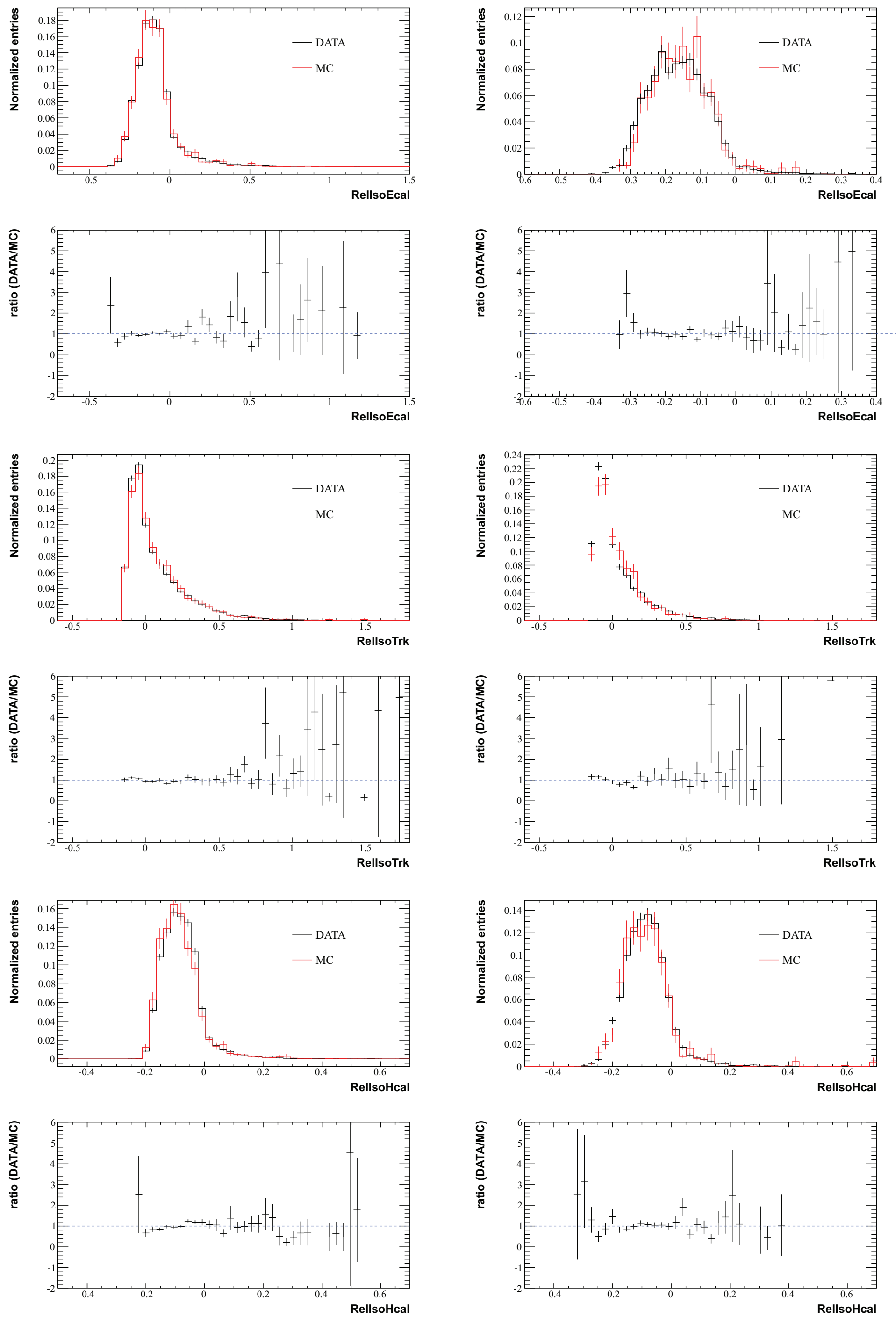

Figure 4.9: Photon isolation variables and Monte Carlo to data comparison after pile-up correction for barrel (left) and end endcaps (right) [1].

To achieve the optimal purity and efficiency the thresholds for the isolation variables are p_t dependent. The cuts used for the isolation variables are optimized for one without the pile-up activity, e.g. for Iso^{orig} in Eq. 4.2. Table 4.2 shows the photon identification requirements applied to the reconstructed photons in this analysis.

Variable	Selection	
Iso^{orig}_{ECAL}	$< 4.2 + 0.006 \times p_t$	
Iso^{orig}_{HCAL}	$< 2.2 + 0.0025 \times p_t$	
$Iso^{orig}_{Tracker}$	$< 2.0 + 0.001 \times p_t$	
H/E	< 0.05	
	Selection in Barrel	Selection in Encdaps
$\sigma_{\eta\eta}$	< 0.011	< 0.03

Table 4.2: Photon identification requirements.

In addition to these cuts, the analysis requires that a photon SC does not have a pixel seed (see electron reconstruction for pixel seed 4.3.4) associated to it to suppress the electron bremsstrahlung photon background.

All the selection criteria are optimized by tuning the selection cut thresholds of a discrete set of variables, using the Monte Carlo simulation, to achieve the maximal signal efficiency for a given, fixed background rejection.

4.3.4 Electron Reconstruction

Electrons leave tracks in the CMS tracker detector, in contrast to photons, which only deposit there energy in the ECAL crystals. Therefore, offline reconstruction of electron, in addition to the reconstruction described in 4.3.3, also includes the association of the track reconstructed in the tracker. The first step of the electron track reconstruction is a pixel seed association. Pixel seed finding uses the electron superclusters, thus considering the electron energy and the associated bremsstrahlung photon energies. The energy weighted position ensures to coincide with the impact point of the electron without the bremsstrahlung. This point is then propagated backward in the magnetic field to be matched with the hits in the innermost layer of the pixel detector for the pixel seed association. The track reconstruction algorithm is then used to reconstruct the track as described in Section 4.3.2 with the pixel seed as the starting point.

Electrons that came from a converted photon are rejected. If an electron is missing hits in the layers before the first hit in the reconstructed track, then it is assumed to be from the converted photon. Also, an electron candidate is considered a result of photon conversion if the distance in the $r - \varphi$ plane between it and its nearest partner track is less than 0.02 and the $\Delta \cot \theta$ between these two objects is less than 0.02. Electron partner tracks for the conversion rejection are searched within a cone of aperture $R < 0.5$ around the electron track. Partner electrons are required to have opposite charges.

As already mentioned in Section 4.3.1, in order to suppress the electron background from the pile-up activity we require $d0 < 0.02$ cm and $dz < 0.1$ cm.

Besides the shower shape variable $\sigma_{\eta\eta}$ described in the photon identification section we also use the $\Delta\varphi_{in}$ and $\Delta\eta_{in}$ variable to describe the transverse shape of the electron shower. The $\Delta\varphi_{in}$ ($\Delta\eta_{in}$) is the absolute difference in the φ (η) direction between the electron supercluster and the associated track as extrapolated to its vertex. For the longitudinal shower shape the H/E parameter is used as described for the photon (4.3.3).

For electron isolation, the variables are calculated as for the photon isolation but within the annular region of outer radius $R = 0.3$. They are aggregated into the combined isolation variable, which is also corrected to account for the pileup energy deposition in the calorimeters:

$$Iso^{combined} = Iso_{ECAL} + Iso_{HCAL} + Iso_{Tracker} + \rho_{event} \times \pi \times \Delta R^2. \tag{4.3}$$

where the efficient area A_{eff} for the pile-up activity is taken to be in radius of 0.3. So, $A_{eff} = \pi \times \Delta R^2 = \pi \times 0.3^2$

Afterwards, the relative isolation (Iso_{rel}) is formed by taking the ratio of the combined isolation to the p_t of the electron supercluster energy. The electron identification requirements are summarized in Table 4.3

	Selection in Barrel	Selection in Encdaps
Iso^{rel}	< 0.053	< 0.042
$\Delta\varphi_{in}$	< 0.039	< 0.028
$\Delta\eta_{in}$	< 0.005	< 0.007
$\sigma_{\eta\eta}$	< 0.01	< 0.031

Table 4.3: Electron identification requirements.

4.3.5 Muon Reconstruction

An efficient muon reconstruction and identification is one of the most important tasks at CMS. Muons that have sufficient momentum not to be trapped by the magnetic field can pass through the entire detector. The ionization of the material due to the charged particles traversing it and energy loss of the particle, depend on the particle energy. In general, there is an energy at which ionization of the material, and therefore the energy loss of the particle, are minimum [28]. For most analyses at the CMS, including this one, muons typically are very close to the minimum ionization region, while the other detected particles are not. For the identification and parameter measurement, muon tracks can be reconstructed both in the silicon tracker and in the muon system. Muons are also expected to deposit a small amount of their energy in the calorimeters, which is called a minimum ionizing particle (MIP) signature and is used for muon identification and isolation purposes.

The muon reconstruction is performed based on the tracks in the tracker for the *tracker muons*, and the signals in muon system for the *stand-alone muons*. The combination of the two gives the best estimate for the muon reconstruction and identification, called a *global muon*, for the muon energies used in this analysis.

The tracker muon reconstruction proceeds inside out starting from the tracker tracks. The tracks are then extrapolated to the muon system and, if the track is compatible with at least one segment in the CSCs or DTs, it is considered the tracker muon.

To reconstruct the stand-alone muons, at least two compatible hits are required in the muon system, at least one of which has to be a segment that allows a muon track parametrization. Once a stand-alone muon is found, the track from the tracker muons and stand-alone muon are extrapolated to a common plane and tracks compatible in momentum, direction, and position are searched for. If such tracks are found, the information is combined and re-fitted to form a global muon track. Based on the fit χ^2 the best global muon track is selected for each stand-alone muon. No compatible tracker track is found to form a global muon in about 1% of all cases. The final fit uses all measurements from both tracker and muon systems for the global muon reconstruction.

In order to minimize the muon fake rate while keeping the efficiency high following identification requirements, that are common for the wide range of the CMS analysis, are used:

- *trackerHits*: Muons are required to have at least eleven hits in the tracker, combining the hits in the pixel detector and silicon tracker. It ensures the accurate p_t measurement and reduces the possibility of a wrong matching during the global muon reconstruction.

- *muonHits*: In order to reduce the fake rate from the hadronic shower leakage (hadronic *punch-through*) into the muon system, a muon track is required to use at least one hit in the muon system for the track fit parametrization.

- *muonStations*: The hadronic punch-through background can further be reduced by requiring at least two hits that come from different muon stations in different layers.

- *pixelHits*: Muons can come from the decay-in-flight processes, which can be efficiently suppressed by requiring at least one hit in the pixel detector.

- $\chi^2/n.d.f.$: To ensure that the muon parameters are well measured and reduce the mismatching of the tracker and stand-alone muons, high quality of fit is required.

The muon is required to satisfy the combined relative isolation requirement as described in Section 4.3.4. The pile-up background is removed using the d_0 and d_z variables. Table 4.4 summarizes all the muon identification requirements.

Variable	Selection
$trackerHits$	> 10
$muonHits$	> 0
$muonStations$	> 1
$pixelHits$	> 0
$\chi^2/n.d.f$	< 10
Iso^{rel}_{comb}	< 0.1
d_0	< 0.01
d_z	< 0.01

Table 4.4: Global muon identification requirements.

4.4 Event Selection

The events that will make their way into this analysis are selected using di-muon and di-electron high level triggers. In addition, to select electron, muon and photon candidates for the final selection of the $Z\gamma$ event candidate, additional offline selection requirements are applied. These aspects are discussed below.

4.4.1 Lepton Selection

Lepton candidates (electrons or muons) have to be reconstructed in the fiducial region of the ECAL for electrons and muon system for the muons. The fiducial region for the ECAL is defined as the regions of the pseudorapidity of the barrel and endcaps with $|\eta| < 1.4442$ and $1.566 < |\eta| < 2.5$ respectively and for the muon system $|\eta| < 2.4$. For electron to be considered within the acceptance of the ECAL, its SC has to be reconstructed within the fiducial region of the ECAL.

Event candidates with muon and electron candidates are preselected using the di-muon and di-electron HLT paths given in Table 4.5 and Table 4.6 respectively. This means that both leptons be matched within a cone of aperture $R < 0.3$ to an object passing the electron or muon trigger being used when the event was collected.

For the detailed performance study of the electron and muon high level triggers please refer to [1].

CMS Run Range	L1 Name	HLT path (all starting with HLT_Ele17)	$\int \mathscr{L} dt$ (pb^{-1})
160431-161176	SingleEG12	CaloIdL_CaloIsoVL_Ele8_CaloIdL_CaloIsoVL_v1	6.3
161217-163261	SingleEG12	CaloIdL_CaloIsoVL_Ele8_CaloIdL_CaloIsoVL_v2	40.7
163270-163869	SingleEG12	CaloIdL_CaloIsoVL_Ele8_CaloIdL_CaloIsoVL_v3	168.5
165088-165633	SingleEG12	CaloIdL_CaloIsoVL_Ele8_CaloIdL_CaloIsoVL_v4	136.4
165970-166967	SingleEG12	CaloIdL_CaloIsoVL_Ele8_CaloIdL_CaloIsoVL_v5	541.5
165970-166967	SingleEG12	CaloIdL_CaloIsoVL_Ele8_CaloIdL_CaloIsoVL_v6	277.3
170826-173198	SingleEG12	CaloIdT_CaloIsoVL_TrkIdVL_TrkIsoVL_Ele8_CaloIdT_CaloIsoVL_TrkIdVL_TrkIsoVL_v6	38.1
170826-173198	DoubleEG_12_5	aloIdT_CaloIsoVL_TrkIdVL_TrkIsoVL_Ele8_CaloIdT_CaloIsoVL_TrkIdVL_TrkIsoVL_v7	777.9
173236-173692	DoubleEG_12_5	aloIdT_CaloIsoVL_TrkIdVL_TrkIsoVL_Ele8_CaloIdT_CaloIsoVL_TrkIdVL_TrkIsoVL_v8	265.3
175832-178380	DoubleEG_12_5	aloIdT_CaloIsoVL_TrkIdVL_TrkIsoVL_Ele8_CaloIdT_CaloIsoVL_TrkIdVL_TrkIsoVL_v8	1829
178420-179889	DoubleEG_12_5	aloIdT_CaloIsoVL_TrkIdVL_TrkIsoVL_Ele8_CaloIdT_CaloIsoVL_TrkIdVL_TrkIsoVL_v9	751.1
179959-180252	DoubleEG_12_5	aloIdT_CaloIsoVL_TrkIdVL_TrkIsoVL_Ele8_CaloIdT_CaloIsoVL_TrkIdVL_TrkIsoVL_v10	128.9

Table 4.5: Summary of the di-electron HLT used for the analysis.

CMS Run Range	L1 Name	HLT path	$\int \mathscr{L} dt$ (pb^{-1})
160431-163869	L1_DoubleMu3	HLT_DoubleMu7_v*	215.5
165088-178380	L1_DoubleMu3	HLT_Mu13_Mu8_v*	3881.8
178420-180252	L1_DoubleMu3	HLT_Mu17_Mu8_v*	880.0

Table 4.6: Summary of the di-muon HLT used for the analysis.

In addition to the HLT, isolation, and identification requirements, leptons are required to have $p_t > 20$ GeV and opposite charge.

4.4.2 Photon Selection

Photon and electron candidates have to be reconstructed from the SC within the fiducial region of the ECAL. The photon transverse momentum has to exceed 30 GeV. The relatively high cut on the transverse momentum further reduces the background from jets misidentified as photons. I also require that photons and leptons are spatially separated by $\Delta R_{\ell,\gamma} = \sqrt{\Delta\eta^2 + \Delta\varphi^2} > 0.7$, where ℓ stands for either e electron or μ muon.

4.4.3 $Z\gamma$ Event Selection

To select the final $Z\gamma$ event candidate I require at least two leptons (muon or electrons) and at least one photon that satisfy all the above mentioned identification and selection requirements. The total invariant mass of the $Z\gamma$ system is required to be withing (50 GeV, 120 GeV) mass range. In addition, to remove the $Z\gamma$ events where photon came as a result of the radiation, called final state radiation event (FSR) a lepton, I apply following requirement $M_{\ell\ell\gamma} + M_{\ell\ell} > 200$ GeV.

Chapter 5

Data and Monte Carlo Simulation

This analysis uses methods that rely completely on data, so called ”data-driven” methods(e.g. for background estimation), and ones that rely on Monte Carlo simulation (e.g. for systematic uncertainties). This chapter describes the data and Monte Carlo samples used in the analysis, and provides the Monte Carlo correction factors that are necessary for proper simulation of the processes under consideration and the detector feedback. The final comparison plots are given at the end of the chapter.

5.1 Data Sample

The data used for the analysis corresponds to the full 2011 data collected during the LHC run 2011A and 2011B of pp collisions at $\sqrt{s} = 7$ TeV. Run A and B correspond to different instantaneous luminosity regimes, therefore different pile-up profiles, and together comprise integrated luminosity of ~ 5 fb^{-1}. The data has been put through the entire chain of the data quality monitoring and certification as discussed in Section 4.1, where every subdetector is required to be certified as *good*.

Information about particular datasets and CMS run ranges used is given in Table 5.1

run range	dataset name	used for
160404 - 163869	/DoubleElectron/Run2011A-May10ReReco-v1/AOD	$Z\gamma \to ee + \gamma$
165071 - 167913	/DoubleElectron/Run2011A-PromptReco-v4/AOD	$Z\gamma \to ee + \gamma$
170249 - 172619	/DoubleElectron/Run2011A-05Aug2011-v1/AOD	$Z\gamma \to ee + \gamma$
172620 - 173692	/DoubleElectron/Run2011A-03Oct2011-v1/AOD	$Z\gamma \to ee + \gamma$
175832 - 180252	/DoubleElectron/Run2011B-PromptReco-v1/AOD	$Z\gamma \to ee + \gamma$
160404 - 163869	/DoubleMu/Run2011A-May10ReReco-v1/AOD	$Z\gamma \to \mu\mu + \gamma$
165088 - 167913	/DoubleMu/Run2011A-PromptReco-v4/AOD	$Z\gamma \to \mu\mu + \gamma$
170249 - 172619	/DoubleMu/Run2011A-05Aug2011-v1/AOD	$Z\gamma \to \mu\mu + \gamma$
172620 - 173692	/DoubleMu/Run2011A-03Oct2011-v1/AOD	$Z\gamma \to \mu\mu + \gamma$
175832 - 180252	/DoubleMu/Run2011B-PromptReco-v1/AOD	$Z\gamma \to \mu\mu + \gamma$

Table 5.1: Information about the datasets used in the analysis

5.2 Monte Carlo Generators

The di-boson analyses aimed at testing the standard model and looking for the effects of a new physics, rely on the comparison of expected and measured kinematic variables. This analysis is using a broad range of the kinematic information by looking at the production and decay angles of the $Z\gamma$ system, therefore the best possible modeling of the Monte Carlo production of the process is crucial. Numerous Monte Carlo generators are available to model the $Z\gamma$ production process at the leading order.

For the acceptance study described in Section 2.5 as well as for the estimation of the next-to-leadig order (NLO) effects, MadGraph5 generator is used. In the first case, it is used to generate $Z\gamma$ samples with and without a contribution of the final state photon radiation events. For the NLO effects contribution, $Z\gamma$ plus up to two jets sample is generated, where additional jets cause $Z\gamma$ system to be boosted in respect with the $q\bar{q}$ center of mass system, thus giving the *effective* NLO effects. The necessity to use effective NLO Monte Carlo simulation is caused by the fact that $Z\gamma$ generators, that would produce the unweighted NLO $Z\gamma$ sample, do not exist [29].

Table 5.2 summarizes the main generator level requirements used for the Monte Carlo generated samples in this analysis.

MadGraph5(LO/NLO)	MadGraph5 (ISR Only)
$p_T^{\ell} > 0$ GeV	" - "
$p_T^{\gamma} > 5$ GeV	" - "
$\lvert\eta_{\gamma}\rvert < 10$	" - "
$\lvert\eta_{\ell}\rvert < 10$	" - "
$\Delta R(\ell, \gamma) > 0.6$	$\Delta R(\ell, \gamma) > 0$
$M_{\ell\bar{\ell}} > 40$ GeV	" - "

Table 5.2: Generator level cuts used in the analysis.

5.3 Detector Simulation

The generated data is run through the complete detector simulation and digitization chain. The detector simulation is done using full detector geometry and particle interaction with the detector material, using GEANT4 integrated into the CMSSW_4_2_0. PYTHIA6 (Tune Z2) is used in the simulation step for simulating the hadronic activity for the underlying events and initial and final state hadronic radiation for the hard scattering process that was generated.

The effects of the detector simulation and differences of the detector acceptance and resolution effects in the simulated and real data are studied. The correction factors are calculated and applied to the simulated data to account for these differences. In order to simulate the proper underlying event activity, the pile-up scenario from the *Summer11/MinBias_TuneZ2_7TeV-pythia6* samples are used.

5.4 Monte Carlo Correction Factors

In order to describe data with all its aspects (pile-up, detector acceptance, selection efficiency, etc.) correctly, additional scale factors (SFs) are applied to the Monte Carlo simulated datasets. *Tag and probe* method is used for the efficiency calculations, and the scale factor is the ratio between those in data and MC. The SFs are calculated as functions of the transverse momentum of the object (leptons or a photon) and the number of the primary vertices, by binning the data sample in this phase-space, for the electron channel. The number of primary vertices give the direct dependence on the pile-up. For the muon channel, where the pile-up dependence is much less pronounced, SFs are calculated as a function of the transverse momentum and the pseudorapidity.

These scale factors correct for the efficiency of the detector simulation and modeling of the hadronization, which is independent of the generated sample, thus independent of the Monte Carlo generator used or whether the process is generated with or without the final state photon radiation. Both Monte Carlo datasets, with and without the FSR contribution, go through the full detector simulation, including the same PYTHIA setup for the simulation of the hadronization of the underlying events and the hard scattering.

5.4.1 Tag and Probe Method

The tag and probe method [30] is based on the very high purity of the $Z \to \ell\bar{\ell}$ ($\ell = \mu, e$) signal. The tag lepton is selected using the stringent lepton selection criteria and acts as a control lepton. The probe lepton is used for the efficiency measurement of the particular selection requirement or trigger. High purity of the tag and probe di-lepton pair is ensured by requiring the di-lepton mass to be close to the nominal mass of the Z boson (e.g. 60 GeV $< M_{\ell\bar{\ell}} <$ 120 GeV). The details of the tag and probe requirements for a particular selection criteria can be found at [1].

As a result, the tag and probe method yields two sets of di-lepton pairs, both have a tag lepton that passed tight selection requirements and a probe lepton, which in one case (tag+pass or TP) passed the selection criteria under study, and fails in the second case (tag+fail or TF). The efficiency of the selection criteria is then defined by the ratio of the number of TP events to the total number of the events (TP+TF). The number of events in each sample is measured using the unbinned maximum likelihood method. The di-lepton invariant mass fit is done using the Fourier convolution of the Breit-Wigner and Crystal Ball functions for the signal, and Mellin convolution of the exponential decay and error functions for the background estimation.

Electron Reconstruction, Identification and HLT Scale Factors

The scale factors for the electron reconstruction, identification and double-electron HLTs used in the analysis are separately calculated and applied to the Monte Carlo data. The efficiencies are calculated sequentially, which means that the identification requirement efficiency is calculated with respect to the reconstruction efficiency, etc. Efficiency calculations are done for the ECAL barrel and edncap fiducial regions separately due to the different reconstruction and identification criteria used in these regions. The scale factors for each case are shown on Figs. 5.1, 5.2 and 5.3.

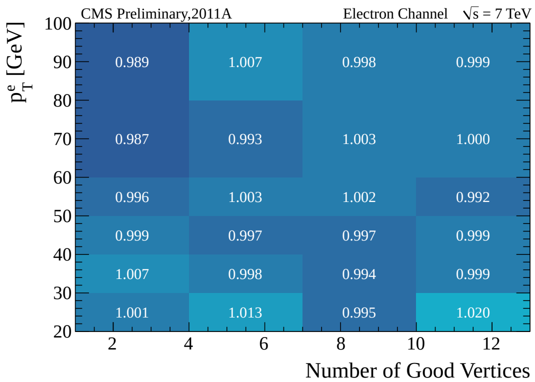

(a) Run A, Barrel

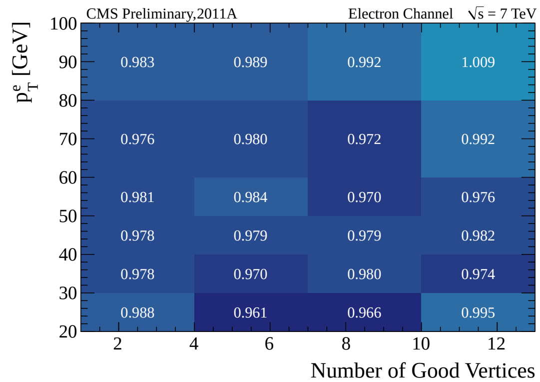

(b) Run A, Encap

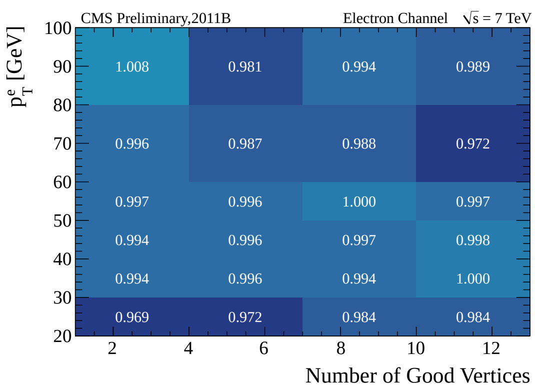

(c) Run B, Barrel

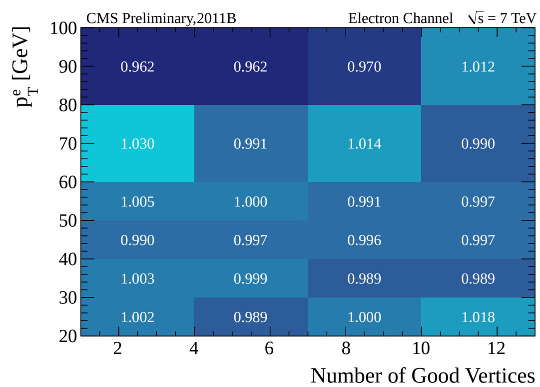

(d) Run B, Endcap

Figure 5.1: Scale factors for electron reconstruction.

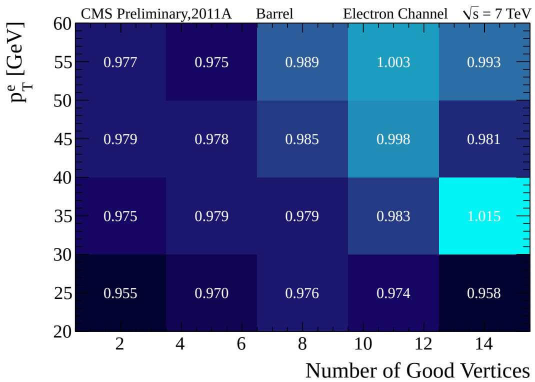

(a) Run A, Barrel

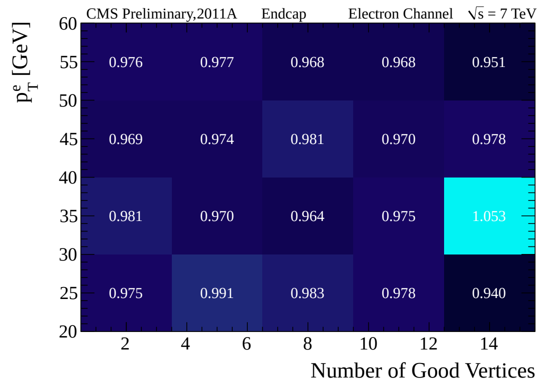

(b) Run A, Encap

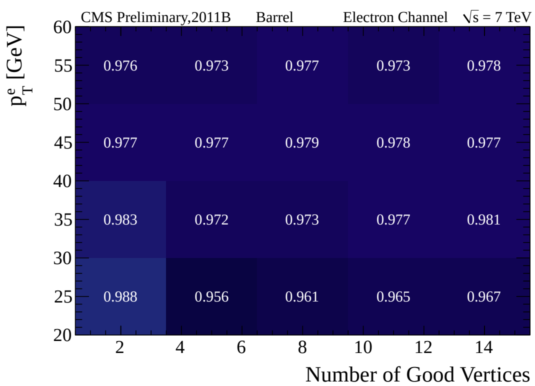

(c) Run B, Barrel

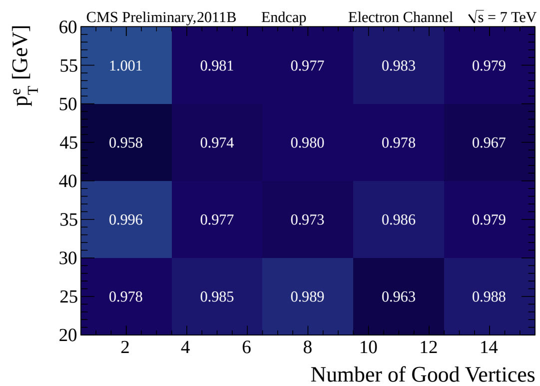

(d) Run B, Endcap

Figure 5.2: Scale factors for electron identification requirements.

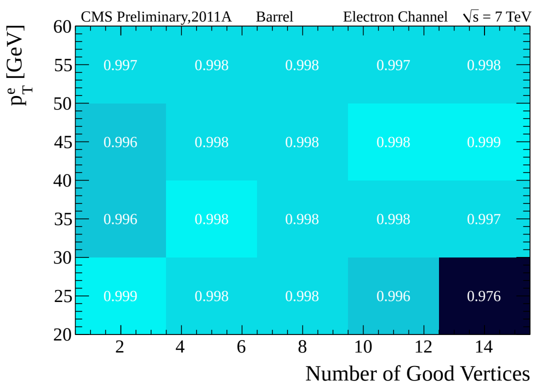

(a) Run A, Barrel

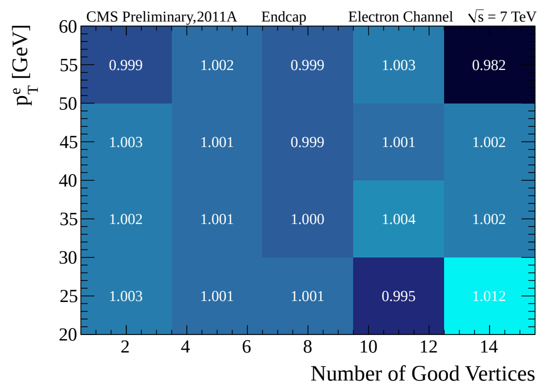

(b) Run A, Encap

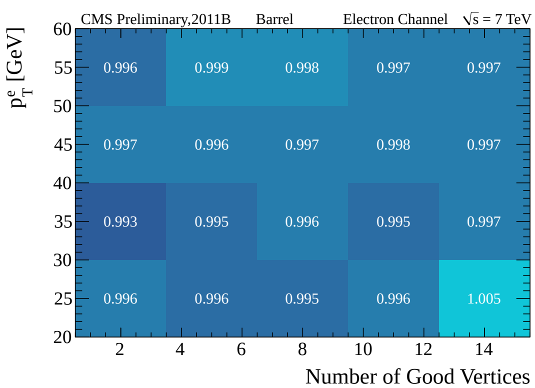

(c) Run B, Barrel

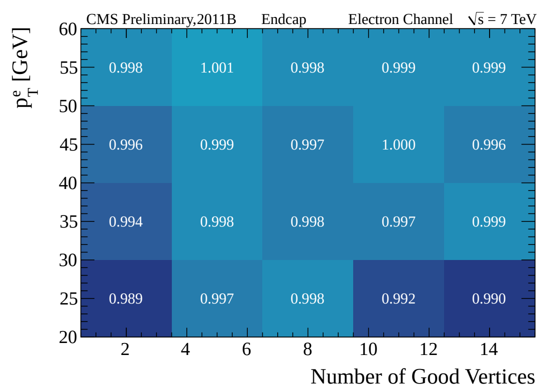

(d) Run B, Endcap

Figure 5.3: Scale factors for di-electron HLT.

Muon Reconstruction, Identification and Trigger Efficiencies

The scale factors for muon reconstruction, identification and di-muon HLTs are factored into one overall muon selection criteria:

$$\epsilon_{tot} = \epsilon_{trk} \times \epsilon_{sa} \times \epsilon_{Id} \times \epsilon_{Iso} \times \epsilon_{HLT}, \tag{5.1}$$

where individual efficiencies correspond to the reconstruction and identification efficiencies that were described before:

- ϵ_{trk} is the efficiency of the muon track reconstruction;
- ϵ_{sa} is the efficiency of stand-alone muon reconstruction;
- ϵ_{Id} is the muon identification requirement efficiency without isolation requirements;
- ϵ_{Iso} is the muon isolation requirement efficiency;
- ϵ_{HLT} is the di-muon HLT efficiency.

The background estimation in this case is done by fitting the di-muon invariant mass distribution with the Landau distribution function. The scale factors for the reconstruction and HLTs are shown on Fig. 5.4.

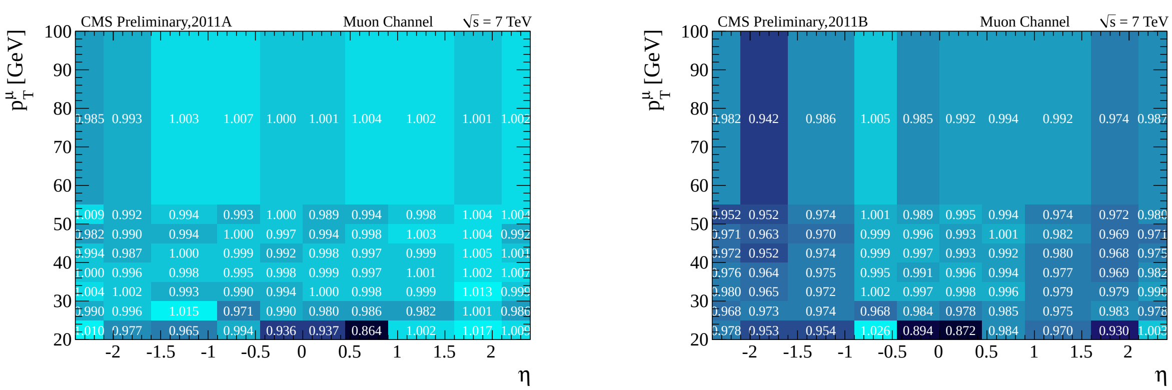

(a) Run A

(b) Run B

Figure 5.4: Scale factors for muon reconstruction, identification and di-muon HLTs.

Photon Reconstruction and Identification Scale Factors

To study the efficiencies of the photons and calculate the photon selection scale factors for the Monte Carlo, tag and probe method was used for the electrons while treating them as photons. This means that photon selection requirements were applied to the probe electron to study its efficiency. The results are shown on Fig. 5.5

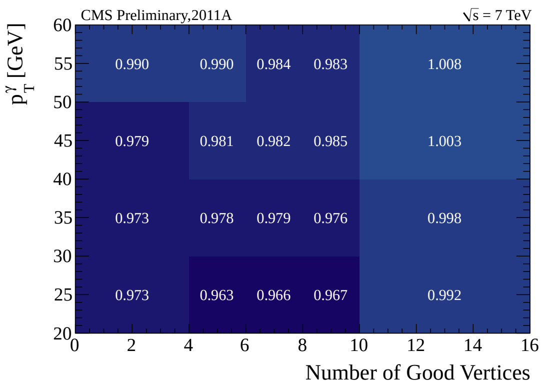

(a) Run A, Barrel

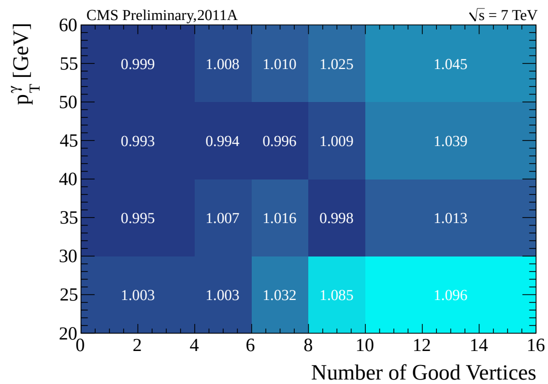

(b) Run A, Encap

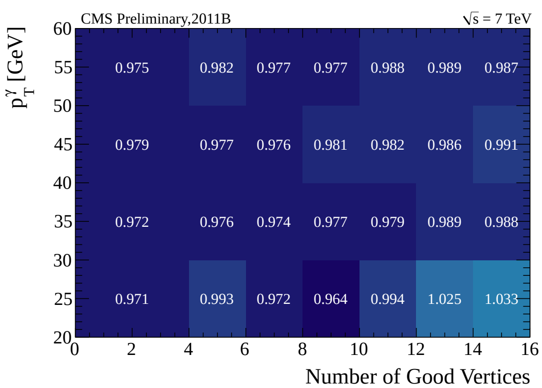

(c) Run B, Barrel

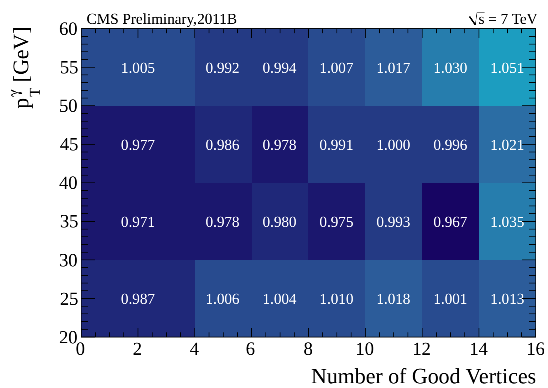

(d) Run B, Endcap

Figure 5.5: Scale factors for photon reconstruction and identification.

5.5 Data and Monte Carlo Comparison

One-dimensional distributions of the angles under study, as well as of the di-lepton invariant mass, after the selection requirements and Monte Carlo correction is given on Figs. 5.6 and

5.7. The plots contain the main background for the $Z\gamma$ production process, which comes from the jets misidentified as photons. Background study is described in Chapter 6.

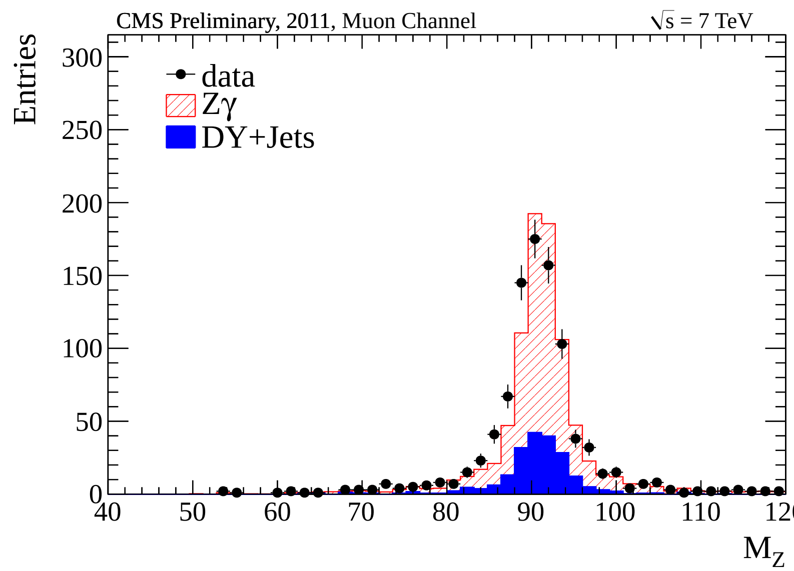

(a) Di-lepton invariant mass

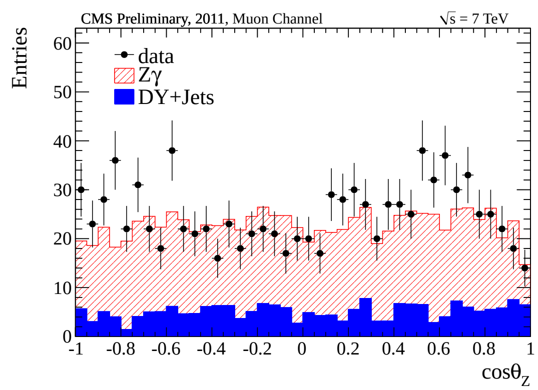

(b) Cosine of the production polar angle

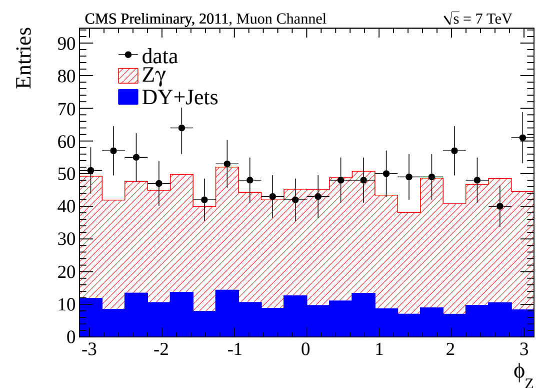

(c) Production azimuthal angle

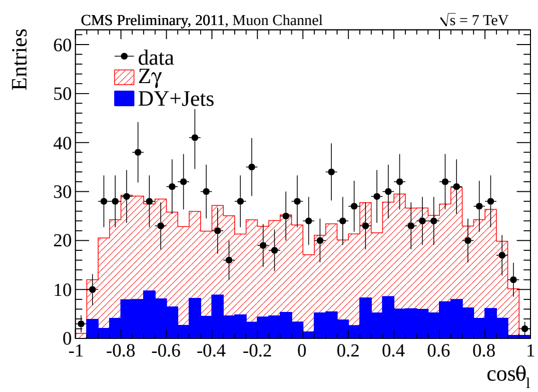

(d) Cosine of the decay polar angle

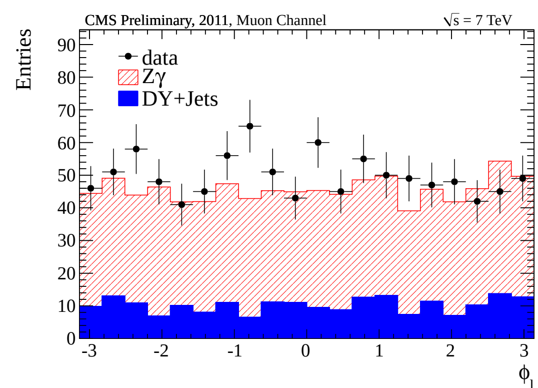

(e) Decay azimuthal angle

Figure 5.6: Data and Monte Carlo comparison plots for muon channel.

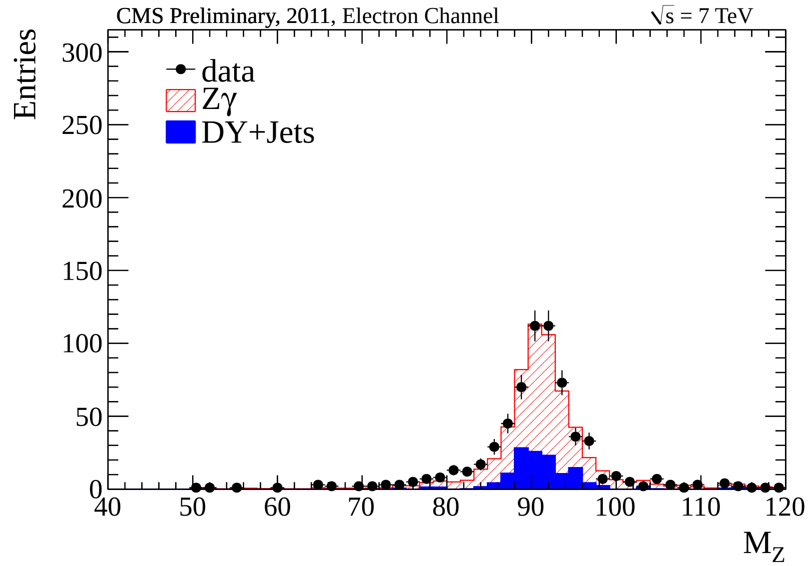

(a) Di-lepton invariant mass

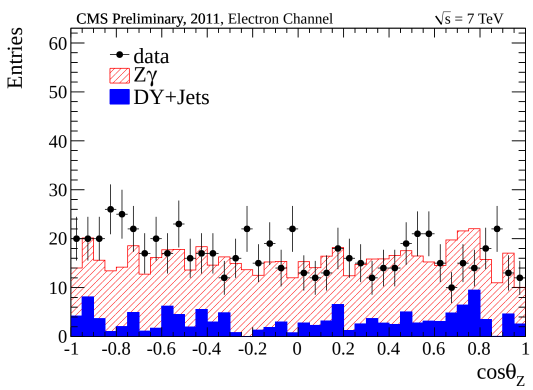

(b) Cosine of the production polar angle

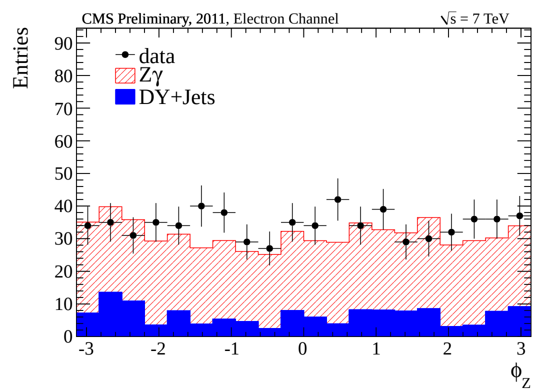

(c) Production azimuthal angle

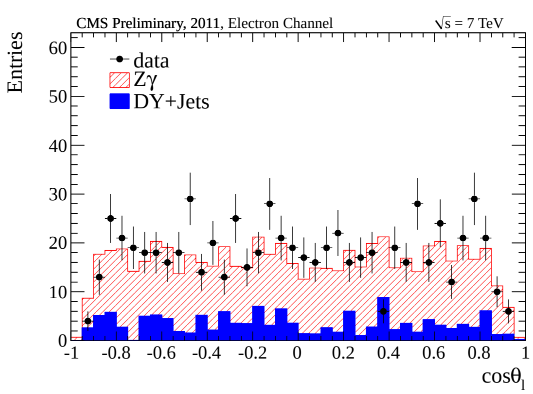

(d) Cosine of the decay polar angle

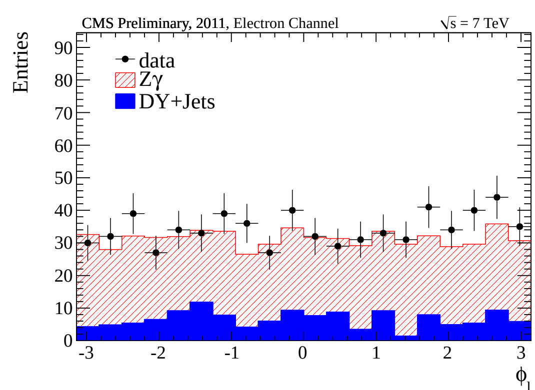

(e) Decay azimuthal angle

Figure 5.7: Data and Monte Carlo comparison plots for electron channel.

Chapter 6

Background Study

The background for the $Z\gamma$ production process is largely dominated by the photon background, which comes from the hadronic jets giving a photon signal. The rate of jets being misidentified as photons is measured using the data with the *template* method, which is described in this chapter. The likelihood function that is used for the measurement of the helicity amplitudes in this analysis does not consider the background contribution, so parameters are measured both with and without the background and effects are used as a systematic error. The contribution from other backgrounds have been measured using Monte Carlo simulation and yielded just a handful of events, thus is completely neglected in this analysis.

The data-driven template method of background estimation is used to estimate the number of the expected background events. Actual distribution of the background sample is obtained from the Monte Carlo sample of the Drell-Yan $q+\bar{q}\rightarrow\ell+\bar{\ell}$ plus jets production. The sample is then scaled to the number of the events that has been estimated from the data.

6.1 Template Method

The template method exploits the discriminating power of the electromagnetic shower shape variable $\sigma_{\eta\eta}$ (Eq. 4.1). The $\sigma_{\eta\eta}$ distribution for the prompt photons is symmetric about the sharp peak, whereas the photons that come from the hadronic activity produce asymmetric distribution with a larger tail towards the larger $\sigma_{\eta\eta}$ values. This is the reason $\sigma_{\eta\eta}$ is required to be less than 0.01 in barrel and 0.03 in the endcap region in order to remove the $\sigma_{\eta\eta}$ tail, which is dominated by the background photons, as discussed in Section 4.3.3. The $\sigma_{\eta\eta}$ distributions for the signal $S(\sigma_{\eta\eta})$ and for the background $B(\sigma_{\eta\eta})$ are taken as templates for the final fit of the data to calculate the jet misidentification rate.

The photon $\sigma_{\eta\eta}$ distribution template for the signal is obtained using the simulated $W\gamma$ events. The correctness of the simulation is checked by comparing the $\sigma_{\eta\eta}$ distributions for electrons in the simulation and in the data. This comparison is based on the purity of the electrons from the $Z \to e^+e^-$ decay. The electron candidates have to satisfy the identification and selection criteria described in Chapter 4, except the $\sigma_{\eta\eta}$ requirement is not enforced only for one of the electrons - tag electron, and the distribution is obtained for the other electron. The purity of these electrons is 99%. Little shift of the distribution was observed (Fig. 6.1) for the electrons and the distribution for the photon has been corrected accordingly.

The background template was obtained completely from the data. Photons for the background sample are required to pass all the photon identification and selection requirements except the $\sigma_{\eta\eta}$ cut and fail the track isolation requirement. Failing isolation requirement ensures that only negligible amount of photons contribute to the obtained $\sigma_{\eta\eta}$ distribution. Candidates selected this way have the photon-like features and with high purity do not originate from prompt photons. Using the Monte Carlo simulation, the correlation between $\sigma_{\eta\eta}$ and track isolation variable was checked. It was shown that the distribution does not depend on the isolation requirement, therefore, the template obtained from the region with failed isolation cut can be used for the photons that pass the isolation requirement as well.

After obtaining the distribution templates the data was fitted by the following function:

$$N_S S(\sigma_{\eta\eta}) + N_B B(\sigma_{\eta\eta}) = N\left[\frac{N_S}{N} S(\sigma_{\eta\eta}) + \left(1 - \frac{N_S}{N}\right) B(\sigma_{\eta\eta})\right]. \tag{6.1}$$

where N, N_S and N_B are total number of events number of events, number of signal and

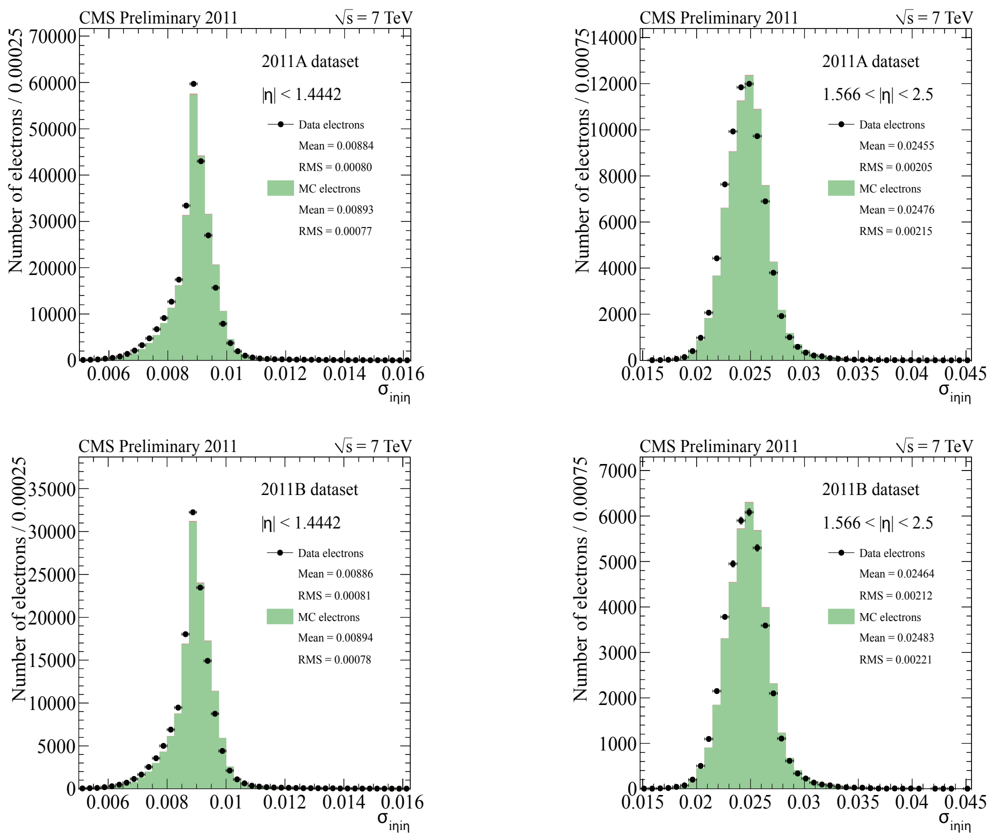

Figure 6.1: Comparison of the simulated $\sigma_{\eta\eta}$ distribution for the electrons to the distribution obtained from the data, in barrel (left) and endcap (right) regions for 2011A and 2011B datasets separately.

background events in the data accordingly, in each p_T^γ bin.

The fit was performed in p_T^γ bins by minimizing the extended maximum likelihood function (fit is shown on Fig. 6.2). Results of the fit are shown in Table 6.1. Figure 6.3 shows the p_T^γ distribution of the data and corresponding background yield.

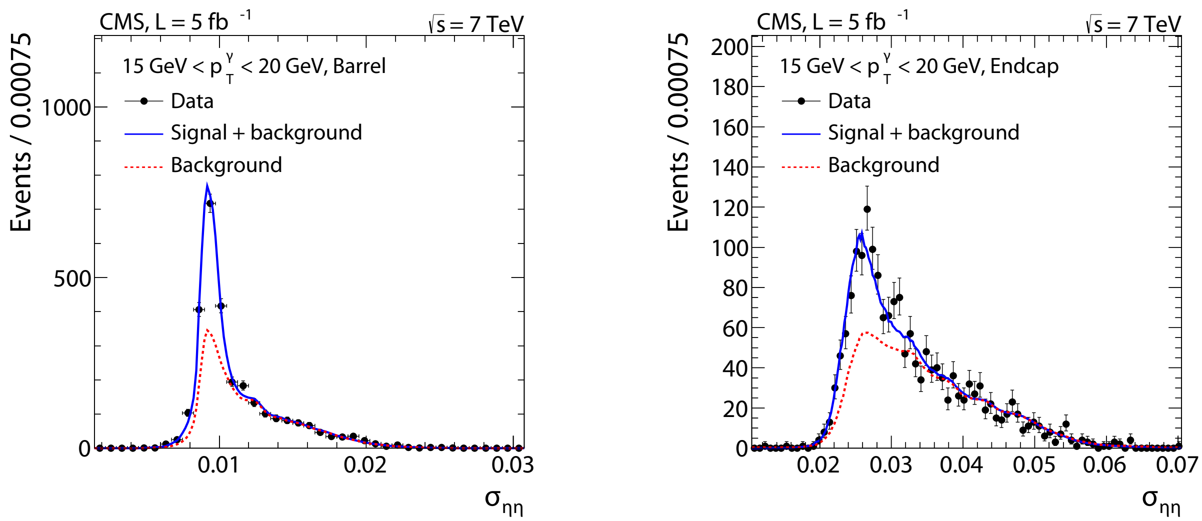

Figure 6.2: Fit to the $\sigma_{\eta\eta}$ distribution for the photons with 15 GeV $< p_T^\gamma <$ 20 GeV in the barrel (left) and endcap (right) regions.

p_T^γ GeV	Background Yield	
	$Z\gamma \to ee\gamma$	$Z\gamma \to \mu\mu\gamma$
30-35	32.4	50.7
35-40	38.6	37.7
40-60	36.3	64
60-90	17.3	25.1
90-120	0	13.7
120-500	5.2	7.5

Table 6.1: Background yields from jet misidentification for electron and muon channels in different p_T^γ bins.

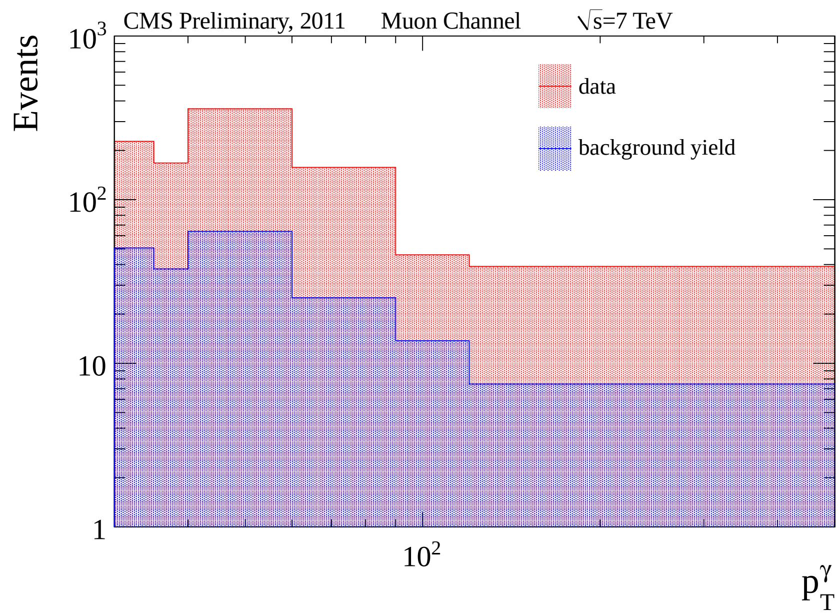

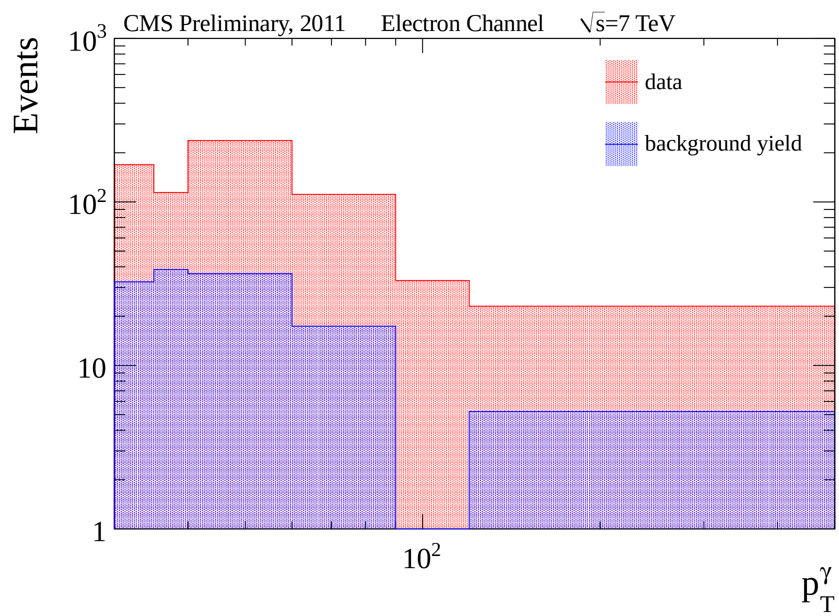

Figure 6.3: Photon transverse momentum distribution of the data and corresponding background yield in muon and electron channels.

Chapter 7

Results

This chapter presents the results of the measurement of the helicity amplitudes described in the analysis as well as the measurement of the systematic uncertainties for the methods used for building the model.

7.1 Helicity Amplitudes

As mentioned in Chapter 2 the distribution function fitted to the data has to be truncated in terms of the total angular momentum $J_{Z\gamma}$, which is taken to be 0, 1 and 2 in this case. With more data higher total angular momentum helicity states can be probed. The linearly independent helicity amplitudes, from the point of view of the *effective* parity conservation (Eq. 2.12) are given in Table 7.1 arranged according to different properties.

There are total of 16 helicity amplitudes describing the $q\bar{q} \to Z\gamma$ production process with $q\bar{q}$ total angular momentum 0, 1 and 2, and two helicty amplitudes describing the $Z \to \ell\bar{\ell}$ decay process. These quantum mechanical amplitudes are complex numbers, thus in principle there are twice as many free parameters (real and imaginary parts of the amplitude, or phase and amplitude). However, the amount of data used in this analysis doesn't allow to measure the phase of the helicity amplitudes and therefore they are set to zero and only the measurement of the real parts (amplitudes) is performed.

Also, it should be noted that the normalization coefficient that is omitted in the distribution function affects the $A_{\lambda_{\ell\ell}}$ amplitudes, so the measurement of the absolute value of

$A_{\lambda_{\ell\ell}}$	$T^J_{\lambda_{qq}\lambda_Z\lambda_\gamma}$		
	$J=0$	$J=1$	$J=2$
A_{-1}	$T^0_{0,-1,-1}$	$T^1_{-1,-1,-1}$	$T^2_{-1,-1,-1}$
A_1		$T^1_{-1,0,-1}$	$T^2_{-1,0,-1}$
		$T^1_{0,-1,-1}$	$T^2_{-1,1,-1}$
		$T^1_{0,0,-1}$	$T^2_{0,-1,-1}$
		$T^1_{1,-1,-1}$	$T^2_{0,0,-1}$
		$T^1_{1,0,-1}$	$T^2_{0,1,-1}$
			$T^2_{1,-1,-1}$
			$T^2_{1,0,-1}$
			$T^2_{1,1,-1}$

Table 7.1: Helicity amplitudes measured in this analysis.

these parameters is not very meaningful. The meaningful parameter to measure would be:

$$k_A = \frac{A_{-1}}{A_1}. \tag{7.1}$$

The $A_{\lambda_{\ell\ell}}$ parameters are responsible for the asymmetry in the $\cos\theta_\ell$ distribution due to the parity violating $Z \to \ell\ell$ process. Hence, the deviation of the k_A parameter from unity would be related to the above mentioned asymmetry.

To demonstrate the goodness of likelihood fit, the χ^2 between the data and the fit is calculated for the distribution of each angle separately. If the measured parameters are plugged into the distribution function, it will describe the distribution due to the underlying physics that governs the process, or in terms of Monte Carlo, it will describe the generated sample. But in order to actually check the performance of the fit it has to be compared to the data, which of course already reflects the detector, identification, and reconstruction acceptances and efficiencies. So, the function to be compared to the data is:

$$fitFunction = \frac{d\sigma}{d\Omega_Z \Omega_\ell} \times \epsilon(\Omega_Z, \Omega_\ell). \tag{7.2}$$

To get the *fitFunction* the RECO sample of the pure signal is reweighted using the weights from the parametrization described in Section 2.5. This parametrization will yield the distribution for the $\epsilon(\Omega_Z, \Omega_\ell)$. So, if the distribution function is reweighted with those

ϵ weights the resultant distribution will correspond to the *fitFunction*. The χ^2 is calculated for this function and the data for which the amplitudes were measured.

Figures 7.1 and 7.2 show the performance of the fit with the corresponding χ^2 for the data and for the LO $Z\gamma$ Monte Carlo production.

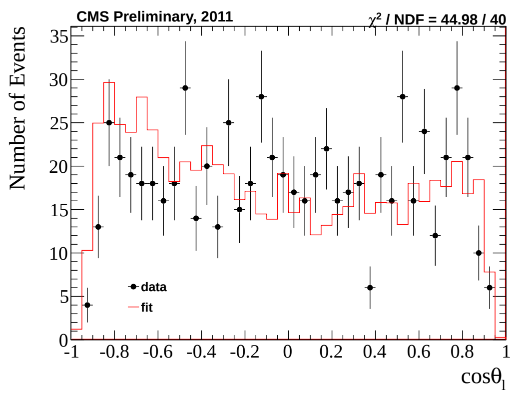

(a) Polar angle distribution for the decay process

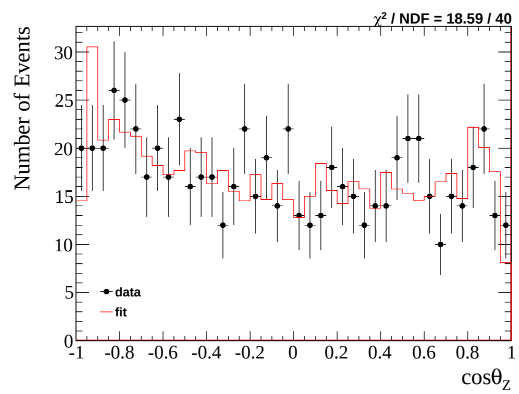

(b) Polar angle distribution for the production process

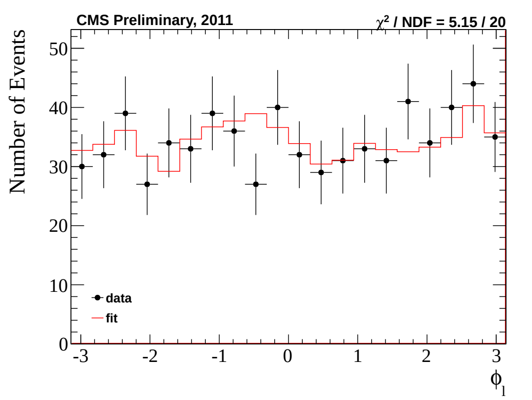

(c) Azimuthal angle distribution for the decay process

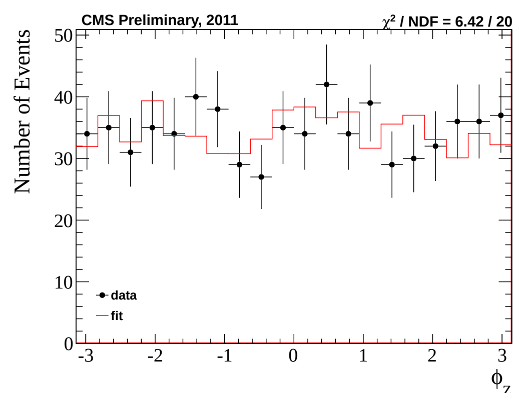

(d) Azimuthal angle distribution for the production process

Figure 7.1: Angular distributions for the data overlaid with the likelihood fit result projection to each angular dimension for electron channel.

These Monte Carlo results are then compared to the measurements on the other datasets for the systematic uncertainty studies. Tables 7.2, 7.4, 7.3, and 7.5 show the results of the measurements in electron and muon channels.

The measurements show that $T^0_{0,-1,-1}$ amplitude is roughly an order of magnitude higher

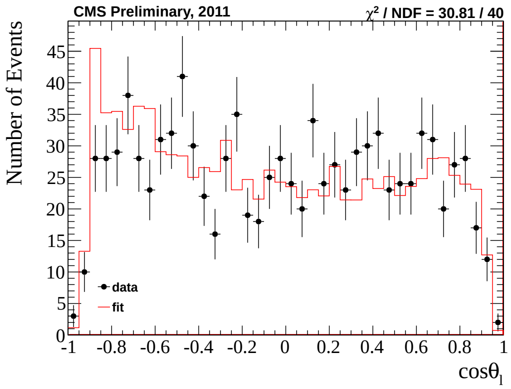

(a) Polar angle distribution for the decay process

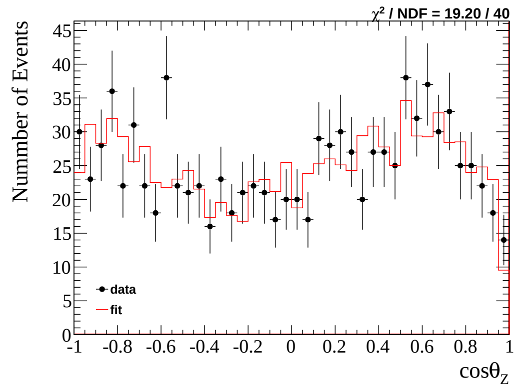

(b) Polar angle distribution for the production process

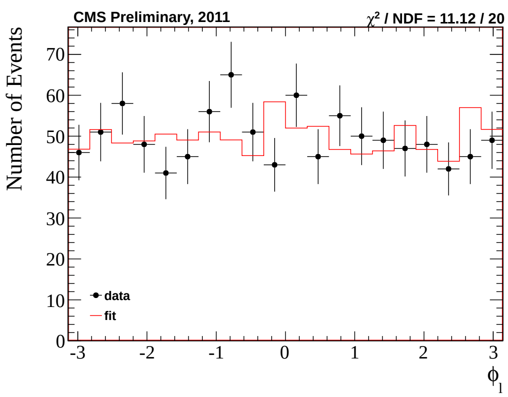

(c) Azimuthal angle distribution for the decay process

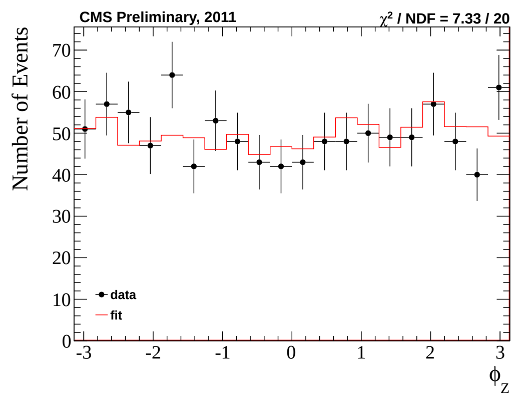

(d) Azimuthal angle distribution for the production process

Figure 7.2: Angular distributions for the data overlaid with the likelihood fit result projection to each angular dimension for muon channel.

than others. This parameter is the only contribution from the $J_{Z\gamma} = 0$ state of the production process. Therefore, it shows that the contribution from the $J_{Z\gamma} = 0$ is dominant in this process.

The amplitudes measured for the muon channel are very consistent with the standard model $Z\gamma$ leading order prediction, whereas the electron channel shows some discrepancy. However the same behavior is observed during the systematic uncertainty studies shown in next sections.

$Z \to ee$ channel	k_A	$T^J_{\lambda_{q\bar{q}}\lambda_Z\lambda_\gamma}$						
		$T^0_{0,-1,-1}$	$T^1_{-1,-1,-1}$	$T^1_{-1,0,-1}$	$T^1_{0,0,-1}$	$T^1_{0,-1,-1}$	$T^1_{1,-1,-1}$	$T^1_{1,0,-1}$
signal	1.02 $\pm$0.3	-6.17 $\pm$1.5	0.06 $\pm$0.2	-0.36 $\pm$0.3	0.82 $\pm$0.4	0.86 $\pm$0.5	2.76 $\pm$0.9	2.03 $\pm$0.4
data	1.00 $\pm$0.5	-7.84 $\pm$3.5	-1.08 $\pm$1.0	-2.57 $\pm$1.5	3.23 $\pm$1.6	-2.00 $\pm$1.1	-0.36 $\pm$0.9	2.23 $\pm$1.1
χ^2	0.0	0.2	1.2	2.2	2.1	5.6	6.4	0.0

Table 7.2: Data and Monte Carlo measurement results for Z decay and $Z\gamma$ production helicity amplitudes for $J_{Z\gamma} = 0, 1$. Electron channel.

$Z \to \mu\mu$ channel	k_A	$T^J_{\lambda_{q\bar{q}}\lambda_Z\lambda_\gamma}$						
		$T^0_{0,-1,-1}$	$T^1_{-1,-1,-1}$	$T^1_{-1,0,-1}$	$T^1_{0,0,-1}$	$T^1_{0,-1,-1}$	$T^1_{1,-1,-1}$	$T^1_{1,0,-1}$
signal	0.95 $\pm$0.3	-11.05 $\pm$3.7	0.36 $\pm$0.4	-0.06 $\pm$0.6	1.82 $\pm$0.6	2.10 $\pm$0.7	4.78 $\pm$1.1	1.83 $\pm$1.1
data	1.06 $\pm$0.5	-11.43 $\pm$4.9	-0.24 $\pm$0.9	-0.64 $\pm$1.1	2.38 $\pm$1.3	2.73 $\pm$1.4	5.42 $\pm$2.2	4.16 $\pm$1.8
χ^2	0.0	0.0	0.4	0.2	0.2	0.2	0.1	1.3

Table 7.3: Data and Monte Carlo measurement results for Z decay and $Z\gamma$ production helicity amplitudes for $J_{Z\gamma} = 0, 1$. Muon channel.

7.2 Systematic uncertainties for the resolution study

In this analysis I use event-by-event (unbinned) extended likelihood for parameter measurement, which assumes that the resolution of the used variables is very high. One way to demonstrate the high resolution of the measured variable would be to show the correlation between its true (or generated (GEN)) value with its fully reconstructed (RECO) value. This would show how well the variable is measured by the detector and reconstructed by the offline reconstruction algorithms. Plots on Fig. 7.3 show such correlation.

To measure the systematic uncertainty that arises from this assumption, I take the Monte Carlo dataset that has gone through full detector simulation and reconstruction procedures, and measure the helicity amplitudes for the event candidates selected from this dataset. Then, the Monte Carlo generated values (also called Monte Carlo truth information) for the event candidates selected in the fully reconstructed dataset are taken and helicity amplitudes

$Z \to ee$ channel	$T^J_{\lambda_{q\bar{q}}\lambda_Z\lambda_\gamma}$								
	$T^2_{-1,-1,-1}$	$T^2_{-1,0,-1}$	$T^2_{-1,1,-1}$	$T^2_{0,-1,-1}$	$T^2_{0,0,-1}$	$T^2_{0,1,-1}$	$T^2_{1,-1,-1}$	$T^2_{1,0,-1}$	$T^2_{1,1,-1}$
signal	-0.33 ± 0.2	-0.17 ± 0.2	-0.06 ± 0.2	-0.09 ± 0.2	0.83 ± 0.3	-1.02 ± 0.7	1.00 ± 0.4	0.93 ± 0.3	-1.03 ± 0.8
data	-0.60 ± 0.8	0.23 ± 0.7	4.06 ± 1.7	1.91 ± 1.0	-0.61 ± 0.8	1.36 ± 1.4	1.95 ± 1.1	-0.66 ± 0.5	1.44 ± 1.1
χ^2	0.1	0.3	5.6	4.2	2.8	2.3	0.8	8.0	3.2

Table 7.4: Data and Monte Carlo measurement results for $Z\gamma$ production helicity amplitudes for $J_{Z\gamma} = 2$. Electron channel.

$Z \to \mu\mu$ channel	$T^J_{\lambda_{q\bar{q}}\lambda_Z\lambda_\gamma}$								
	$T^2_{-1,-1,-1}$	$T^2_{-1,0,-1}$	$T^2_{-1,1,-1}$	$T^2_{0,-1,-1}$	$T^2_{0,0,-1}$	$T^2_{0,1,-1}$	$T^2_{1,-1,-1}$	$T^2_{1,0,-1}$	$T^2_{1,1,-1}$
signal	0.36 ± 0.3	0.11 ± 0.6	-0.44 ± 0.5	-0.11 ± 0.6	1.38 ± 0.5	-2.67 ± 1.8	2.38 ± 0.7	0.81 ± 0.8	-3.84 ± 1.3
data	0.42 ± 0.7	0.23 ± 0.7	0.68 ± 1.0	-0.87 ± 0.8	2.57 ± 1.1	-4.84 ± 2.3	3.40 ± 1.5	0.35 ± 1.1	-3.99 ± 2.1
χ^2	0.0	0.0	1.0	0.6	0.9	0.5	0.4	0.1	0.0

Table 7.5: Data and Monte Carlo measurement results for $Z\gamma$ production helicity amplitudes for $J_{Z\gamma} = 2$. Muon channel.

are measured for the dataset they comprise. The total integrated luminosity for the Monte Carlo datasets is normalized to the total integrated luminosity of the data using the number of events:

$$\mathcal{L}_{\mathcal{MC}} = \frac{N_{MC}}{N_{data}}\mathcal{L}_{data}. \tag{7.3}$$

Individual χ^2 between GEN and RECO values are applied as a systematic uncertainty for the corresponding parameter.

It is important to note that the helicity amplitudes in the distribution function are correlated in a very intricate way and if we go to higher total angular momenta the correlation gets even more complicated, so in order to get rid of the error due to the correlation of the parameters, each parameter is minimized individually while other were fixed, for the systematic uncertainty studies. This way every parameter gives a measure of how much the curvature due to this parameter deviates from its leading order value, thus giving the

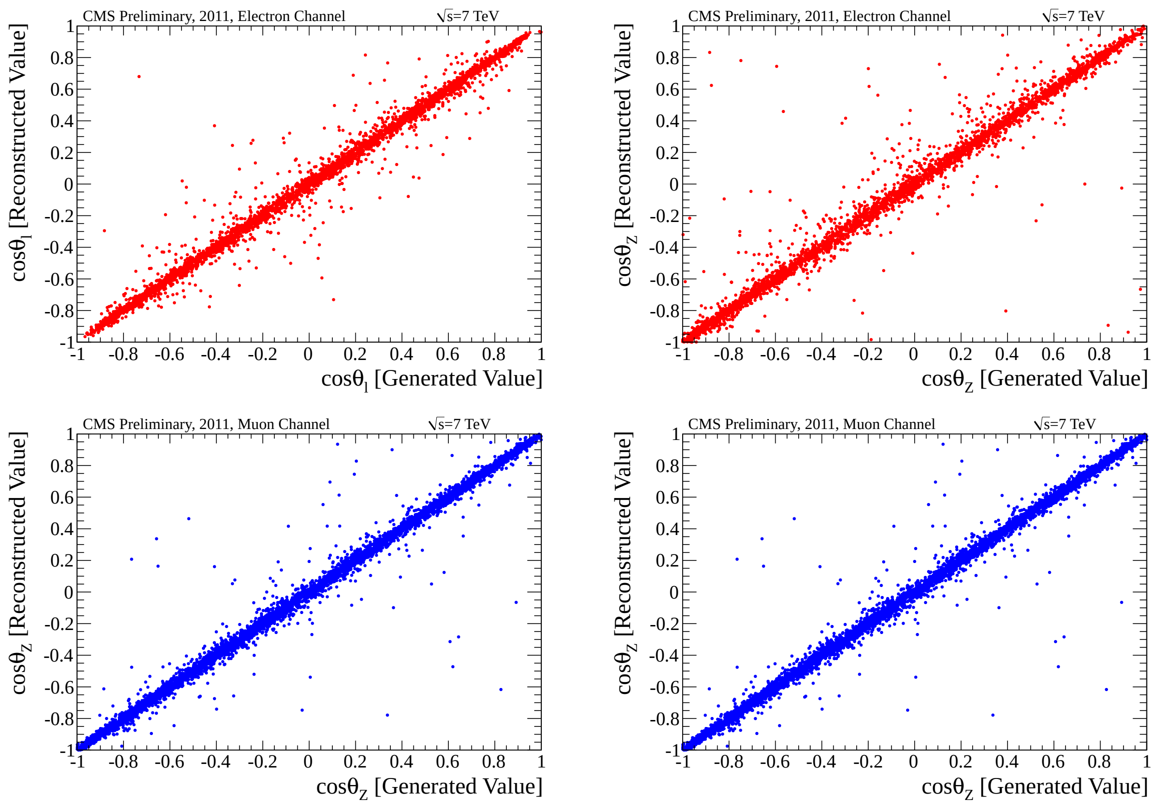

Figure 7.3: Scattered plot of reconstructed vs. generated values for production and decay polar angles in muon (blue) and electron (red) channels.

systematic error.

Extremely low χ^2 between the parameters shows that the resolution effects are negligible and use of the unbinned likelihood is perfectly justified.

$Z \to ee$ channel	k_A	$T^J_{\lambda_{qg}\lambda_Z\lambda_\gamma}$						
		$T^0_{0,-1,-1}$	$T^1_{-1,-1,-1}$	$T^1_{-1,0,-1}$	$T^1_{0,0,-1}$	$T^1_{0,-1,-1}$	$T^1_{1,-1,-1}$	$T^1_{1,0,-1}$
RECO	1.02 $\pm$0.3	-6.17 $\pm$1.5	0.06 $\pm$0.2	-0.36 $\pm$0.3	0.82 $\pm$0.4	0.86 $\pm$0.5	2.76 $\pm$0.9	2.03 $\pm$0.4
GEN	1.01 $\pm$0.0	-6.28 $\pm$0.2	0.098 $\pm$0.2	-0.30 $\pm$0.2	0.90 $\pm$0.1	0.88 $\pm$0.1	2.83 $\pm$0.1	2.12 $\pm$0.1
χ^2	0.0	0.0	0.0	0.0	0.0	0.0	0.0	0.0

Table 7.6: Systematic uncertainties for Z decay and $Z\gamma$ production helicity amplitudes due to the resolution of the variables for $J_{Z\gamma} = 0, 1$. Electron channel.

$Z \to \mu\mu$ channel	k_A	$T^J_{\lambda_{qg}\lambda_Z\lambda_\gamma}$						
		$T^0_{0,-1,-1}$	$T^1_{-1,-1,-1}$	$T^1_{-1,0,-1}$	$T^1_{0,0,-1}$	$T^1_{0,-1,-1}$	$T^1_{1,-1,-1}$	$T^1_{1,0,-1}$
RECO	0.95 $\pm$0.3	-11.05 $\pm$3.7	0.36 $\pm$0.4	-0.06 $\pm$0.6	1.82 $\pm$0.6	2.10 $\pm$0.7	4.78 $\pm$1.1	1.83 $\pm$1.1
GEN	0.97 $\pm$0.0	-11.70 $\pm$0.5	0.33 $\pm$0.3	-0.09 $\pm$0.6	1.87 $\pm$0.3	2.37 $\pm$0.2	5.11 $\pm$0.2	2.21 $\pm$0.4
χ^2	0.0	0.0	0.0	0.0	0.0	0.1	0.1	0.1

Table 7.7: Systematic uncertainties for Z decay and $Z\gamma$ production helicity amplitudes due to the resolution of the variables for $J_{Z\gamma} = 0, 1$. Muon channel.

$Z \to ee$ channel	$T^J_{\lambda_{qg}\lambda_Z\lambda_\gamma}$								
	$T^2_{-1,-1,-1}$	$T^2_{-1,0,-1}$	$T^2_{-1,1,-1}$	$T^2_{0,-1,-1}$	$T^2_{0,0,-1}$	$T^2_{0,1,-1}$	$T^2_{1,-1,-1}$	$T^2_{1,0,-1}$	$T^2_{1,1,-1}$
RECO	-0.33 $\pm$0.2	-0.17 $\pm$0.2	-0.06 $\pm$0.2	-0.09 $\pm$0.2	0.83 $\pm$0.3	-1.02 $\pm$0.7	1.00 $\pm$0.4	0.93 $\pm$0.3	-1.03 $\pm$0.8
GEN	-0.42 $\pm$0.2	-0.14 $\pm$0.1	-0.05 $\pm$0.2	-0.11 $\pm$0.1	0.77 $\pm$0.1	-1.00 $\pm$0.3	0.94 $\pm$0.1	0.92 $\pm$0.1	-1.19 $\pm$0.2
χ^2	0.1	0.0	0.0	0.0	0.1	0.0	0.0	0.0	0.0

Table 7.8: Systematic uncertainties for $Z\gamma$ production helicity amplitudes due to the resolution of the variables for $J_{Z\gamma} = 2$. Electron channel.

$Z \to \mu\mu$ channel	$T^J_{\lambda_{q\bar{q}}\lambda_Z\lambda_\gamma}$								
	$T^2_{-1,-1,-1}$	$T^2_{-1,0,-1}$	$T^2_{-1,1,-1}$	$T^2_{0,-1,-1}$	$T^2_{0,0,-1}$	$T^2_{0,1,-1}$	$T^2_{1,-1,-1}$	$T^2_{1,0,-1}$	$T^2_{1,1,-1}$
RECO	0.36 $\pm$0.3	0.11 $\pm$0.6	-0.44 $\pm$0.5	-0.11 $\pm$0.6	1.38 $\pm$0.5	-2.67 $\pm$1.8	2.38 $\pm$0.7	0.81 $\pm$0.8	-3.84 $\pm$1.3
GEN	0.25 $\pm$0.3	0.05 $\pm$0.5	-0.53 $\pm$0.4	-0.11 $\pm$0.2	1.46 $\pm$0.2	-3.08 $\pm$0.4	2.44 $\pm$0.2	0.97 $\pm$0.3	-4.15 $\pm$0.3
χ^2	0.1	0.0	0.0	0.0	0.0	0.0	0.0	0.0	0.1

Table 7.9: Systematic uncertainties for $Z\gamma$ production helicity amplitudes due to the resolution of the variables for $J_{Z\gamma} = 2$. Muon channel.

7.3 Systematic uncertainties for the background study

Another source of systematic uncertainty is the fact that the background contribution has been neglected in the likelihood function. As already mentioned, the background level from the misidentified photons has been suppressed by the relatively high photon p_T requirement. To obtain the systematic uncertainty due to the background, the pure signal Monte Carlo dataset is compared to the signal plus background Monte Carlo dataset. The signal plus background dataset is comprised of the proper mixture of signal and background events. The proper mixture means that the number of background events is equal to that measured by the data-driven method described in Chapter 6 and number of signal brings the total number to the number of the events in the data. Systematic uncertainties are derived from the χ^2 between signal and signal plus background parameter measurements and are shown in Tables 7.10 through 7.13.

$Z \to ee$ channel	k_A	$T^J_{\lambda_{q\bar{q}}\lambda_Z\lambda_\gamma}$						
		$T^0_{0,-1,-1}$	$T^1_{-1,-1,-1}$	$T^1_{-1,0,-1}$	$T^1_{0,0,-1}$	$T^1_{0,-1,-1}$	$T^1_{1,-1,-1}$	$T^1_{1,0,-1}$
signal	1.02 $\pm$0.3	-6.17 $\pm$1.5	0.06 $\pm$0.2	-0.36 $\pm$0.3	0.82 $\pm$0.4	0.86 $\pm$0.5	2.76 $\pm$0.9	2.03 $\pm$0.4
bkgd	1.03 $\pm$0.1	-7.58 $\pm$0.4	-0.24 $\pm$0.3	-0.62 $\pm$0.3	0.85 $\pm$0.2	1.51 $\pm$0.2	3.40 $\pm$0.2	2.48 $\pm$0.2
χ^2	0.0	0.3	0.7	0.4	0.0	1.6	0.5	1.0

Table 7.10: Systematic uncertainties for Z decay and $Z\gamma$ production helicity amplitudes due to the background for $J_{Z\gamma} = 0, 1$. Electron channel.

$Z \to \mu\mu$ channel	k_A	$T^J_{\lambda_{q\bar{q}}\lambda_Z\lambda_\gamma}$						
		$T^0_{0,-1,-1}$	$T^1_{-1,-1,-1}$	$T^1_{-1,0,-1}$	$T^1_{0,0,-1}$	$T^1_{0,-1,-1}$	$T^1_{1,-1,-1}$	$T^1_{1,0,-1}$
signal	0.95 $\pm$0.3	-11.05 $\pm$3.7	0.36 $\pm$0.4	-0.06 $\pm$0.6	1.82 $\pm$0.6	2.10 $\pm$0.7	4.78 $\pm$1.1	1.83 $\pm$1.1
bkgd	0.96 $\pm$0.1	-10.84 $\pm$0.9	0.13 $\pm$0.5	-0.79 $\pm$0.7	1.55 $\pm$0.4	2.10 $\pm$0.3	4.86 $\pm$0.4	2.16 $\pm$0.5
χ^2	0.0	0.0	0.1	0.6	0.1	0.0	0.0	0.1

Table 7.11: Systematic uncertainties for Z decay and $Z\gamma$ production helicity amplitudes due to the background for $J_{Z\gamma} = 0, 1$. Muon channel.

$Z \to ee$ channel	$T^J_{\lambda_{q\bar{q}}\lambda_Z\lambda_\gamma}$								
	$T^2_{-1,-1,-1}$	$T^2_{-1,0,-1}$	$T^2_{-1,1,-1}$	$T^2_{0,-1,-1}$	$T^2_{0,0,-1}$	$T^2_{0,1,-1}$	$T^2_{1,-1,-1}$	$T^2_{1,0,-1}$	$T^2_{1,1,-1}$
signal	-0.33 ± 0.2	-0.17 ± 0.2	-0.06 ± 0.2	-0.09 ± 0.2	0.83 ± 0.3	-1.0 ± 0.7	1.00 ± 0.4	0.93 ± 0.3	-1.03 ± 0.8
bkgd	-0.03 ± 0.0	0.04 ± 0.0	0.01 ± 0.0	0.40 ± 0.0	0.29 ± 0.0	-1.8 ± 0.3	1.38 ± 0.2	1.30 ± 0.2	-1.79 ± 0.3
χ^2	1.8	1.0	0.1	7.2	4.6	1.1	0.7	1.2	0.8

Table 7.12: Systematic uncertainties for $Z\gamma$ production helicity amplitudes due to the background for $J_{Z\gamma} = 2$. Electron channel.

$Z \to \mu\mu$ channel	$T^J_{\lambda_{q\bar{q}}\lambda_Z\lambda_\gamma}$								
	$T^2_{-1,-1,-1}$	$T^2_{-1,0,-1}$	$T^2_{-1,1,-1}$	$T^2_{0,-1,-1}$	$T^2_{0,0,-1}$	$T^2_{0,1,-1}$	$T^2_{1,-1,-1}$	$T^2_{1,0,-1}$	$T^2_{1,1,-1}$
signal	0.36 ± 0.3	0.11 ± 0.6	-0.44 ± 0.5	-0.11 ± 0.6	1.38 ± 0.5	-2.67 ± 1.8	2.38 ± 0.7	0.81 ± 0.8	-3.84 ± 1.3
bkgd	0.31 ± 0.5	-0.06 ± 0.7	-0.39 ± 0.6	-0.02 ± 0.3	1.67 ± 0.3	-2.63 ± 0.6	2.48 ± 0.3	0.49 ± 0.5	-3.67 ± 0.4
χ^2	0.0	0.0	0.0	0.0	0.2	0.0	0.0	0.1	0.0

Table 7.13: Systematic uncertainties for $Z\gamma$ production helicity amplitudes due to the background for $J_{Z\gamma} = 2$. Muon channel.

The systematic uncertainties due to the background effects in the muon channel are very small, however in the electron channel they are more pronounced. This is due to a smaller statistics in the electron channel, which contributes double-fold to this effect. First, due to a very low statistics in the high E_T^γ bins, the fit for the template method for the background estimation is not very well defined and it gives bigger error. Consequently, the scale factors for the backgrounds are much higher than simple extrapolation to that E_T^γ region would give. Secondly, due to the low statistics the flat angular distribution of the background causes the parameters at the high order $\cos\theta_Z(\cos\theta_\ell)$ to be lower. These reasons, in combination with background effects being much lower for the muon channel, give me confidence that the assumption for neglecting the background is justified.

7.4 Systematic uncertainties for LO to NLO comparison study

Since the distribution function used for the parameter measurement is describing the leading order $Z\gamma \to \ell\ell\gamma$ production, the effect of the NLO processes on the measured parameters has to be estimated. This systematic error is not the error on the parameters measured on the data, but need to be added to the parameters measured on the standard model Monte Carlo in order to compare the measurement to the standard model predictions. Also these are the systematic uncertainties on the physical leading order amplitudes.

As discussed earlier, the Monte Carlo generator for the next to leading order $Z\gamma$ production is not available. Therefore, to serve the same purpose, I use the Monte Carlo generated dataset for $Z(\ell\bar{\ell})\gamma$ plus up to two jets in the final state. This ensures that the $Z\gamma$ system is recoiled against the jet with roughly the same branching fraction as the NLO contribution. Of course this dataset cannot provide the proper standard model fractions for individual helicity state contributions. The proper estimation of the NLO effects requires better NLO tools.

The systematic uncertainty is obtained from the χ^2 between parameters measured on the LO and *quasi*-NLO datasets, taking the same number of events for both. The results of the measurement are shown in Tables 7.14, 7.16, 7.15, and 7.17.

$Z \to ee$ channel	k_A	$T^J_{\lambda_{qq}\lambda_Z\lambda_\gamma}$						
		$T^0_{0,-1,-1}$	$T^1_{-1,-1,-1}$	$T^1_{-1,0,-1}$	$T^1_{0,0,-1}$	$T^1_{0,-1,-1}$	$T^1_{1,-1,-1}$	$T^1_{1,0,-1}$
LO	1.02 $\pm$0.3	-6.17 $\pm$1.5	0.06 $\pm$0.2	-0.36 $\pm$0.3	0.82 $\pm$0.4	0.86 $\pm$0.5	2.76 $\pm$0.9	2.03 $\pm$0.4
NLO	1.00 $\pm$0.0	-2.22 $\pm$0.3	-0.13 $\pm$0.1	-0.15 $\pm$0.1	0.23 $\pm$0.1	0.27 $\pm$0.1	1.03 $\pm$0.1	0.75 $\pm$0.1
χ^2	0.0	6.7	0.7	0.4	2.3	1.4	3.7	9.1

Table 7.14: Systematic uncertainties for Z decay and $Z\gamma$ production helicity amplitudes due to the NLO effects for $J_{Z\gamma} = 0, 1$. Electron channel.

The immediate observation from this study is that the quasi-NLO sample that we use

$Z \to \mu\mu$ channel	k_A	$T^J_{\lambda_{q\bar{q}}\lambda_Z\lambda_\gamma}$						
		$T^0_{0,-1,-1}$	$T^1_{-1,-1,-1}$	$T^1_{-1,0,-1}$	$T^1_{0,0,-1}$	$T^1_{0,-1,-1}$	$T^1_{1,-1,-1}$	$T^1_{1,0,-1}$
LO	0.95 $\pm$0.3	-11.05 $\pm$3.7	0.36 $\pm$0.4	-0.06 $\pm$0.6	1.82 $\pm$0.6	2.10 $\pm$0.7	4.78 $\pm$1.1	1.83 $\pm$1.1
NLO	1.03 $\pm$0.0	-7.21 $\pm$0.5	0.14 $\pm$0.2	0.20 $\pm$0.3	1.19 $\pm$0.2	0.65 $\pm$0.2	3.07 $\pm$0.2	1.20 $\pm$0.3
χ^2	0.1	1.0	0.2	0.1	1.1	3.6	2.2	0.3

Table 7.15: Systematic uncertainties for Z decay and $Z\gamma$ production helicity amplitudes due to the NLO effects for $J_{Z\gamma} = 0, 1$. Muon channel.

$Z \to ee$ channel	$T^J_{\lambda_{q\bar{q}}\lambda_Z\lambda_\gamma}$								
	$T^2_{-1,-1,-1}$	$T^2_{-1,0,-1}$	$T^2_{-1,1,-1}$	$T^2_{0,-1,-1}$	$T^2_{0,0,-1}$	$T^2_{0,1,-1}$	$T^2_{1,-1,-1}$	$T^2_{1,0,-1}$	$T^2_{1,1,-1}$
LO	-0.33 $\pm$0.2	-0.17 $\pm$0.2	-0.06 $\pm$0.2	-0.09 $\pm$0.2	0.83 $\pm$0.3	-1.02 $\pm$0.7	1.00 $\pm$0.4	0.93 $\pm$0.3	-1.03 $\pm$0.8
NLO	-0.10 $\pm$0.1	-0.13 $\pm$0.1	0.04 $\pm$0.1	0.11 $\pm$0.1	0.50 $\pm$0.1	-0.27 $\pm$0.1	0.93 $\pm$0.1	0.55 $\pm$0.1	-0.28 $\pm$0.1
χ^2	1.0	0.0	0.2	0.9	1.6	1.1	0.0	1.6	0.8

Table 7.16: Systematic uncertainties for $Z\gamma$ production helicity amplitudes due to the NLO effects for $J_{Z\gamma} = 2$. Electron channel.

brings the $J_{Z\gamma} = 2$ contribution downs and $J_{Z\gamma} = 1, 2$ contributions up, this can be seen in a few parameters that are off the most. The conclusion that could be drawn is that adding up to two jets to the sample without correct NLO matrix elements does not lead to a correct description of the process. However, this sample can be used for the NLO $Z\gamma$ cross-section calculation studies, it is not a good estimator of NLO effects in a detailed analysis like one presented in this thesis.

$Z \to \mu\mu$ channel	$T^J_{\lambda_{q\bar{q}}\lambda_Z\lambda_\gamma}$								
	$T^2_{-1,-1,-1}$	$T^2_{-1,0,-1}$	$T^2_{-1,1,-1}$	$T^2_{0,-1,-1}$	$T^2_{0,0,-1}$	$T^2_{0,1,-1}$	$T^2_{1,-1,-1}$	$T^2_{1,0,-1}$	$T^2_{1,1,-1}$
LO	0.36 $\pm$0.3	0.11 $\pm$0.6	-0.44 $\pm$0.5	-0.11 $\pm$0.6	1.38 $\pm$0.5	-2.67 $\pm$1.8	2.38 $\pm$0.7	0.81 $\pm$0.9	-3.85 $\pm$1.3
NLO	0.19 $\pm$0.2	0.04 $\pm$0.2	0.05 $\pm$0.3	-0.16 $\pm$0.2	1.13 $\pm$0.2	-1.25 $\pm$0.3	1.97 $\pm$0.2	0.51 $\pm$0.2	-2.29 $\pm$0.3
χ^2	0.2	0.0	0.8	0.0	0.2	0.6	0.3	0.1	1.5

Table 7.17: Systematic uncertainties for $Z\gamma$ production helicity amplitudes due to the NLO effects for $J_{Z\gamma} = 2$. Muon channel.

7.5 Conclusion

The idea of the comprehensive multidimensional angular analysis to study the $Z\gamma$ di-boson production is presented along with the methods for the derivation of the distribution function and building the model. The analysis shows that the analyzed data reveals no significant deviations of the measured helicity amplitudes from their standard model predictions. Tables 7.18, 7.20, 7.19 and 7.21 present the final measurements including the systematic uncertainties from background and resolution for data and NLO corrections for the Monte Carlo.

$Z \to ee$ channel	k_A	$T^J_{\lambda_{q\bar{q}}\lambda_Z\lambda_\gamma}$						
		$T^0_{0,-1,-1}$	$T^1_{-1,-1,-1}$	$T^1_{-1,0,-1}$	$T^1_{0,0,-1}$	$T^1_{0,-1,-1}$	$T^1_{1,-1,-1}$	$T^1_{1,0,-1}$
signal	1.02 $\pm$0.3	-6.17 $\pm$1.8	0.06 $\pm$0.3	-0.36 $\pm$0.4	0.82 $\pm$0.5	0.86 $\pm$0.6	2.76 $\pm$0.9	2.03 $\pm$0.5
data	1.00 $\pm$0.5	-7.84 $\pm$4.4	-1.08 $\pm$1.7	-2.57 $\pm$1.9	3.23 $\pm$1.7	-2.00 $\pm$2.7	-0.36 $\pm$1.3	2.23 $\pm$2.1
χ^2	0.0	0.1	0.4	1.3	2.0	1.1	3.4	0.0

Table 7.18: Data and Monte Carlo measurement results for Z decay and $Z\gamma$ production helicity amplitudes for $J_{Z\gamma} = 0, 1$ including systematic uncertainties. Electron channel.

$Z \to \mu\mu$ channel	k_A	$T^J_{\lambda_{q\bar{q}}\lambda_Z\lambda_\gamma}$						
		$T^0_{0,-1,-1}$	$T^1_{-1,-1,-1}$	$T^1_{-1,0,-1}$	$T^1_{0,0,-1}$	$T^1_{0,-1,-1}$	$T^1_{1,-1,-1}$	$T^1_{1,0,-1}$
signal	0.95 $\pm$0.3	-11.05 $\pm$4.3	0.36 $\pm$0.6	-0.06 $\pm$0.9	1.82 $\pm$0.8	2.10 $\pm$0.9	4.78 $\pm$1.3	1.83 $\pm$1.3
data	1.06 $\pm$0.5	-11.43 $\pm$4.9	-0.24 $\pm$1.0	-0.64 $\pm$1.7	2.38 $\pm$1.4	2.73 $\pm$1.5	5.42 $\pm$2.3	4.16 $\pm$1.9
χ^2	0.0	0.0	0.2	0.1	0.1	0.1	0.1	1.0

Table 7.19: Data and Monte Carlo measurement results for Z decay and $Z\gamma$ production helicity amplitudes for $J_{Z\gamma} = 0, 1$ including systematic uncertainties. Muon channel.

7.6 Outlook

Presented analysis is based on the 5 fb^{-1} data, and therefore is statistically limited. The straightforward extension of this analysis would be to plug in the proper correction factors

$Z \to ee$ channel	$T^J_{\lambda_{qq}\lambda_Z\lambda_\gamma}$								
	$T^2_{-1,-1,-1}$	$T^2_{-1,0,-1}$	$T^2_{-1,1,-1}$	$T^2_{0,-1,-1}$	$T^2_{0,0,-1}$	$T^2_{0,1,-1}$	$T^2_{1,-1,-1}$	$T^2_{1,0,-1}$	$T^2_{1,1,-1}$
signal	-0.33 ± 0.2	-0.17 ± 0.2	-0.06 ± 0.2	-0.09 ± 0.2	0.83 ± 0.3	-1.02 ± 0.7	1.00 ± 0.4	0.93 ± 0.3	-1.03 ± 0.8
data	-0.60 ± 2.9	0.23 ± 1.7	4.06 ± 1.8	1.91 ± 8.2	-0.61 ± 5.5	1.36 ± 2.5	1.95 ± 1.9	-0.66 ± 1.7	1.44 ± 1.9
χ^2	0.0	0.0	4.9	0.0	0.0	0.8	0.2	0.9	1.4

Table 7.20: Data and Monte Carlo measurement results for $Z\gamma$ production helicity amplitudes for $J_{Z\gamma} = 2$ including systematic uncertainties. Electron channel.

$Z \to \mu\mu$ channel	$T^J_{\lambda_{qq}\lambda_Z\lambda_\gamma}$								
	$T^2_{-1,-1,-1}$	$T^2_{-1,0,-1}$	$T^2_{-1,1,-1}$	$T^2_{0,-1,-1}$	$T^2_{0,0,-1}$	$T^2_{0,1,-1}$	$T^2_{1,-1,-1}$	$T^2_{1,0,-1}$	$T^2_{1,1,-1}$
signal	0.36 ± 0.5	0.11 ± 0.6	-0.44 ± 0.7	-0.11 ± 0.7	1.38 ± 0.7	-2.67 ± 2.1	2.38 ± 0.9	0.81 ± 1.0	-3.84 ± 1.5
data	0.42 ± 0.7	0.23 ± 0.7	0.68 ± 1.0	-0.87 ± 0.8	2.57 ± 1.3	-4.84 ± 2.3	3.40 ± 1.5	0.35 ± 1.3	-3.99 ± 2.2
χ^2	0.0	0.0	0.8	0.5	0.6	0.5	0.3	0.1	0.0

Table 7.21: Data and Monte Carlo measurement results for $Z\gamma$ production helicity amplitudes for $J_{Z\gamma} = 2$ including systematic uncertainties. Muon channel.

for the 2012 data and extend it to the full available statistics. This would lower the statistical error and make it possible to measure both real and imaginary parts of the helicity amplitudes. On the other hand, this analysis laid solid ground for the future di-boson angular analysis. With more data similar analysis could be performed for the ZZ production. It would be interesting to perform partial wave analysis and see if particular helicity wave resonances could be found in different mass or rapidity ranges. In principal this kind of helicity analysis could be performed to study the properties of the Higgs boson if it is observed in the $Z\gamma$ or ZZ channels.

Bibliography

[1] A. Barker et al., "Study of $W\gamma$ and $Z\gamma$ production at CMS with $\sqrt{s} = 7$ TeV," 2011. CMS AN 2011/251.

[2] J.Beringer et al. (Particle Data Group), "Quantum chromodynamics," *Phys. Rev.*, vol. D86, no. 010001, 2012.

[3] J.Beringer et al. (Particle Data Group), "Electroweak model and constraints on new physics," *Phys. Rev.*, vol. D86, no. 010001, 2012.

[4] Z. Q. a. A. Liu, "Study of $e^+e^- \rightarrow \pi^+\pi^- j/\psi$ and observation of a charged charmoniumlike state at belle," *Phys. Rev. Lett.*, vol. 110, p. 252002, Jun 2013.

[5] R. Aaij *et al.*, "Observation of the resonant character of the $Z(4430)^-$ state," 2014. LHCb collaboration, LHCB-PAPER-2014-014, CERN-PH-EP-2014-061.

[6] M. Gell-Mann, "A Schematic Model of Baryons and Mesons," *Phys.Lett.*, vol. 8, pp. 214–215, 1964.

[7] S. Weinberg, "Non-abelian gauge theories of the strong interactions," *Phys. Rev. Lett.*, vol. 31, pp. 494–497, Aug 1973.

[8] H. Fritzsch, M. Gell-Mann, and H. Leutwyler, "Advantages of the color octet gluon picture," *Physics Letters B*, vol. 47, no. 4, pp. 365 – 368, 1973.

[9] D. J. Gross and F. Wilczek, "Asymptotically free gauge theories. i," *Phys. Rev. D*, vol. 8, pp. 3633–3652, Nov 1973.

[10] C. N. Yang and R. L. Mills, "Conservation of isotopic spin and isotopic gauge invariance," *Phys. Rev.*, vol. 96, pp. 191–195, Oct 1954.

[11] C. S. Wu, E. Ambler, R. W. Hayward, D. D. Hoppes, and R. P. Hudson, “Experimental test of parity conservation in beta decay,” *Phys. Rev.*, vol. 105, pp. 1413–1415, Feb 1957.

[12] S. L. Glashow, “Partial-symmetries of weak interactions,” *Nuclear Physics*, vol. 22, no. 4, pp. 579 – 588, 1961.

[13] S. Weinberg, “A model of leptons,” *Phys. Rev. Lett.*, vol. 19, pp. 1264–1266, Nov 1967.

[14] A. Salam, “Elementary particle theory,” *Proceedings Of The Nobel Symposium Held At Lerum, Sweden*, vol. 8, pp. 367–377, 1968.

[15] G. Arnison *et al.*, “Experimental Observation of Lepton Pairs of Invariant Mass Around 95-GeV/c**2 at the CERN SPS Collider,” *Phys.Lett.*, vol. B126, pp. 398–410, 1983.

[16] M. Banner *et al.*, “Observation of Single Isolated Electrons of High Transverse Momentum in Events with Missing Transverse Energy at the CERN anti-p p Collider,” *Phys.Lett.*, vol. B122, pp. 476–485, 1983.

[17] CMS Collaboration, “Observation of a new boson at a mass of 125 gev with the CMS experiment at the LHC,” *Physics Letters B*, vol. 716, no. 1, pp. 30 – 61, 2012.

[18] J. Campbell, K. Ellis, C. Williams, “MCFM - Monte Carlo for FeMtobarn processes.” http://mcfm.fnal.gov/.

[19] U. Baur, T. Han, and J. Ohnemus, “Qcd corrections and anomalous couplings in $z\gamma$ production at hadron colliders,” *Phys. Rev. D*, vol. 57, pp. 2823–2836, Mar 1998.

[20] J. D. Richman, “An Experimenter’s Guide to the Helicity Formalism,” *CALT-68-1148*, 1984.

[21] R. Brun and F. Rademakers, “Root - an object oriented data analysis framework,” 1996. Proceedings AIHENP’96 Workshop, Lausanne, Sep. 1996, Nucl. Inst. & Meth. in Phys. Res. A 389 (1997) 81-86. See also http://root.cern.ch/.

[22] D. Acosta et al, "Cms high level trigger," 2007. CMS AN 2007/009.

[23] S. Cucciarelli, M. Konecki, D. Kotliński, and T.Todorov, "Track reconstruction, primary vertex finding and seed generation with the pixel detector," 2006. CMS AN 2006/026.

[24] CMS Collaboration, "Detector performance and software," CMS TDR 8.1 2006-001, CERN/LHCC, February 2006.

[25] R. Frühwirth, M. Regler, R. Bock, H. Grote, and D. Notz, *Data Analysis Techniques for High-Energy Physics*, vol. 2nd Ed. Cambridge University Press, 2000.

[26] CMS Collaboration, "The TriDAS Project Technical Design Report, Volume 2: Data Acquisition and High-Level Trigger," CMS TDR 6 02-26, CERN/LHCC, December 2002.

[27] "Pile-up reweighting using cms fastject package." unpublished, restricted access at: https://twiki.cern.ch/twiki/bin/viewauth/CMS/PileupReweighting.

[28] C. Amsler et al, "Passage of particles through matter," *Phys.Lett.*, 2008. B667(1).

[29] G. Bella, "Weighting di-boson monte carlo events in hadron colliders," *arXiv:0803.3307 [hep-ph]*, 2008.

[30] N. Adam et al., "Generic Tag and Probe Tool for Measuring Efficiency at CMS with Early Data," 2009. CMS AN 2009/111.

Appendix A

Constructing the Likelihood Function

In section 2.4, the angular distribution function 2.9 is recast into a form 2.18. The final $-\ln(L)$ function that is minimized for measuring the $A_{\lambda_{\ell\ell}}$ and $T^{J}_{\lambda_{qq}\lambda_Z\lambda_\gamma}$ helicity amplitudes relies on the careful and correct interpretation of the A_i as a function of the helicity parameters and $\omega_i(\Omega)$ as a construct of the functions in the angular distribution function.

Let's rewrite Eq. 2.16 to a generic form:

$$W(x) = \sum_i \left| \sum_j a_j f_{ij}(x) e^{-i\alpha_j \phi} \right|^2, \tag{A.1}$$

$$a_j = A_{\lambda_{\ell\ell}} T^{J}_{\lambda_{qq}\lambda_Z\lambda_\gamma}; \quad \alpha_j \phi = \lambda_Z \varphi_\ell - (\lambda_{qq} - \lambda_Z)\varphi_Z, \tag{A.2}$$

$$f_{ij}(x) = F(\cos\theta_Z)[(2J+1) d^{J}_{\lambda_{q\bar{q}}\lambda_{Z\gamma}}(\cos\theta_Z) d^{1}_{\lambda_Z \lambda_{\ell\ell}}(\cos\theta_\ell)], \tag{A.3}$$

where, summation over i is sumation over λ_γ and $\lambda_{\ell\ell}$ and summation over j is - J, λ_Z and λ_{qq}. The outer sum just produces the elements of the inner sum, which, considering a_{ij} and α_{ij} are real parameters and $f_{ij}(x)$ are real functions, can be expended to the following:

$$\left| \sum_i a_i f_i(x) e^{-i\alpha_i \phi} \right|^2 = \sum_i \sum_{j \geqslant i} (2 - \delta_{ij}) a_i a_j x_i x_j \cos([\alpha_i - \alpha_j]\phi), \tag{A.4}$$

where $\delta_{ij} i$ is a Kroneker delta symbol. In general, helicity amplitudes are complex numbers, so substituding a_i in A.4 by $z_i = a_i + ib_i$:

$$
\begin{aligned}
\left|\sum_i z_i x_i e^{i\alpha_i\phi}\right|^2 &= \left|\sum_i a_i x_i e^{i\alpha_i\phi} + i\sum_i b_i x_i e^{i\alpha_i\phi}\right|^2 \\
&= \left|\sum_i a_i x_i e^{i\alpha_i\phi} \;|^2 + |\sum_i x_i b_i e^{i\alpha_i\phi}\right|^2 \\
&= \sum_i \sum_{j\geqslant i} (2-\delta_{ij}) a_i a_j x_i x_j \cos([\alpha_i - \alpha_j]\phi) \\
&\quad + \sum_i \sum_{j\geqslant i} (2-\delta_{ij}) b_i b_j x_i x_j \cos([\alpha_i - \alpha_j]\phi) \\
&= \sum_i \sum_{j\geqslant i} (2-\delta_{ij}) x_i x_j (a_i a_j + b_i b_j) \cos([\alpha_i - \alpha_j]\phi).
\end{aligned} \tag{A.5}
$$

Thus, the parameters A_i and the functions $\omega_i(\Omega)$ have the following form:

$$
A_i = |A_{\lambda_{\ell\ell}}|^2[\mathscr{R}\mathrm{e}(T_m)\mathscr{R}\mathrm{e}(T_n) + \mathscr{I}\mathrm{m}(T_m)\mathscr{I}\mathrm{m}(T_n)], \tag{A.6}
$$

$$
\begin{aligned}
\omega_i(\Omega) = F(\cos\theta_Z)&(2-\delta_{mn})\times \\
&[(2J_m+1)d_m(\cos\theta_Z)d_m(\cos\theta_\ell)\times \\
&(2J_n+1)d_n(\cos\theta_Z)d_n(\cos\theta_\ell)]\times \\
&\cos([(\lambda_{qq}^m + \lambda_Z^m)\varphi_Z - \lambda_{\ell\ell}^m\varphi_\ell] - [(\lambda_{qq}^n + \lambda_Z^n)\varphi_Z - \lambda_{\ell\ell}^n\varphi_\ell]),
\end{aligned} \tag{A.7}
$$

where m and n run every possible permutations of the helicities. The outer sum produces these elements of inner summation for every $\lambda_{\ell\ell}$.